Nuclear irradiation effects on additive manufactured Inconel 625 & 718

by

Mohanish Andurkar

B. Eng., University of Mumbai, 2016
MET., Pittsburg State University, 2018

AN ABSTRACT OF A DISSERTATION

submitted in partial fulfillment of the requirements for the degree

DOCTOR OF PHILOSOPHY

Alan Levin Department of Mechanical and Nuclear Engineering
Carl R. Ice College of Engineering

KANSAS STATE UNIVERSITY
Manhattan, Kansas

2024

Abstract

The effects of neutron irradiation and extreme environment conditions on the structural integrity of parts additively manufactured (AM) via the laser-powder bed fusion method (L-PBF), the most common AM method for producing strong/durable metallic parts, is not currently well understood. This is hampering the direct, dependable, and immediate use of AM for generating compact/efficient, functional equipment for very small modular reactors (SMRs) and nuclear propulsion. This dissertation focuses on AM materials most suitable for operating within extreme environments, i.e., nickel-based superalloys. These alloys are currently used for nuclear applications such as control rods, tension springs, fuel channel spacers, and more, since they possess superior properties such as corrosion resistance, creep resistance, and strength at elevated temperatures. In many cases, AM enables a more cost efficient and securer means for fabricating SMR structural components by reducing the number of suppliers required for component assembly and allowing for on-site/remote fabrication.

This research aims to better understand the difference in mechanical properties of L-PBF nickel-based superalloys (and wrought counterparts), before and after distinct types of neutron irradiation to accelerate their safe, reliable use in nuclear applications. The major objective is to quantify the microhardness of two nickel-based superalloys additively manufactured via L-PBF, i.e., Inconel 718 (IN718) and Inconel 625 (IN625). Another objective is to measure and compare the residual stress in L-PBF samples built at different orientations and post-processing heat treatment schedules. Effects of build orientation during L-PBF and post-AM heat treatments on radiation hardening resistance are investigated. Neutron damage mechanisms via irradiation-induced hardening will be characterized. Although neutron radiation hardening defects within

conventionally machined metals are commonly reported in the literature, this research is among the first of its kind focused on L-PBF nickel-based superalloys.

The findings from this research will give a better head-to-head comparison between the performance of AM and conventionally machined nickel-based superalloys under similar neutron irradiation environments. In practice, nuclear reactor components are irradiated with thermal neutrons, which have relatively low energy spectra, over several years, leading to accumulated damage and the generation of radioactive isotopes. This complicates the qualification of nuclear materials since the radioactivity level of post-service components makes inspection time consuming. Thus, alternative forms of accelerated irradiation testing such as fast neutron irradiation are investigated herein. Fast neutron irradiation produces lower levels of radioactivity in metals while still providing relevant damage levels on specimens.

Key results indicate that after full spectrum neutron irradiation, most L-PBF samples showed a higher tolerance towards radiation-induced hardening relative to the wrought samples. After fast neutron irradiation, IN625 and IN718 samples demonstrated hardening at the beginning of exposure, but later underwent radiation softening, most likely due to dislocation dissolution in the microstructure. L-PBF build orientation and post-processing heat treatment was also found to play a vital role in the amount of residual stress formed in IN625. Heat treatment at higher temperature reduces detrimental surface tensile residual stresses. All these precious experimental data demonstrate a noteworthy structural integrity of L-PBF materials after their exposure to different irradiation environments. Results provide insight into how one may minimize radiation hardening defects in such materials for maintaining material property constraints for a targeted service life. Research findings should assist engineers in selecting and interpreting an appropriate heat treatment for L-PBF nickel-based superalloys for increased radiation damage resistance.

Major results can increase confidence levels for adopting AM for building nuclear reactor components which perform the same or better than conventionally manufactured components.

Nuclear irradiation effects on additive manufactured Inconel 625 & 718

by

Mohanish Andurkar

B. Eng., University of Mumbai, 2016
MET., Pittsburg State University, 2018

A DISSERTATION

submitted in partial fulfillment of the requirements for the degree

DOCTOR OF PHILOSOPHY

Alan Levin Department of Mechanical and Nuclear Engineering
Carl R. Ice College of Engineering

KANSAS STATE UNIVERSITY
Manhattan, Kansas

2024

Approved by: Approved by:

Co-Major Professor   Co-Major Professor
Dr. Rajkumar Pal   Dr. S. M. Thompson

Copyright

Abstract

The effects of neutron irradiation and extreme environment conditions on the structural integrity of parts additively manufactured (AM) via the laser-powder bed fusion method (L-PBF), the most common AM method for producing strong/durable metallic parts, is not currently well understood. This is hampering the direct, reliable, and immediate use of AM for generating compact/efficient, functional equipment for very small modular reactors (SMRs) and nuclear propulsion. This dissertation focuses on AM materials most suitable for operating within extreme environments, i.e., nickel-based superalloys. These alloys are currently used for nuclear applications such as control rods, tension springs, fuel channel spacers, and more, since they possess superior properties such as corrosion resistance, creep resistance, and strength at elevated temperatures. In many cases, AM enables a more cost efficient and securer means for fabricating SMR structural components by reducing the number of suppliers required for component assembly and allowing for on-site/remote fabrication.

This research aims to better understand the difference in mechanical properties of L-PBF nickel-based superalloys (and wrought counterparts), before and after distinct types of neutron irradiation to accelerate their safe, reliable use in nuclear applications. The major objective is to quantify the microhardness of two nickel-based superalloys additively manufactured via L-PBF, i.e., Inconel 718 (IN718) and Inconel 625 (IN625). Another objective is to measure and compare the residual stress in L-PBF samples built at different orientations and post-processing heat treatment schedules. Effects of build orientation during L-PBF and post-AM heat treatments on radiation hardening resistance are investigated. Neutron damage mechanisms via irradiation-induced hardening will be characterized. Although neutron radiation hardening defects within

conventionally machined metals are commonly reported in the literature, this research is among the first of its kind focused on L-PBF nickel-based superalloys.

The findings from this research will give a better head-to-head comparison between the performance of AM and conventionally machined nickel-based superalloys under similar neutron irradiation environments. In practice, nuclear reactor components are irradiated with thermal neutrons, which have relatively low energy spectra, over several years, leading to accumulated damage and the generation of radioactive isotopes. This complicates the qualification of nuclear materials since the radioactivity level of post-service components makes inspection time consuming. Thus, alternative forms of accelerated irradiation testing such as fast neutron irradiation are investigated herein. Fast neutron irradiation produces lower levels of radioactivity in metals while still providing relevant damage levels on specimens.

Key results indicate that after full spectrum neutron irradiation, most L-PBF samples showed a higher tolerance towards radiation-induced hardening relative to the wrought samples. After fast neutron irradiation, IN625 and IN718 samples demonstrated hardening at the beginning of exposure, but later underwent radiation softening, most likely due to dislocation dissolution in the microstructure. L-PBF build orientation and post-processing heat treatment was also found to play a vital role in the amount of residual stress formed in IN625. Heat treatment at higher temperature reduces detrimental surface tensile residual stresses. All these precious experimental data demonstrate a noteworthy structural integrity of L-PBF materials after their exposure to different irradiation environments. Results provide insight into how one may minimize radiation hardening defects in such materials for maintaining material property constraints for a targeted service life. Research findings should assist engineers in selecting and interpreting an appropriate heat treatment for L-PBF nickel-based superalloys for increased radiation damage resistance.

Major results can increase confidence levels for adopting AM for building nuclear reactor components which perform the same or better than conventionally manufactured components.

Table of Contents

List of Figures

List of Tables

Acknowledgements

Dedication

I dedicate this dissertation to my family and girlfriend.

Preface

Figure 2.3 from Chapter 2 and parts from Chapter 3 are reproduced from [1] V. O'Donnell *et al.*, "Diagnostic Technique Characterizing Neutron Irradiation Effects on Additively Manufactured Inconel 625 Eliminating the Need for Remote Handling," *Nucl. Technol.*, vol. 209, no. 2, pp. 254–260, 2023, doi: 10.1080/00295450.2022.2120321., with permission from Nuclear Technology.

Chapter 1 - Introduction

1.1 History of additive manufacturing

Additive manufacturing (AM) is the formalized term for what used to be called rapid prototyping and what is popularly called 3D Printing. The origins of AM dates to the 1980's when Chuck Hull invented the first ever 3D printer. Hull's printed employed stereolithography (SLA) technique which is still used in modern times. This SLA machine was patented in 1986 and Chuck Hull co-founded 3D Systems Corporation. Following this, other forms of AM were explored and developed including selective laser sintering (SLS) by Carl Deckard, direct metal laser sintering (DMLS) by German company EOS GmbH, and fused deposition modeling (FDM) by S. Scott Crump. In those times, only plastics could be printed. The surface finish and level of details were too low to be adopted in real-life applications. Hence, AM process parts were used only for prototyping purposes [2]. The expiration of the old patents opened the field for significantly more affordable consumer and hobbyist focused 3D printers to be developed.

The late 1990's marked the beginning of 3D printers using polymers and metal alloys. Customized tools required during manufacturing process such as jigs, molds used in injection molding and casting have been traditionally built via subtractive manufacturing techniques. In these techniques, the margin for errors to build user-defined geometry is minimal. Hence, mistakes can be quite costly and there is little room for flexibility in terms of fixing the manufactured tools. In contrast, AM technology provides opportunities to print molds in fraction of time and cost of subtractive manufacturing. Later in 2000's, 3D printers became more affordable and available to consumers. The quality of parts produced also increased and started to be adopted by various industries.

1.2 Additive manufacturing of metals

As per the International Organization for Standardization (ISO) and American Society for Testing and Materials (ASTM), additive manufacturing (AM) is divided into seven major categories. Binder jetting, Directed Energy Deposition (DED), Powder Bed Fusion, Sheet Lamination, Material Extrusion, Material Jetting, Vat Photo Polymerization [3]. Out of these seven, the first four are appropriate for fabrication of metals. Laser Powder Bed Fusion (L-PBF) offers the ability to fabricate metal parts with highly customized geometries, tailored structures, and consolidated assemblies. This AM technique has several advantages over traditional manufacturing methods, including, fabrication-friendly environments promoting lean production by reducing material waste, fabrication of parts made from a broad range of materials including superalloys, and reduction of fabrication time and cost [4][5]. A schematic of the L-PBF process and its different components are presented in Figure 1.1. During L-PBF, a focused high-energy laser beam selectively melts a powder layer between 10-100 μm [6] in thickness accompanied with rapid cooling/solidification to a predetermined shape defined via computer aided drawing (CAD) data. The scanning system can rotate to guide the laser to the desired spot. The f-θ lens helps to maintain the required laser spot size. The build platform moves downwards in the Z-direction. The distance traveled by the build platform is equal to the layer thickness defined. The roller (or blade) spreads a new powder layer on the previous melted layer and the laser is traced again on the new layer. The unused powder is rolled over in the next round and collected in the overflow chamber. This process is repeated hundreds of times until the final geometry is built in a layer-by-layer fashion. According to published data, out of the seven categories, the L-PBF and DED techniques are the most employed AM methods in the current manufacturing of metal parts as shown in Figure 1.2 [7].
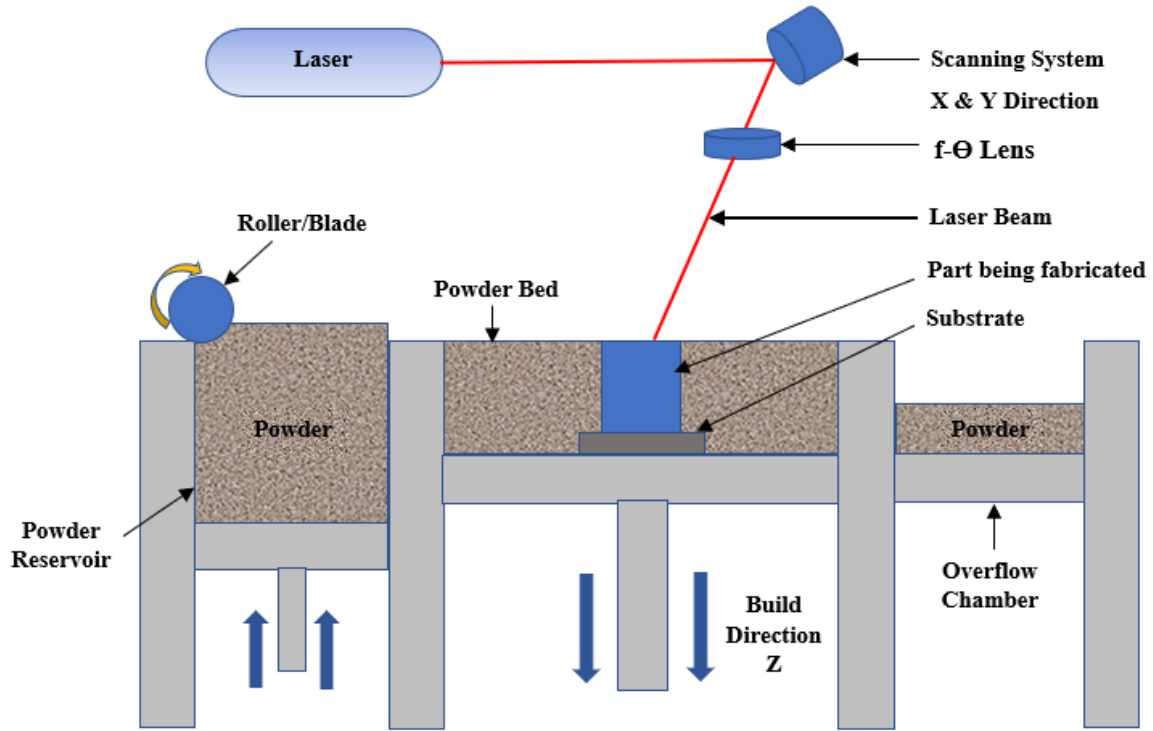
Figure 1.1. L-PBF process schematic.
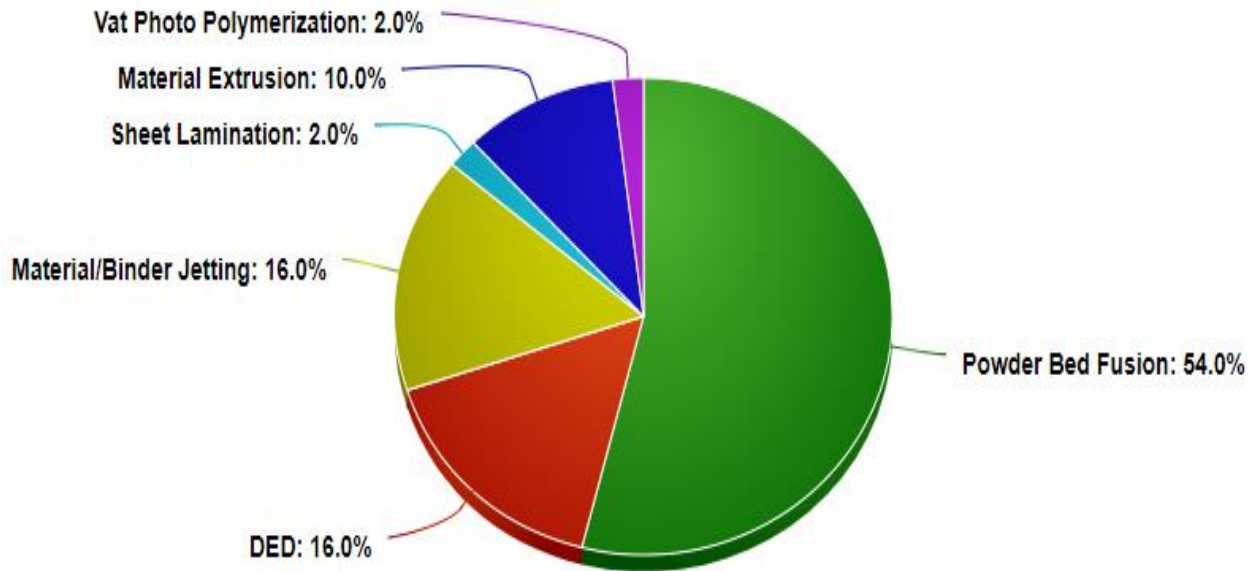
Figure 1.2. Metal AM market in 2020.

AM techniques have various process and design parameters that need to be determined to build dense parts. Some of the major process and design parameters are presented in Table 1.1. The best combination of all these parameters is determined by preparing a design of experiment and printing samples using iterative method.

Table 1.1. Different AM process and design parameters.

Process parameter	Design parameter
Laser power	Build orientation
Scan speed	Layer slicing technique
Hatch spacing	Location on substrate
Layer thickness	Support structures
Heating area	Powder shape and size

1.3 Trending applications of additive manufacturing of metals

According to reports published by the National Institute of Standards and Technology (NIST), the AM market is predicted to exceed $16.0 billion in 2025 and $196.8 billion in 2035. AM system and raw material costs comprise a substantial fraction of an AM part; however, these costs have been declining over the few last decades [8]. This has resulted in changes to vendor, manufacturer, and customer relations. The following sections are not meant to be an inclusive list of all applications of metals AM. Rather, it focuses on giving the reader an appreciation for the capability metals AM has in a range of disciplines. Specifically, the topics to be discussed are the applications of metals AM in aerospace, healthcare/medicine, and nuclear industries.

1.3.1 Aerospace industry

AM has critical impacts within the aviation industry, given that there are numerous opportunities that it can provide-design, waste reduction, and high surface finish. Through AM, it is conceivable to manufacture near-net shape useful parts in a small span of time, expanding reliability and reducing process cost. Moreover, as AM can build light weighted fully dense parts, the weight of an airplane can be diminished, increasing fuel efficiency. With an increased

utilization of unmanned aerial vehicles (UAVs) to replace crewed aircraft, there is a profound dependence on cost-effective manufacturing. For space applications, engineers can plan more advanced rocket systems that can carry a better payload or even print less-critical parts in space for future missions.

AM has been recognized as a game-changer by Airbus i.e., airplane manufacturer when it was successful in manufacturing parts with 30-55% lighter in weight. They also reported a 90% reduction in material wastage and energy consumption [9].

GE's new LEAP passenger jet engines employed fuel nozzles which were designed using additive manufacturing process. AM provided the advantage of designing these fuel nozzles with 25% lighter in weight and five times more durable. Since these fuel nozzles are complex in structure to mix and inject fuel in efficiently, AM is the only method to mass produce them [10], [11]. One of the first examples of a structural, topology optimized (TO), AM component being used for the interior on a commercial aircraft is the A350 cabin bracket connector [12]. Airbus utilized TO and L-PBF to produce the bracket build using Ti-6Al-4V in 2014.

1.3.2 Healthcare and medicine industry

The advantages that AM has to offer are being applied in fabricating surgical instruments in the healthcare industry as needed. Firstly, AM permits for manufacture of custom-designed medical device replicating the patient's anatomy [13]. It also permits the fabrication of personalized surgical instruments to fit the surgeons' hands [14]. Besides, AM can create complex tools that are not conceivable with traditional machining methods. Finally, it allows on-demand manufacture in inaccessible areas with generally lower costs and encourages mitigating the costs related to packaging and shipping. AM is also playing a key role in reshaping the hearing aid industry. Like dental manufacturing, the process of hearing aid production consists of multiple

labor-intensive steps including molding, curing, and trimming to drilling. This process is significantly shortened by AM which fabricates near-shape intricate parts without additional processes [15].

1.3.3 Nuclear Industry

The benefits of AM have been harnessed in the nuclear industry in recent decades as the demand for more powerful and safe nuclear reactors is increasing. AM components are currently being used in some critical areas of nuclear reactors. In 2021, the French company Framatome in collaboration with Oak Ridge National Laboratory developed a 3D printed fuel assembly part [16]. This fuel assembly is made of stainless steel and was installed at the Forsmark nuclear power plant in Sweden. This fuel assembly helps to hold the control rods intact.

The first 3D printed component to be incorporated in a nuclear power plant was achieved by Siemens. A 108 mm diameter metal impeller of a fire pump was installed at Krško nuclear power plant in Slovenia in 1981 [17]. Siemens used reverse engineering to build the digital twin of the original impeller and replaced the original part with the AM part. The AM part passed all the strict tests and commissions before it was installed.

1.4 Challenges in additive manufactured parts

AM is a tool that allows designers to generate custom or intricate geometries in one-building step without the limitations of conventional manufacturing techniques such as high material waste, lower design/materials freedom, need of additional tooling and molds. However, successful application of AM in industry demands identification of drawbacks in parts, and intense research of innovative approaches and strategies to mitigate the drawbacks. Drawbacks such as high expenses, limited applications in critical structures and mass production, subpar and inconsistent mechanical properties, restrictions on raw metal materials, and the presence of defects.

Through research and development, progress has been made in overcoming some of these challenges. Nevertheless, there are still a few remaining challenges that must be addressed to enhance the utilization of AM across various industries and applications. While certain challenges may be more prominent in specific AM technology methods or materials, there are a few that are prevalent across nearly all AM methods. The primary obstacles that impede the mass production of repetitive parts through AM are the extensive processing duration and elevated expenses associated with this technique. Other conventional methods can accomplish the same tasks with significantly less time and cost [18]. The following subsections address some important challenges or defects that hinder the adoption of AM metal parts in critical applications.

1.4.1 Voids and Porosity

One of the critical challenges in AM'ed metals is void and porosity formation between subsequent melted layers. Porosity in AM is a widespread concern and is often accompanied with a negative effect on the mechanical properties, especially fatigue performance [19]. Porosity is defined as the ratio of total pore volume to bulk material volume. It can be said that porosity is the Achilles' heel of metals AM. In the past, many studies have focused on comprehending the physics behind melt pool dynamics, spattering, and porosity formation [20]–[24]. Porosity formed in an L-PBF part can be categorized into several types considering the source of the formation [25]. For example, lack of fusion (LOF) of subsequent tracks and layers, keyhole induced pores, originally trapped voids in powder bed in L-PBF process, and vaporization of specific solute elements during the AM process [26]. During L-PBF, many gaps exist among the pre-packed powder particles. These cavities need to be removed from the molten pool during the melting and solidification process, which otherwise would remain as trapped voids in the selectively melted zone. Porosity can stem from process-induced defects such as initial powder impurities, evaporation or local voids

after powder-layer deposition [27]–[29]. Eventually, these pores act as strong stress raisers and finally lead to failure, especially under fatigue loading. The LOF porosity occurs when insufficient laser power is applied on the powder bed. Inadequate heat from the laser can either be due to high scan speed or low laser power for the selected powder layer thickness. LOF porosity is generally irregular in morphology and may include un-melted powder particles. The shape of the LOF porosity come in varied sizes and usually have sharp edges.

Ex situ studies of the L-PBF process have shown that the major process parameter contributor to the formation of irregular voids is low heat input [30]–[32]. Since the L-PBF process is an extremely transient and localized oriented, process parameters like laser power, scan speed, layer thickness, hatch spacing play a critical role. Overheating during changes in laser scan speed, when the scan direction is to be changed, laser stops and turns in other direction. This leads to increased melting of metal powder from the surface causing a deep keyhole depression to form. L-PBF must be performed in a controlled environment (e.g., most commonly argon or nitrogen) in order to minimize the introduction of any potential defects. L-PBF printing process of metals must be performed in a controlled environment minimizing the introduction of any potential impurities. Inert gas is also critical for proper management of any combustible spatter arising during the laser-powder particle interaction. Without the inert gas, potential fumes may be generated, and these fumes can interfere with laser beam and potential create defects in the part. The keyhole depression is unstable and can collapse and encapsulate the inert shielding gas. Examples of a keyhole and LOF porosity are shown along the cross-section of titanium (Ti) alloy fabricated using L-PBF process in Figure 1.3 and 1.4, respectively.

Figure 1.3. Example of LOF porosity in L-PBF Ti alloy. (Included with permission from
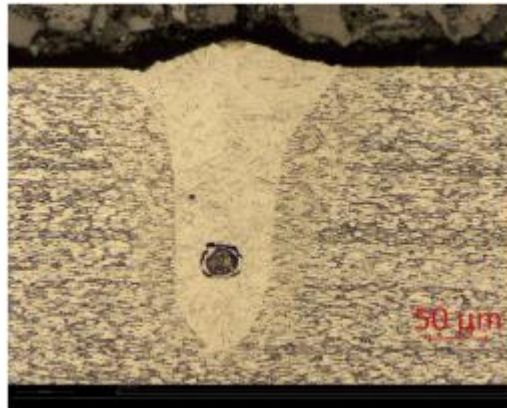
Elsevier) [33].

Figure 1.4. Example of keyhole porosity along the cross-section of L-PBF Ti alloy. (Included

with permission from Elsevier) [33].

To minimize the porosity in an L-PBF part, designers can adopt different strategies such as using optimized quality powder of desired size particles for dense packing in the powder bed [34], pre-heating the substrate to reduce the thermal gradient during the printing process, selecting correct laser power [35], [36], hatch spacing [37], build orientation [38]. If these methods are observed to have negligible effect, some post-processing techniques such as hot isostatic pressing (HIP), or heat-treatment can help reduce the porosity level or size in the part. Post-processing techniques are employed to consolidate material and closes pores within parts through the

application of heat and pressure [39]–[41]. Porosity due to keyholing in the melt pool, entrapped gases and/or lack of fusion is another ongoing issue for using L-PBF parts in critical, load-bearing applications [42]–[45]; especially since such porosity can reduce fatigue strength due to stress rising and crack initiation at pore boundaries [46]. It has been reported that porosity present on the surface level has more detrimental effects on the mechanical properties compared to the ones present in the interior of the bulk parts [47]–[49].

1.4.2 Residual Stress

Laser-based manufacturing methods such as L-PBF involve large thermal gradients in the vicinity of the targeted region due to very high heat flux required for melting the metal powder. When a new layer is irradiated with the laser beam, a portion of the incident energy is absorbed for melting the material while the rest conducts through the subsequent underlying layers or transferred to the environment. The conduction heat transfer coupled with the rapid solidification of the melt pool (around 10^5–10^6 ºC/s) results in thermal and mechanical stress in layers leading to formation of residual stress (RS) also known as 'hidden stress'. The unique rapid heating-cooling thermal cycle present in the AM process is also observed in laser welding processes where similar RS formation mechanisms are observed [50], [51]. The classic three bar example may be used to explain the RS formation mechanism [52]. Debroy *et al*. explained the origins of residual stress as a result of four stages with the help of a nickel-alloy bar-frame [53]. As shown in Figure 1.5, the middle bar and rigid box frame are initially set at room temperature. The middle bar is heated at elevated temperature and cooled off to room temperature in a relatively short time. The whole arrangement undergoes four stages comprised of elastic compression, plastic compression, elastic tensioning, and plastic tensioning. Elastic and plastic compression occurs simultaneously in the middle bar to compensate for the expansion of box-frame attached to it when heated to

higher temperatures. Similarly, elastic and plastic tensioning in the middle bar takes place to balance the compression in the box-frame when cooled down to ambient temperature. RS left unmanaged in the finished product promote to part distortion, delamination, parts built outside geometric tolerances, stress-corrosion cracking, buckling deformation, and reduced fatigue performance [53]–[59]. Hence, the formation of RS presents a major challenge in adopting AM metals in, for example, the aerospace and nuclear industries where high dimensional accuracy and mechanical performance is expected.
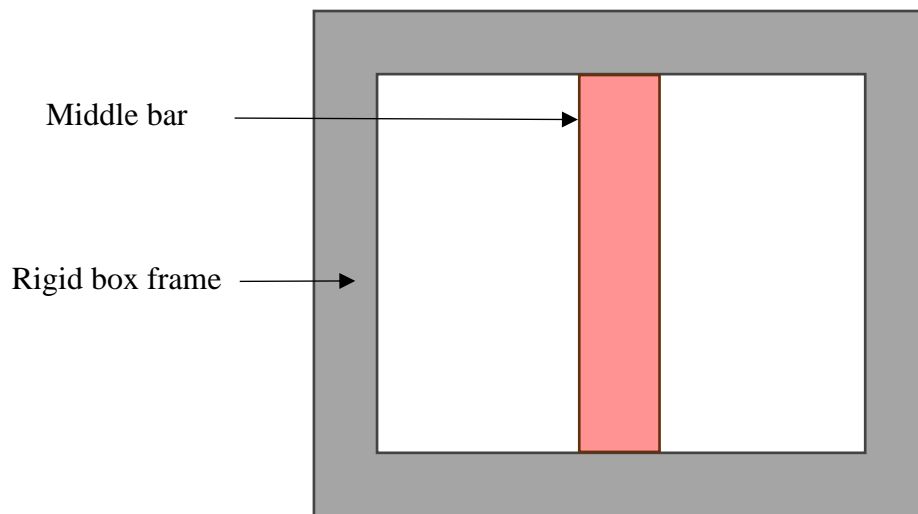
Figure 1.5. Schematic of a simple bar-frame arrangement to represent the origin of RS in AM.

Previous experimental studies have been conducted to determine the magnitude of residual stress in Inconel-series materials built in different orientations via AM. Wang and Chou investigated residual stresses formed in Inconel 718 (IN718) produced via Selective Laser Melting (SLM), an L-PBF method, using the mechanical instrumented indentation technique [60]. They found tensile and compressive residual stresses in the planes parallel and normal to the build direction, respectively. Liu *et al*. studied the residual stress formation in IN718 fabricated by L-PBF by employing the Vicker micro-indentation method. They observed a contrasting trend in

microhardness values compared to residual stress values. They also observed high residual stress values in overlapping regions of two adjacent laser pass and low residual stress values in the interior regions of single pass [61]. Barros *et al*. analyzed residual stress in L-PBF-built IN718 before and after heat treatment using a hole-drilling strain-gage method. They observed the presence of tensile residual stress on the top surface of as-built specimens while compressive residual stress existed on the top surface of solution annealed heat-treated specimens [62]. Liu *et al*. measured residual stress in stainless steel 316L L-PBF parts and demonstrated that the residual stress in the build direction is higher than that in the perpendicular direction within the material [63].

Another RS mitigation technique is using different scan strategies. Some of the common laser scan strategies used to fabricate metal parts are shown in Figure 1.6. A common method to mitigate the formation of residual stress is employing shorter scan vectors. Shorter scan vectors can be achieved using "island" scan method. Utilizing the island scan method during L-PBF process generally results in reduction of temperature gradients and residual stress. Few studies reported advantages of using island scan strategy in reducing tensile residual stress in end parts [64], [65]. Meanwhile, some studies have reported inconsistency in residual stress values when the island size is reduced beyond a certain limit [66], [67]. Build orientation also plays a vital role in mitigation of residual stress formation in L-PBF parts. Pant *et al*. plotted residual stress in Inconel 718 produced by L-PBF in three orientations (vertical, diagonal, horizontal) using a finite element (FE) based thermo-mechanical numerical mode [68]. They observed the vertical sample inherited the highest tensile residual stress followed by the diagonal and horizontal samples. Parry *et al*. reported unidirectional scan vectors may give rise to higher anisotropic residual stress compared to checkerboard or alternating scanning strategies since longer scanning paths introduce

heterogenous thermal gradients [69]. In addition to mentioned techniques to reduce residual stress, preheating the build platform and heat treatment of as-built samples are also feasible solutions [62], [70]–[72]. To understand the effects of different build orientation and heat treatment temperatures on residual stress formation in AM parts, accurate and reliable residual stress measurement NDT techniques is critical.
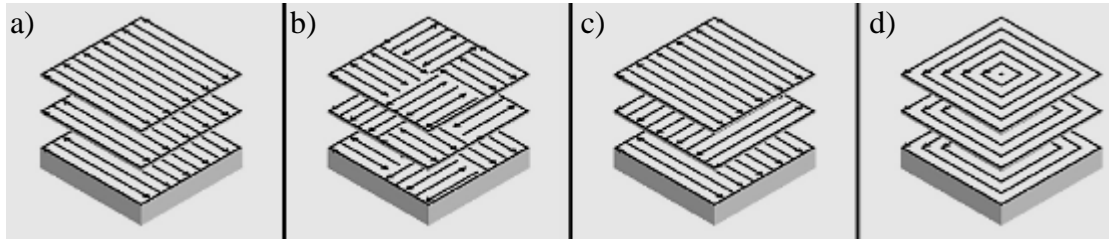
Figure 1.6. Illustration of a) zigzag, b) island, c) zigzag with rotation between layers, and d) spiral scan strategies used in AM process. (Included with permission from Elsevier) [73].

In general, measurements of residual stress can be performed via various methods and devices. Three major categories of methods are destructive, semi-destructive, and non-destructive. The different techniques that fall under these categories are presented in Figure 1.7. The penetration depth and the spatial resolution of each technique is shown in Figure 1.8. Destructive methods involve removal of a small portion of the part to understand the relaxation of RS. Some examples of destructive methods are hole drilling, core drilling, stripping, and the contour method. Destructive testing methods are comparatively easy to implement and provide accurate results, but surface destruction can be unacceptable when evaluating critical components. To prevent such surface damage, non-destructive methods have been introduced and developed. Non-destructive testing (NDT) technology has proven to be a vital and efficient tool and experienced expanded adoption, becoming the main RS measurement method for the future. NDT can involve X-ray, neutrons, synchrotron radiation, and magnetic strain [74]. X-ray diffraction (XRD) is the most widely and matured technology among all NDT to measure RS along or near a surface due to its

high accuracy and low penetration depth. Measuring RS in material using XRD requires the grain size to be less than 100 μm. On the other hand, neutron diffraction method is used to measure RS by measuring the change in interplanar spacing d in the interior of the samples. The neutron diffraction method provides volumetric stress fields because of its high penetration depth. Masoomi *et al*. used neutron diffraction to measure the residual stress distribution in L-PBF stainless steel 17-4 PH [75]. The study required several hours of neutron exposure at specific regions along the samples. It was found that heat treating vertically built cylinders reduces compressive axial stress in the core region.
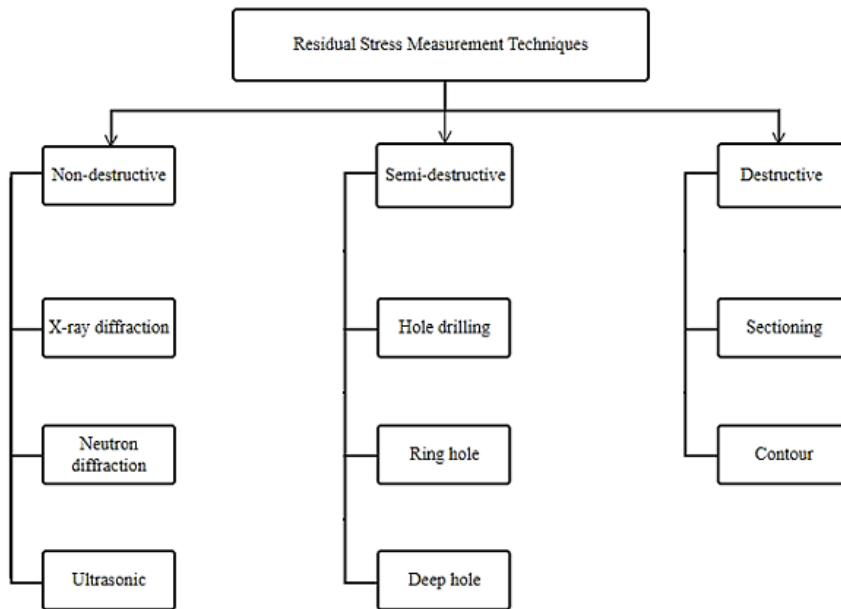
Figure 1.7. Different RS measurement techniques.
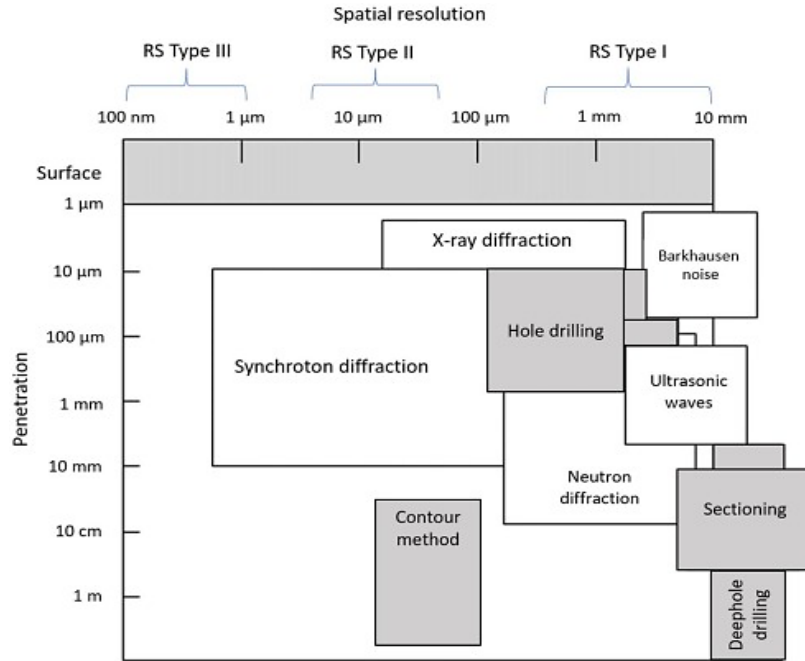
Figure 1.8. Penetration depth and spatial resolution of different RS measurement techniques.

(Included with permission from Elsevier) [76].

RS type I, also known as macro residual stress, refers to stress with a spatial scale larger than the grain size, typically exceeding 1 mm. Disruption of the self-balanced state of macro residual stress can lead to changes in the overall size of the component.

RS type II, also referred to as intergranular residual stress, exists within the range of multiple grains, typically ranging from 0.01 mm to 1.0 mm. Alterations in intergranular residual stress can result in corresponding changes in the macroscopic size of the component.

RS type III is confined to the crystal grain range and is generated within the crystal due to the consistency of grain boundaries and the stress field caused by dislocations on an atomic scale. The length range of type III residual stress is generally less than 0.01 mm.

As seen in Figure 1.8., the XRD technique is the most effective and non-destructive to measure RS on surface and sub-surface level. RS on the metal surface is critical in defining the mechanical properties of the bulk sample. XRD typically relies on using the traditional $\sin^2\Psi$

method for calculating stresses. The XRD-$\sin^2\Psi$ stress method begins with XRD scans along series

of defined incident angles (Ψ) over a pre-determined diffraction angle. From the scans performed

at each incident angle, the selected diffraction peak position must be accurately verified, i.e., the

2θ value must be measured from a very wide-ranging and sometimes unevenly shaped peak. The

obtained 2θ values are then used to execute the linear regression to obtain the slope and intercept

values to be used for the stress calculation. Line detectors are usually used in the $\sin^2\Psi$ method

which captures a small part of the Debye-Scherrer (D-S) ring at every incident angle (Ψ). The D-

S ring is created by a diffraction pattern occurring due to Braggs law when X-rays are incident on

a polycrystalline material. To eliminate the additional time for data collection, in 1978, the Cos α

method was developed in Japan. This method is also known as single exposure method and has

gained attention as a new method to measure residual stress. The Cos α method employs the entire

D-S ring produced from single exposure of X-rays at a single incident X-ray beam angle captured

by a 2-D detector. The stress is calculated by comparing the D-S ring obtained from the stressed

specimen to the D-S ring of unstressed specimen. The cos α method has several advantages over

the traditional $\sin^2\Psi$ method such as simple optical setup and faster in-plane normal and shear

stress calculations [77]. Past studies have proven the reliability of the cos α method by comparing

measured residual stress values with those obtained via the traditional $\sin^2\Psi$ method [77][78][79].

Delbergue *et al*. performed a comparison study between the two X-ray residual stress

measurements through the X-ray elastic constant in quenched and tempered martensite steels [80].

They found the cos α method yielded better repeatability in results compared to the $\sin^2\Psi$ method.

The difference between two X-ray stress measurement techniques is presented schematically in

Figure 1.9.
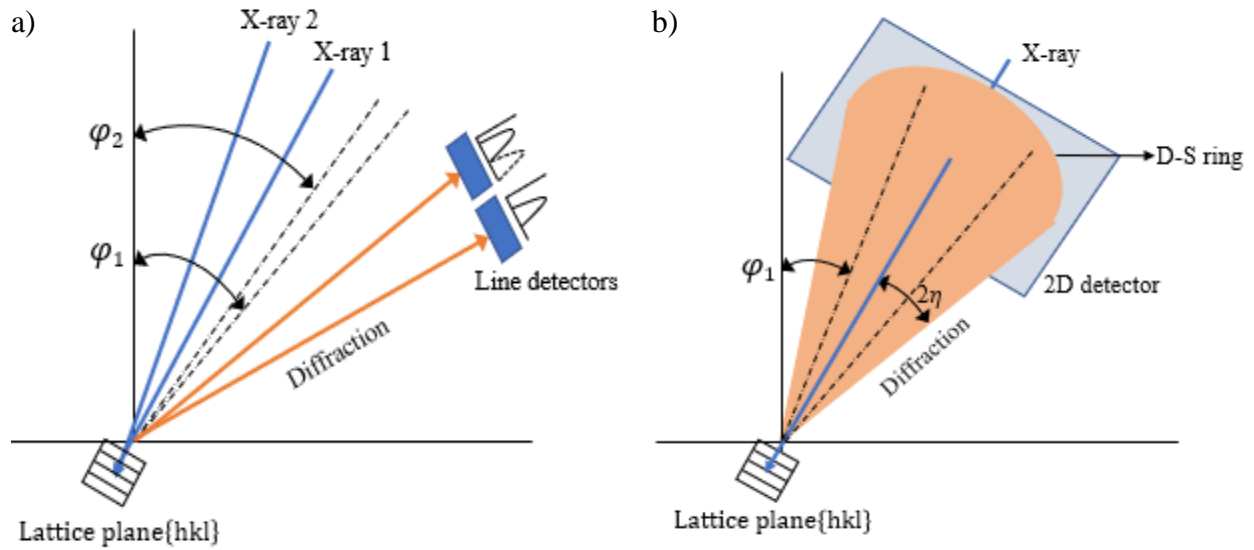
Figure 1.9. Schematic of two X-ray residual stress measurement techniques: a) sin²Ψ and b) cos α.

1.4.3 Anisotropic microstructure and mechanical properties

One of the serious challenges of AM metals is the anisotropic microstructure and mechanical properties in its produced parts. Isotropic materials show the same properties in all directions, while anisotropic materials show different properties in various directions. Parts are built in layer-by-layer fashion during metals AM. Microstructure variation in every layer is caused due to the different thermal history experienced by each layer. In addition, the thermal gradient experienced by the boundaries of each layer is different than the material inside the bulk volume. The heat from the AM laser is conducted primarily in the vertical direction fusing the new layer with layers underneath. This creates a long columnar grain in the microstructure of AM metals. For a component to be successfully employed in engineering application, it should possess superior and uniform properties in all directions. Materials with anisotropic microstructure have a higher tendency of failure under multi-directional stresses. The columnar grains are coarse in morphology. In contrast to columnar grains, equiaxed grains are finer and with more homogenous

mechanical properties [81]. Equiaxed grains promote mechanical properties such as ductility and fracture toughness. There have been several studies conducted in the past focusing on the microstructure of AM metals [82]–[85].

AM technologies are convenient to fabricate complex, small batch, critical, parts made from superalloys or refractory metals. Nickel-based superalloys such as Inconel 625 (IN625) and Inconel 718 (IN718) are notoriously difficult to process via conventional metallurgical methods due to their extreme hardness value, low thermal conductivity, low elastic modulus, and abrasive wear chips. In addition, formation of secondary inter-metallic phases in these alloys makes it tougher resulting in tool wear during machining [86]–[88]. For these reasons, many industries/users are looking at AM for processing Inconel parts. Inconel is used to build critical parts in harsh environments like aerospace, automotive, chemical, and nuclear reactors, where a high level of mechanical strength is expected at elevated temperatures.

IN625 is a nickel-based face centered cubic superalloy. It is also known as a solid-solution strengthening alloy which derives its strength from the presence of refractory metals such as niobium (Nb) and molybdenum (Mo) in Ni-Cr matrix. A large amount of literature explains that in the as-built condition, the interdendritic regions of AM IN625 are enriched with Nb and Mo [89]–[92]. Performing heat-treatment at different temperatures creates distinct types of precipitates. IN625 is sensitive to create precipitates such as Ni_3M γ" phase, Ni_3M δ phase, and Ni_2 (Cr, Mo) Laves phase as well as MC primary carbides and M_6C and $M_{23}C_6$ secondary carbides [93]–[95].

On the other hand, IN718 is a precipitation-hardening superalloy with the main hardening phases being body-centered tetragonal D022-ordered γ" (Ni_3Nb). Typically, γ" (Ni_3Nb) occupies 15-20% of the volume fraction in a IN718 part [96]. Exposure to elevated temperature and a

particular time, converts the metastable γ" (Ni_3Nb) phase to stable δ phase [96], [97]. The large presence of δ phase in the microstructure in results in undesirable mechanical properties such as reduction in ductility [98]–[100]. The δ phase has some advantages such as it helps to pin down the grain boundaries, resulting in the solid control of grain size during the high temperature applications [101], [102]. IN625 and IN718 share many properties with the other alloys in the Inconel family. The key difference between IN625 and IN718 alloy is primarily in their elemental composition. IN625 has higher chromium (Cr) compared to IN718 alloy which gives it enhanced corrosion resistance property. On the other hand, IN718 is known for its high strength property. IN718 alloy approximately has three times the iron (Fe) content compared to IN625 alloy. Moreover, IN718 has a higher composition of niobium (Nb) which contributes to its high strength property.

Performing heat treatment on these alloys allows for transformation of microstructure and eventually change their mechanical properties. Heat treatment is the simultaneous, controlled heating and cooling of pure and alloy metals with the goal of altering their crystalline structure. Heat treating the as-built L-PBF IN625 and IN718 samples for different durations and at different temperatures creates different forms of precipitates which modify the mechanical properties of the end part. There are four common ways of performing heat treatment process:

1) Annealing: Involves heating the material to change the microstructure and ultimately improve its ductility. This process allows the material to be molded more easily without failure. The material is heated at a particular temperature and held for some period. This results in self-reparation of any present defects. Finally, the material is cooled down to room temperature at a steady slow rate.

2) Hardening: This process is performed to increase the hardness of the material. Firstly, the material is heated to a temperature at which the microstructure changes without melting the material. The material is left at that temperature for a few hours and is followed by rapid cooling.

3) Quenching: This process is comparable to the hardening process, except the rapid cooling stage is performed using one of the several quenching materials like air, water, and brine.

4) Stress relieving: This process involves heating and air cooling at a particular rate. Using this process, internal stress i.e., residual stress can be mitigated which ultimately improves the strength of the material.

1.4.4 Texture

Laser-based AM combines high thermal gradients and high solidification rates which results in the formation of a highly textured microstructure. Texture in AM parts is the geometrical irregularities present at a surface. Texture does not include those geometrical irregularities contributing to the form or shape of the surface. Texture is the distribution of crystallographic orientations of grains in the microstructure. Texture is observed in almost all engineered materials and can have a detrimental effect on materials properties. Material with a dominant grain orientation in the microstructure is known to have high texture. The characteristics of the texture in AM metals are determined by a collective effect of laser scan speed, laser power, powder particle size, and powder layer thickness. Controlling these parameters during the AM process provides an opportunity to obtain optimized texture in the part. Past studies have been conducted to investigate the formation of different crystallographic textures from varying process parameters [103]–[107]. L-PBF metal part's texture is dominated by the presence of grains oriented in the <001> direction

parallel to the build direction due to high heat dissipation in the build direction which leads to anisotropic mechanical properties in longitudinal and lateral directions [108]–[111]. Performing heat treatment on as-built AM parts at different temperatures and time helps in recrystallization of grains by orienting in random directions and ultimately reducing the overall texture [92], [93], [111]–[113]. Heating the microstructure at high temperature but below the material's melting point allows the grains to reorganize in random directions since the heat is applied uniformly through all directions. Inverse pole figure (IPF) maps are used to demonstrate the crystallographic texture of polycrystalline material. IPF maps are generated using electron backscattered diffraction method (EBSD) detector attached to the scanning electron microscope (SEM) system. Some examples of IPF maps of sample printed in vertical direction shows grains oriented along the build direction (BD) are shown in Figures 1.10 (a) and (b).
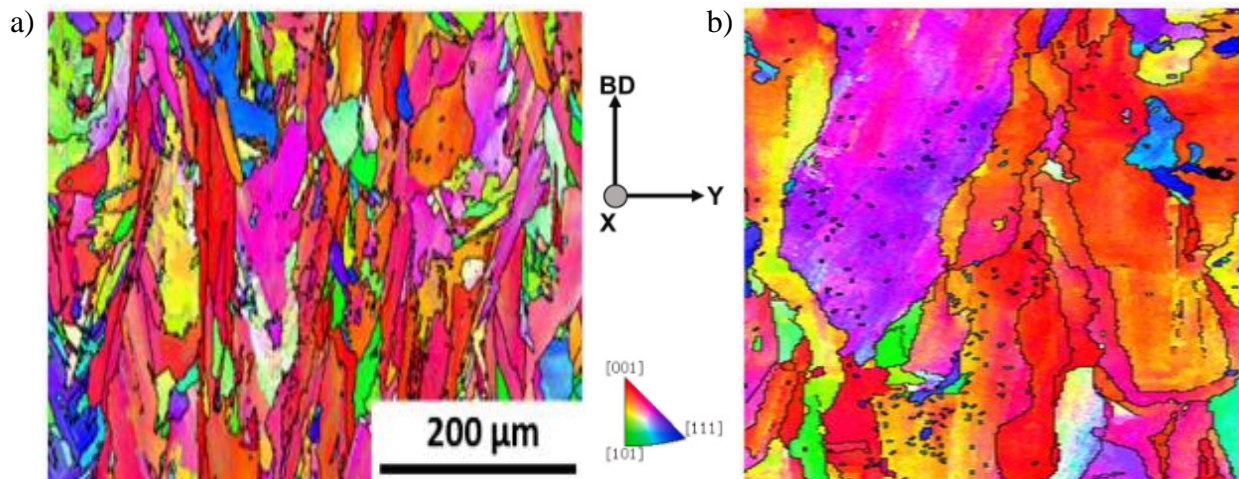
Figure 1.10. Example of EBSD generated IPF maps representing the grain orientated in <001> direction observed in a) IN718 and b) IN625 (Included with permission from Elsevier) [114][110].

1.4.5 Hardness testing

Hardness also has a close relationship to other mechanical properties like strength, ductility, and fatigue resistance, and therefore, hardness testing can be used as a simple, fast, and relatively cheap material quality control method [115]. Hardness testing is important for ensuring that the metal to be employed in a critical application meets the standards of performance. The hardness value of a metal indicates its ability to resist plastic deformation, penetration, indentation, and scratching. Certainly, the importance of the hardness data cannot be underestimated. This information can be used alongside other material property estimation techniques, like tensile or compression tests. Some of the earliest forms of hardness testing methods were introduced in the 1820's, including scratching the material's surface with diamond and measuring the width of the scratch line. Later, with the development of techniques, indentation-type hardness was invented in the 1850's. Since then, several other advanced and accurate types of hardness testing methods have been developed. The shape of the indenter, indentation, and the formulae for calculating hardness values are summarized in Figure 1.11.
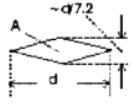
Figure 1.11. Geometrical shape of indenter and projected indentation along with hardness formula and penetration depths for different indenters [116].

22

The Vickers hardness test was developed in 1924 by Smith and Sandland at Vickers Ltd, a British Engineering corporation. The hardness of a solid material can be defined as a measure of its resistance to a permanent shape change when a constant compressive force is applied. Vickers hardness testing uses a pyramidal indenter and a load-on, load-off procedure, which gives geometrically similar impressions regardless of the penetration depth. Two characteristic lengths are measured on the Vickers indent, the indent diagonals, and an average diagonal length is used to calculate the impression area. Load divided by area gives a Vickers hardness number. This is explained with equation (1.1).

$$\text{HV} = 2\sin(68°)\left(\frac{F}{D^2}\right) = 1.85\left(\frac{F}{D^2}\right) \tag{1.1}$$

where F is the indentation load applied by the hardness tester, D is the average diagonal length of the indentation impression made on the material. The load range applicable in a Vickers hardness tester is between 1 gram force (gf) to 120 kgf. The indenter is made of diamond and the base is in the form of a square-based pyramid having an angle of 136° between faces. The sample preparation and the measurement procedure are standardized under ASTM E92-23 [117].

1.5 Nuclear damage in metals

The global population is projected to increase from 8 billion to over 9 billion by the year 2050 [118]. Humans strive for an improved quality of life all the time. As the world's population is rising, so is the demand for energy for basic applications. The increased usage of energy provides additional benefits such as enhanced standards of living, improved healthcare and longevity, increased literacy, and opportunities. However, simply expanding the use of energy through the same production process and technologies as in current market will raise risk and concerns regarding the climate change and the depletion of fossil resources. To ensure the Earth can sustain the human development while supporting its population, it is necessary to increase the stake of

energy supplies that are green, safe, cost-effective, and capable of serving both basic electricity production and other primary energy needs [119]. Nuclear energy is a prominent example of such a non-greenhouse-gas-emitting power supply.

According to the U.S. Energy Information Administration (EIA) for 2022, nuclear energy contributed about 18% of the total electricity produced in the USA. The Generation IV International Forum (GIF) and the IAEA International Project on Innovative Nuclear Reactors (INPRO) are working towards reevaluating manufacturing technologies to develop attractive, safe commercial nuclear systems [120], [121]. In 2001, the GIF organization proposed to build six futuristic nuclear reactor designs. Out of these six designs, four will be operated using fast neutron spectrum (E > 1 MeV) and one will use thermal neutrons (E > 0.025 eV) for its fusion reactions. The details about the designs of these six conceptual reactors are explained in chapter by B. Zohuri [122]. Generation IV (GEN IV) reactors are proposed and designed to operate at higher radiation doses and temperatures than the current GEN III nuclear reactors. Understanding materials response to harsh neutron irradiation doses and service environments such as elevated temperatures is becoming increasingly crucial in the design, development, and operation of GEN IV nuclear reactor systems. Along with the GEN IV reactors, small modular (SMRs) nuclear fission reactors are also considered the next transformative technology in the nuclear industry. SMR is perceived as a more efficient and effective way of producing energy. The maximum capacity of SMRs is up to 300 MW(e) per unit which is one-third of a traditional nuclear reactor. Small modular reactors have benefits such as less expensive than a normal large reactor and the ability to automate the energy production process resulting in lower labor cost and human error [123][124].

Some of the characteristics SMRs are as follows [125]–[128]: (1) Built completely in a factory and installed on-site; (2) Easily and quickly shipped to and from the site; (3) Self-regulating with a high degree of safety; (4) Capable of operating for years without refueling.

There are different types of nuclear reactors. There are different types of neutrons depending on their kinetic energy. Some of the neutron forms are cold, thermal, epithermal, intermediate, and fast neutrons. The neutron forms are classified by the kinetic energy they possess when they travel through a material. The maximum kinetic energy (in eV) of these neutrons are shown in Table 1.2.

Table 1.2. Different types of neutrons depending on their kinetic energy (eV)

Type	Energy (eV)
Cold	0.005
Thermal	0.025
Epithermal	1
Intermediate	10^4
Fast	10^6

According to the GIF focus points, out of the six concept designs proposed, four will be based on fast neutron reactors. Neutrons produced during fission reactions with energy more than 0.1 MeV are known as fast neutrons. Fast reactors employing fast neutrons can provide significant advantage over the current slow or thermal neutron (E < 0.025 eV) reactors [122]. In fast neutron reactors, natural uranium is burned 60 times more efficiently than a normal reactor. Natural uranium (0.7% U-235 and 99.3% U-238) is burned directly by fast neutrons without it being converted to plutonium isotopes eventually utilizing uranium at maximum level. This will help to reduce the scarcity of natural uranium all over the world. Moreover, fast reactors have smaller

cores and higher power density compared to normal reactors. Even though fast reactors are researched to provide significant advantages over current nuclear reactors, there is a shortage of commercial and research fast reactors in the USA.

For the successful construction of the key technologies key components for advanced nuclear systems, demand is high for structural materials to be used for building in-core and out-core components of GEN IV/SMRs reactors that can withstand high operating temperatures and radiation doses to improve the life and safety of the reactor. Nuclear reactors exhibit a harsh environment for a component regardless of the type of reactor. The components inside and outside the core of the reactor are exposed to different mechanical and thermal stress, vibration, intense flux of neutrons, and thermal gradients. The advanced reactor concepts need corresponding innovation in materials to meet the demand of increased neutron flux and doses in the reactor. Fabrication of these complex components using conventional machining methods pose challenges such as poor material machinability, excessive tool wear, and numerous post processing requirements, etc. Therefore, there is a high demand for materials that can tolerate high neutron doses, damage, and possess high resistance towards neutron irradiation-induced defects in microstructure and mechanical properties. To build complex structures with advanced materials, AM can serve as an alternative tool to fabricate near-net-shaped components with desirable properties. AM provides better control during manufacturing process with help of advanced computer technologies, in-situ monitoring, artificial intelligence (AI) that provide real-time feedback and parameter analysis [129].

Neutron bombardment on any material causes detrimental changes in the microstructure and ultimately affects the mechanical properties. The defects formed in the target material can be

classified into either zero, one, two, or three dimensional. Each class of the defects is presented in Figure 1.12. Some of the defects are explained below in detail:

Types of defects			
Point defect (0D) • Vacancy • Interstitial • Frenkel pair	Line defect (1D) • Edge dislocation • Screw dislocation	Surface defect (2D) • Grain boundary • Twin boundary	Volume defect (3D) • Voids grain boundary • Twin boundary
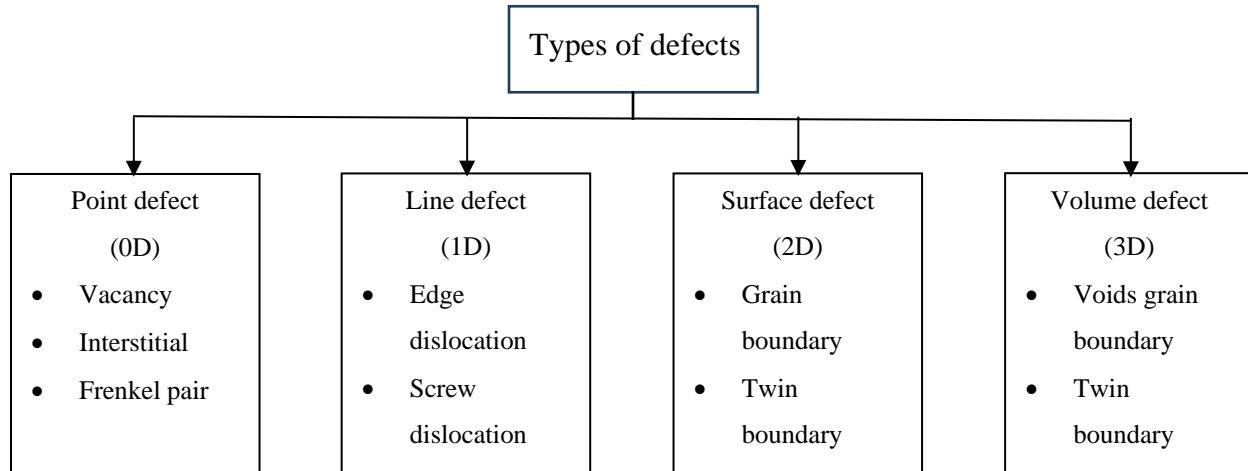
Figure 1.12. Different categories of defects in a material.

1.5.1 Point defects

The research of radiation effects has been established as a critical field of interest in mechanical engineering as it affects mechanical properties of high-value parts. This interest is driven by two crucial factors. Firstly, radiation-induced controlled quantity of point defects (zero dimensional) such as voids, and interstitials gives opportunity to study the material containing them. Secondly, the quality and performance of nuclear reactors built over the last decades is affected by severe exposure of high neutron fluences.

The displacement of atoms from their lattice sites can be achieved through energy transfer of a few tens of electron volts. However, in a typical reactor, neutrons possess energies of a few hundred keV, which enables them to transfer energy that exceeds the displacement threshold of lattice atoms. The primary recoil atom, which is displaced because of neutron interaction, interacts with the surrounding atoms, thereby transferring energy to them and gradually coming to rest. It

is noteworthy that many of these energy transfers are capable of displacing additional atoms, which, in turn, may displace other atoms. This creates a cascade of displacement. Due to this displacement cascade, atoms may be transported by considerable distance. The traveled atoms create vacancy and interstitials at the same time. This can create a cluster of vacancies and interstitials that travel within the microstructure of the material. The combination of the vacancy and interstitials formed by the displacement atom is referred to as a Frenkel pair and is shown in Figure 1.13. This phenomenon leads to a branching displacement cascade that encompasses a region around the path of the primary recoil. The ejected atom from its original position due to elastic collision i.e., only nuclear interaction with the energetic neutron is known as primary knock-on atom (PKA). Some of the PKA's can further lead to secondary knock on resulting in a collision cascade. These defects (vacancies and interstitials) are produced along the tracks of the incident charged particle. The scale and shape of the cascade depends on the charged particle energy, atomic number of the target material, and type of the charged particle [130].
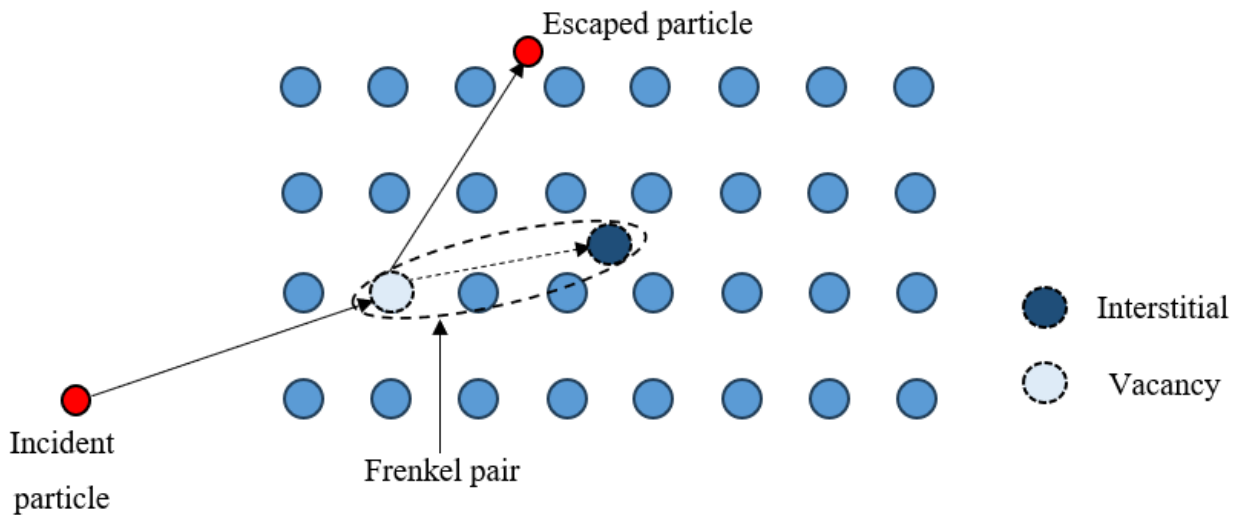
Figure 1.13. Formation of a Frenkel pair due to the elastic collision of energetic particle and lattice atom.

1.5.2 Radiation hardening/embrittlement

The volume of Frenkel pairs generated in the microstructure of an irradiated material depends on irradiation parameters and target material properties. Irradiation parameters include variables such as irradiation time, irradiation fluence, incident particle energy and fluence, and irradiation temperature, etc. Material properties include pre-existing defects in the target material, chemical composition, and so on [131]–[133]. The primary knocked lattice atoms may further interact with neighboring atoms and transfer kinetic energy to the next atoms. This creates a damage cascade in the microstructure. The displaced atoms (interstitials) may either occupy the vacancy site, or they combine with other interstitial atoms and grow in density and ultimately form a larger defect. Large vacancy defect formation process occurs in similar manner [134]. The large cluster of vacancies and interstitials formed are most likely to nucleate at the grain boundaries (GBs). Collectively, the vacancy and interstitial clusters form an aligned array which is known as a dislocation loop. These point defect clusters in the microstructure are the primary contributors to the irradiation-induced hardening macroscopic defect to the mechanical properties of the target material. It is well established that the irradiation-induced hardening of metallic materials is attributed to different irradiation-induced defects such as point defects, dislocation line, dislocation loops, etc. Dong *et al*, performed the in-situ characterization of dislocation evolution during the irradiation. As observed in Figures 1.14. and 1.15., they observed the dislocation density increased with the increase in the irradiation dose and temperature, respectively [135]. Dong *et al*. also provided in-situ videos recorded of the dislocation evolution as the supplementary data. Several studies have been conducted to show different metals experienced irradiation-induced hardening defect [136]–[139]. There are two main ways irradiation hardens a metal [140]:

1) Firstly, the irradiation-induced dislocations combine with the existing dislocation present in the material, which results in an overall increase in dislocation density. The microstructure filled with dislocation inhibits the motion of the neighboring dislocation under the external load. This type of hardening is called source hardening.

2) Secondly, the hardening occurs in metals due to the formation of new defects such as voids and precipitates. This further hinders the motion of dislocation under the external force. This type of hardening is called friction hardening.
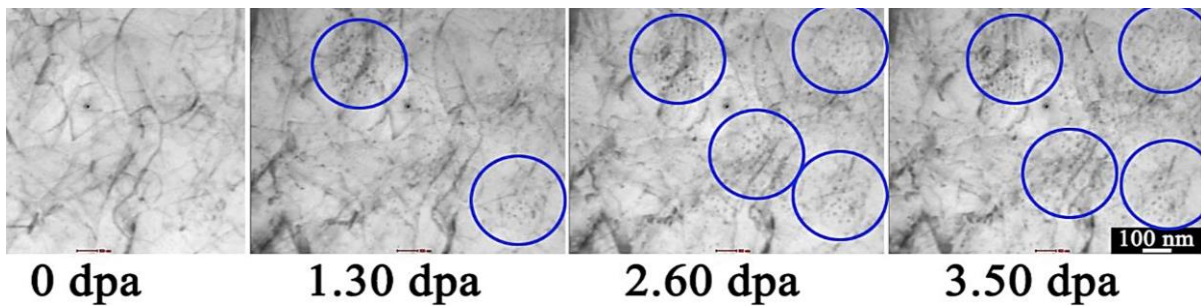
Figure 1.14. Evolution of dislocation (dark lines) after increasing the irradiation dose indicated by displacement per atom (dpa) value. Blue rings highlight the regions used for comparison (Included with permission from Elsevier) [135].
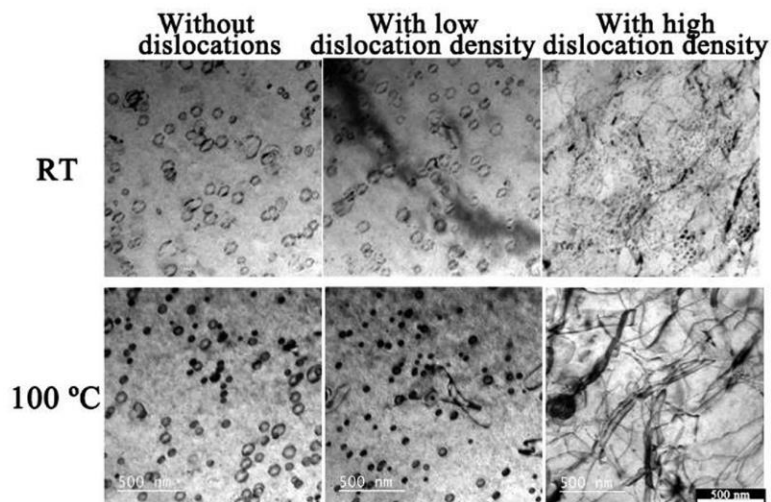
Figure 1.15. Evolution of dislocation (dark spots) after increasing the irradiation temperature (Included with permission from Elsevier) [135].

1.6 Gaps and objectives

Neutron irradiation on metal imposes damage that affects its performance over long periods of exposure. One of the irradiation damage types is hardening where the hardness of the irradiated components increases. Many previous studies have investigated neutron irradiation damage in conventionally-built metals. There is limited research data available on neutron irradiation damage on nickel-superalloys fabricated using AM. This is hindering the certification of AM materials for their application in the nuclear industry. The main goal of this dissertation is to tailor the properties of AM metal to make it as resistance or more towards the nuclear irradiation hardening damage in compared to conventionally built metal. The major objectives of this dissertation to achieve the goal are:

1. Determine how to mitigate residual stress and porosity defects by using different L-PBF build orientations and post-processing heat-treatment schedules to make L-PBF nickel superalloys safer for nuclear energy applications.

2. Discover how AM metals can be tailored to make them more tolerant towards full-spectrum and fast neutron irradiation induced hardening compared to their wrought counterparts.

1.7 The outline of the dissertation

The rest of this dissertation is arranged in the following manner: Chapter 2 introduces the AM process parameters for IN625 samples, heat treatment process employed, build orientation effects, residual stress measurement and analysis using a novel method, and microstructure analysis (microstructure texture, grain misorientation) via using EBSD. Chapter 3 investigates the full-spectrum neutron irradiation process of L-PBF and wrought IN625 samples. The chapter discusses the neutron irradiation parameters, sample placement in the reactor, measuring microhardness before and after irradiation, and pre-irradiation porosity effects on the post-

irradiation microhardness results. Chapter 4 discusses the fast neutron irradiation process, fast neutron irradiation effects on IN625 and IN718 samples, and the comparison of radiation damage levels in L-PBF and wrought samples. Chapter 5 summarizes the major conclusions drawn from all previous chapters and future work.

Chapter 2 - Residual Stress in Inconel 625

The aim of the work presented in this chapter was to understand the effects of two build orientations i.e., vertical, and diagonal, and heat treatment on surface residual stress of IN625 samples fabricated using L-PBF. Along with the influence on residual stress, the microstructure evolution in the part AM'ed in the two different build orientations and heat treatment temperatures was investigated. The 'Cos α method' was used to quantify residual stress by capturing the D-S ring from a single exposure to X-rays. Residual stress was calculated by using the D-S ring distortion from a stress-free IN625 sample and comparing it with the radius of the D-S ring of the as-built and heat-treated IN625 samples. Heat treatment was conducted on the as-built IN625 samples for one hour. EBSD was performed on as-built, heat-treated, and wrought IN625 samples to understand the changes in texture, grain morphology, misorientation and recrystallization which have influence on residual stress. Kernell average misorientation (KAM) maps were captured to estimate the local strains in the microstructure. The effect of build orientation and heat treatment on grain morphology and recrystallization is supported by nano-indentation measurements. All these results are correlated and discussed to understand the overall findings in this study.

2.1 Experimental methods

2.1.1 AM process for IN625

Gas atomized IN625 powder with a mean particle diameter of 31.3 µm was sourced from Carpenter Technologies. The powder morphology is shown in Figures 2.1 (a) and (b) obtained by using a scanning electron microscope (SEM). IN625 samples were built using a Concept Laser Mlab Cusing 100R commercial L-PBF system. This L-PBF system was equipped with a 100 W fiber laser (Nd:YAG) at a wavelength of 1070 nm. Fabrication was conducted in an enclosed high-purity argon atmosphere to avoid any oxidation while also providing a uniform supply of powder.

The elemental composition (in % wt) of the employed, virgin IN625 powder and wrought IN625 is shown in Table 2.1. The elemental composition complies with the ASTM F3056-14 (21) or UNS N06625 standard presented in Table 2.1. Several IN625 cubes were printed using different sets of process parameters. Each cube was checked for density to obtain the optimized set of process parameters. The density of different cubes built using different scan speeds (mm/s) and laser powers (W) is shown in Figure 2.2. IN625 samples were additively manufactured using process parameters as follows: power = 90 W, scan speed = 800 mm/s, laser diameter = 80 µm, layer thickness = 25 µm, and hatch spacing = 80 µm. These parameters were found to produce samples with 99.8% density. Cube IN625 samples of size 10 mm^3 were built using the above-mentioned L-PBF process parameters. Samples were built in the vertical and diagonal orientations as seen in Figure 2.3. Island scanning strategy with a checkerboard pattern consisting of 5×5 mm squares was used. Each island consisted of scan tracks that alternated in opposite directions. The laser rotated by 90° for each island. The laser scan strategy used to build samples is shown in Figure 2.4. The as-built IN625 samples were heat treated at three different temperatures of 700 ℃, 900 ℃, and 1050 ℃ for 1-hour each. The rationale for using these temperatures was to study how residual stress varies with the precipitation of the γ'' and δ phases, as well as with recrystallization of grains in the additively manufactured IN625 [141]. The heating rate used during heat treatment was ~5 ℃/min. All three heat-treated samples were exposed to air cooling to bring their temperatures to ambient temperature while remaining in the furnace. The uncertainty in heat treatment temperatures is ± 5 ℃. For experimental control and baselining, wrought IN625 plate (152.4 x 152.4 x 4.76 mm^3) was acquired from Metalmen, NY, USA. The plate was produced according to the AMS5599 standard. Small 1 x 1 x 0.5 mm samples were sectioned from the plate using wire electrical discharge machining (EDM).
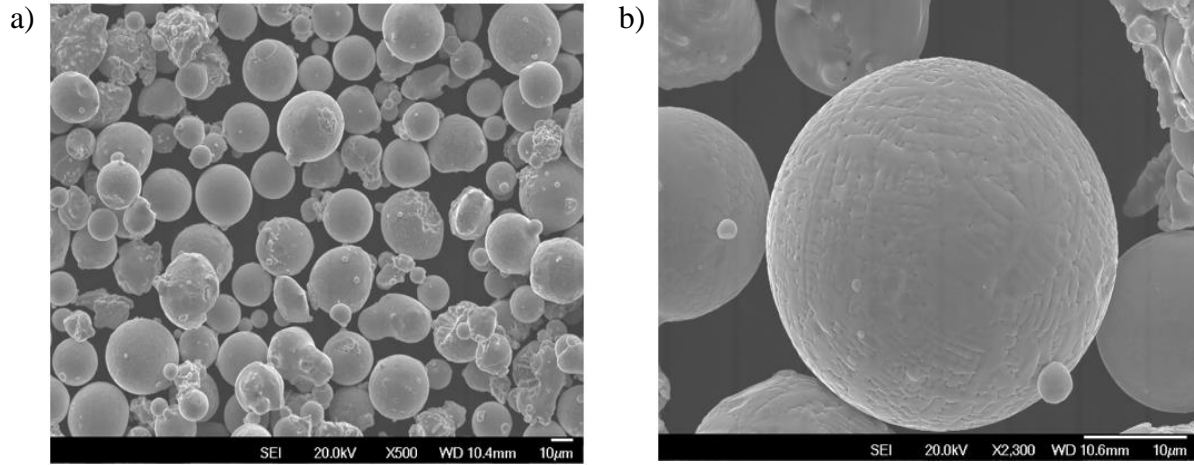
Figure 2.1. SEM of gas atomized IN625 powder showing sphericity. The scale is shown on the bottom right.
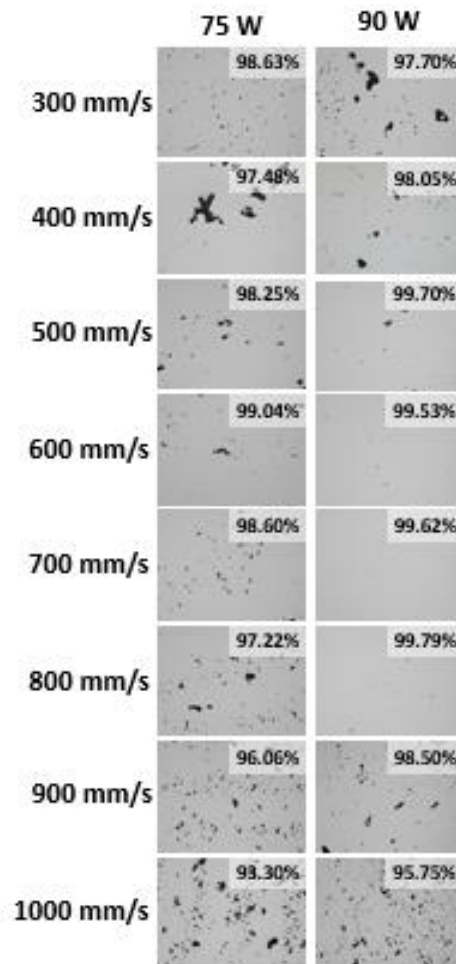
Figure 2.2. Percent density of different IN625 cubes built using different scan speed and laser power.

Table 2.1. Elemental composition of L-PBF IN625 powder, wrought IN625, and UNS standard.

% wt.	Ni	Cr	Mo	Fe	Nb+Ta	Co	C	Al	Ti	Mn
UNS N06625	Bal	20-23	8-10	<5.0	3.15-4.15	<1	<0.1	<0.4	<0.4	<0.5
L-PBF	Bal	21.59	9.0	2.95	3.55	0.03	0.04	0.1	0.1	<0.5
Wrought	Bal	22.08	8.52	4.35	3.41	0.05	0.05	0.24	0.22	0.35
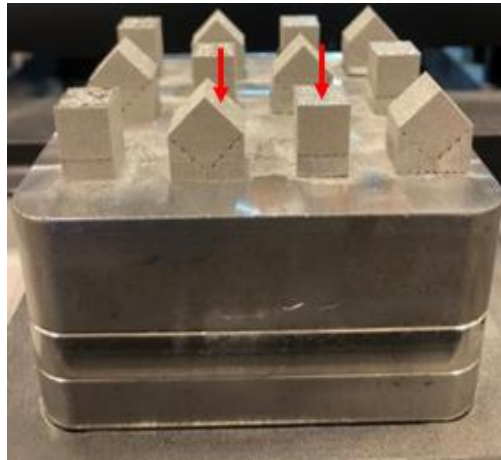
Figure 2.3. Vertically and diagonally built L-PBF IN625 samples on build platform. Red arrows indicate the face used for analysis [1].
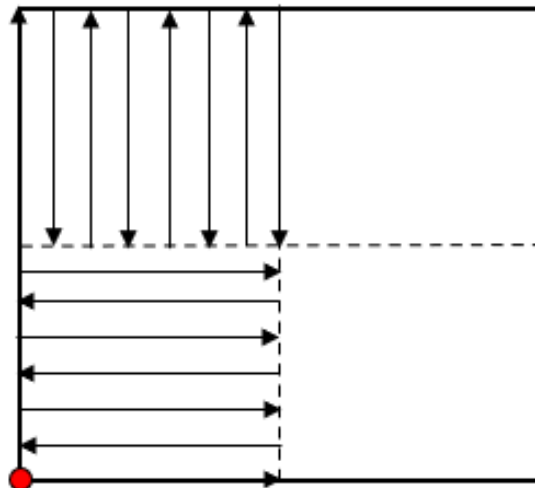
Figure 2.4. Island laser scan strategy used to melt individual powder layers. Red dot indicates the laser start point.

2.1.2 X-ray diffraction residual stress measurement

The X-ray diffraction (XRD) technique is most common technique to measure near surface residual stress as the penetration depth of X-ray is low – on-the-order of 10 μm. In this study, residual stress measurements were conducted using a portable Pulstec μ-X360 X-ray system. The samples were irradiated using a beam current of 0.66 mA and voltage of 30 kV. The X-ray beam was directed to be incident on each sample at an angle of 28.8 degrees. The distance from the specimen and detector to capture the Debye - Scherrer (D-S) ring image was set to D = 50 mm. The X-ray Manganese (Mn) *K*-alpha wavelength (λ) used for X-ray diffraction was 2.10 Å. The diffraction angle (2θ) was calculated using Bragg's law presented in equation 2.1, i.e.:

$$n\lambda = 2d\sin\theta \tag{2.1}$$

where *n* is an integer and *d* is the d-spacing or interplanar spacing equal to 1.077 Å for IN625. Using the above values, the diffraction angle was calculated as 155.03 degrees.

The μ-X360 X-ray Pulstec system utilizes a novel cos α technique to calculate in-plane residual stresses (σ_x and σ_y) and shear residual stress (τ_{xy}) as presented in Figure 2.5 (a). Keeping the angle of incident X-rays constant, the relative position of the D-S ring for the L-PBF parts (red ring) from that of the stress-free part distortion D-S ring (black ring) was used to calculate strain as presented in Figure 2.5 (b). The equations used to calculate the in-plane stress and shear stress from strains are presented in Equations. (2.2) - (2.5). The fundamental equations used to find the D-S ring radius and residual stress for this method are explained in detail in Refs. [77][142]. The (311) family of crystallographic planes were used to create the D-S rings and for verifying the residual stress in as-built and heat-treated samples, as the (311) planes represent bulk macro stresses and are less sensitive to intergranular strain compared to other planes. In addition, the sensitivity of peak broadening under the influence of external stress becomes higher with higher

2θ angles, thus, the use of diffraction peaks at higher 2θ angles provides a better option for conducting full width at half maximum (FWHM) analysis [143]. Cos α method is considered inefficient to capture continuous D-S rings in case of coarse grains. The irradiated area of Cos α method is limited which hampers accurate stress measurements of coarse grains. X-ray oscillation techniques are used in such cases to cover enough grains to get accurate data. For sample heat treated at 1050 °C for 1 hour, the D-S ring was obtained using 3-axes oscillation technique instead of 1-axis oscillation used in other samples. Since the diffraction from grains in sample heat treated at 1050 °C for 1-hour could not be covered using 1-axis oscillation, 3-axes oscillation was used to collect more diffraction data with low standard deviation by swinging X-ray source +/-5degree each 3-axes. To understand the effect of heat treatment on residual stress in sub-surface region of the sample, the surface was electropolished by 100 μm. Residual stress was measured using the 3-axes oscillation. Since a prominent level of tensile residual stress is generated at the top surface of the L-PBF samples due to the layer-wise AM process, the top oriented surface of each sample (surface facing upward during printing) was inspected to study the effects of heat-treatment temperature on residual stress and FWHM.

$$\varepsilon_{\alpha 1} = \frac{1}{2}\{(\varepsilon_\alpha - \varepsilon_{\pi+\alpha}) + (\varepsilon_{-\alpha} - \varepsilon_{\pi-\alpha})\} \tag{2.2}$$

$$\varepsilon_{\alpha 2} = \frac{1}{2}\{(\varepsilon_\alpha - \varepsilon_{\pi+\alpha}) - (\varepsilon_{-\alpha} - \varepsilon_{\pi-\alpha})\} \tag{2.3}$$

$$\sigma_x = -\frac{E}{1+v} \cdot \frac{1}{sin2\eta} \cdot \frac{1}{sin2\varphi_o} \cdot \left(\frac{\partial \varepsilon_{\alpha 1}}{\partial cos\alpha}\right) \tag{2.4}$$

$$\tau_{xy} = \frac{E}{2(1+v)} \cdot \frac{1}{sin2\eta} \cdot \frac{1}{sin\varphi_o} \cdot \left(\frac{\partial \varepsilon_{\alpha 2}}{\partial sin\alpha}\right) \tag{2.5}$$

where $\varepsilon_{\alpha 1}$ is the mean of the four principal strains, $\varepsilon_{\alpha 2}$ is the mean difference of the four principal strains as shown in Fig. 2.5 (b), while E and v are the Young's modulus and Poisson's ratio of IN625, respectively. Since X-ray diffraction penetration is extremely shallow (< 10 um),

the stresses in the Z-directions are assumed to be zero. In this case, a biaxial in-plane stress state condition is assumed to exist on the sample surface. The non-zero stress components on the sample surface are σ_x, σ_y, and σ_{xy}.

a)

b)
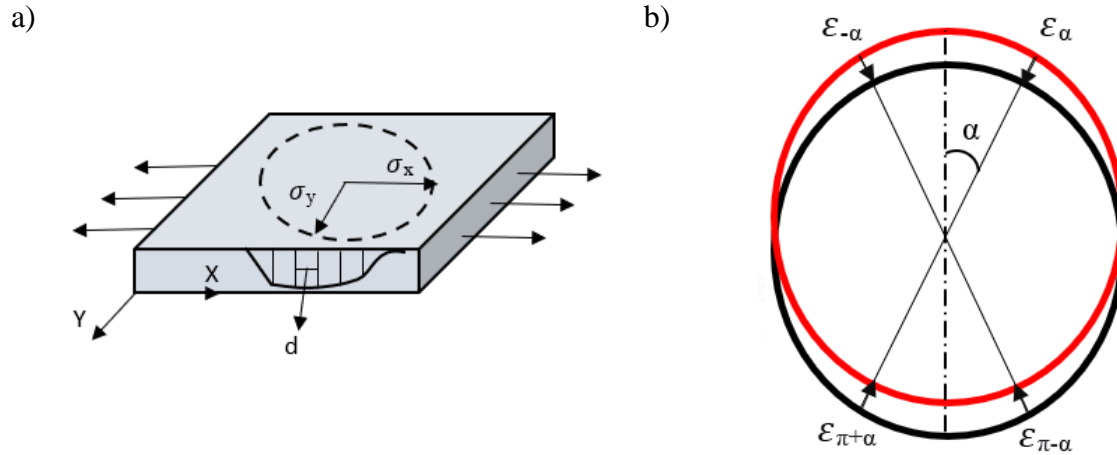
Figure 2.5. (a) Demonstration of in-plane residual stress (σ_x and σ_y) and shear residual stress (τ_{xy}) direction on a sample surface, (b) schematic of D-S ring position of L-PBF samples (red ring) and stress-free (black ring) IN625 samples with four strains (ε) shown.

The X-ray spot size was around 1 mm^2 and the sample surface size was 10 mm^2. The sample was fixed at the bottom during the residual stress measurement. Since the measurement spot is well away from the sample surface boundaries, it can be assumed the effects of sample size and boundary conditions will be negligible.

2.1.3 Principal direction and stress

Tensile or compressive residual stress in the microstructure cause strain which ultimately change the d-spacing in the lattice structure. Since X-ray diffraction penetrates is extremely shallow (< 10 um), a biaxial in-plane stress state condition is assumed to exist on the sample surface. In this study, the sample is considered to be isotropic. The X-ray spot size was around 1 mm^2 and the sample surface size was 10 mm^2. The sample was fixed at the bottom during the

residual stress measurement. Since the measurement spot is well away from the sample surface boundaries, it can be assumed the effects of sample size and boundary conditions will be negligible. The stress components used to calculate in-plane principal direction and stresses are presented in Figure 2.6 (a) and (b).
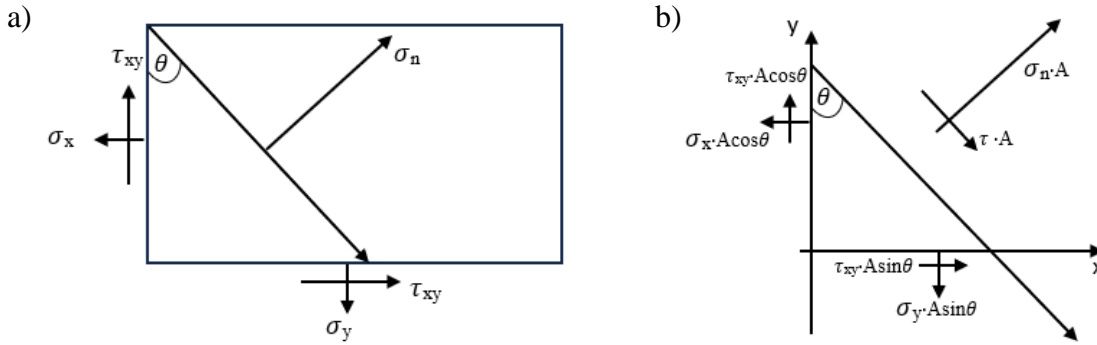
Figure 2.6. (a) Demonstration of in-plane (σ_x and σ_y) and shear (τ_{xy}) residual stress direction on a sample surface and (b) detailed illustration of these stress components used to calculate principal directions and stress.

Magnitudes of the normal have been designated by σ_n. Thus, the problem reduces to finding the unknown stresses σ_n in terms of the known stresses σ_x, σ_y, and τ_{xy}.

Assuming the summation of force in the normal direction n = 0,

$$\sigma_n{\cdot}A = (\sigma_x{\cdot}A\cos\theta)\cos\theta + (\sigma_y{\cdot}A\sin\theta)\sin\theta - (\tau_{xy}{\cdot}A\sin\theta)\cos\theta - (\tau_{xy}{\cdot}A\cos\theta)\sin\theta \quad (2.6)$$

$$\sigma_n = \sigma_x{\cdot}\cos^2\theta + \sigma_y{\cdot}\sin^2\theta - 2\,\tau_{xy}\cos\theta\sin\theta \quad (2.7)$$

$$\sigma_n = \sigma_x\left(\frac{1+\cos2\theta}{2}\right) + \sigma_y\left(\frac{1-\cos2\theta}{2}\right) - \tau_{xy}\frac{\sin2\theta}{2} \quad (2.8)$$

Rearranging the above equation, we get

$$\sigma_n = \left(\frac{\sigma_x + \sigma_y}{2}\right) + \left(\frac{\sigma_x - \sigma_y}{2}\right)\cos\theta - \tau_{xy}\sin2\theta \quad (2.9)$$

The angle (θ) at which maximum stress occurs can be found by differentiating Eq (1) and equating it 0.

$$\frac{d\sigma_n}{d\theta} = 0 \quad (2.10)$$

$$0 = -(\sigma_x - \sigma_y)\sin2\theta - 2\tau_{xy}\cos2\theta \qquad (2.11)$$

$$0 = -(\sigma_x - \sigma_y)\frac{\sin2\theta}{\cos2\theta} - 2\tau_{xy}\frac{\cos2\theta}{\cos2\theta} \qquad (2.12)$$

$$0 = -(\sigma_x - \sigma_y)\tan2\theta - 2\tau_{xy} \qquad (2.13)$$

Rearranging the above equation, we get

$$\theta = \frac{1}{2}\tan^{-1}\left(\frac{-2\tau_{xy}}{\sigma_x - \sigma_y}\right) \qquad (2.14)$$

Equation (2.14) represents the planes with maximum and minimum normal stresses separated by 180°. Assuming $\sigma_y = \frac{1}{2}\sigma_x$, the angle of principle stress is 19 degrees. Normal stresses present on these planes are called principle stresses. Principle stresses are given as:-

$$\sigma_1 = \sigma_{max} = \left(\frac{\sigma_x + \sigma_y}{2}\right) + \sqrt{\left(\frac{\sigma_x - \sigma_y}{2}\right)^2 + \tau_{xy}^2} \qquad (2.15)$$

$$\sigma_2 = \sigma_{min} = \left(\frac{\sigma_x + \sigma_y}{2}\right) - \sqrt{\left(\frac{\sigma_x - \sigma_y}{2}\right)^2 + \tau_{xy}^2} \qquad (2.16)$$

Considering the as-built vertically build IN625 sample, the σ_x and τ_{xy} measured using the Cos α method are 77 and 15 MPa respectively. Assuming $\sigma_y = \frac{1}{2}\sigma_x$,

$$\sigma_1 = \sigma_{max} = \left(\frac{\sigma_x + \sigma_y}{2}\right) + \sqrt{\left(\frac{\sigma_x - \sigma_y}{2}\right)^2 + \tau_{xy}^2} = 82 \text{ MPa}$$

$$\sigma_2 = \sigma_{min} = \left(\frac{\sigma_x + \sigma_y}{2}\right) - \sqrt{\left(\frac{\sigma_x - \sigma_y}{2}\right)^2 + \tau_{xy}^2} = 33 \text{ MPa}$$

2.1.4 Nano-hardness testing

Nano-indentations were made along the top surface of the as-built, heat-treated, and wrought samples using a Micromaterials Vantage Nanotest System. A nano-indentation mapping of 10x10 matrix was performed on each sample's top face and an average was calculated along with standard deviation. Indentations were made following the standard of ASTM E2546 and ISO 14577. The testing parameters used are listed in Table 2.2.

Table 2.2. Nano-indentation testing parameters.

Max Load (mN)	500
Loading Time (s)	10
Unloading Time (s)	10
Holding Time (s)	5
Indent Spacing in X (μm)	60
Indent Spacing in Y (μm)	60
Indentation Matrix	10x10
Indenter Type	Berkovich
Indenter Material	Diamond

2.1.5 EBSD analysis

The EBSD system Analytical FEG-SEM FEI Nova Nano SEM 230 was used to study the effects of heat treatment and build orientation on grain orientation, texture, grain size, in as-built AM, 1050-1-hour heat treated. A similar study was performed in wrought IN625 samples to provide reference data. All samples were ground and polished per standard metallography and vibratory polished for 2 hours. EBSD scans were performed on YZ sections of all samples. Kernel average misorientation (KAM) maps were captured in as-built and 1050 heat treated IN625 samples to estimate the changes in micro strain levels post heat treatment.

2.2 Results and discussions

2.2.1 Residual Stress

Residual stress magnitude and nature (tensile or compressive) determined using the cos α method along the top surface of the as-built and heat-treated L-PBF IN625 samples are shown in

Figure 2.7. As seen from Fig. 2.7, the top surface of the as-built vertically and diagonally build samples is dominated by tensile residual stress with a value of 77 ± 15 and 52 ± 12 MPa. This tensile residual stress is generated from the complex thermal gradients and rapid cooling rates (in range of 10^3 K/s to 10^6 K/s) occurring during the L-PBF process. The intense cooling related to the laser leaving the melt pool and freshly coated powder layers causes built layers under the exposed surface to shrink. The high cooling rate is increased as the measured point moves away from the substrate. Similar results were reported by Shuai *et al*. where they observed formation of intense tensile residual stress in as-built SLM IN625 samples [144]. The vertically printed sample was found to possess higher detrimental tensile residual stress on its top surface compared to the diagonally printed sample surface. Similar results were concluded from a study conducted by Pant *et al* [68]. In addition, vertically printed samples residual stress measurements had higher standard deviation compared to diagonally printed samples. This implies that the microstructure in the vertically printed sample was more anisotropic. Heat treatments performed herein reduced as-built tensile residual stress. Increasing the heat-treatment temperature reduced the tensile residual stress and increased the formation of compressive residual stress on the surface. For 700 ℃, 900 ℃, and pre and post electropolished 1050 ℃ samples, the residual stresses were measured as -64 ± 13 MPa, -96 ± 17 MPa, -394 ± 50 MPa, and 23 ± 18 MPa, respectively. Similar effects of stress relieved heat treatment on residual stress were observed in L-PBF IN718 where tensile residual stress was removed and compressive residual stress was formed on the surface [62]. Formation of high compressive stress on a surface has proven to improve the fatigue life, fatigue strength, slow crack propagation, and increase resistance to environmentally assisted cracking, such as stress corrosion cracking of the material in past studies [145]. The high standard deviation in the 1050 ℃ heat-treated sample is an indication of an increase in grain size. Since the grain size is large,

the number of grains taken into consideration under 1-axis oscillation X-ray method is less and this led to large uncertainty.
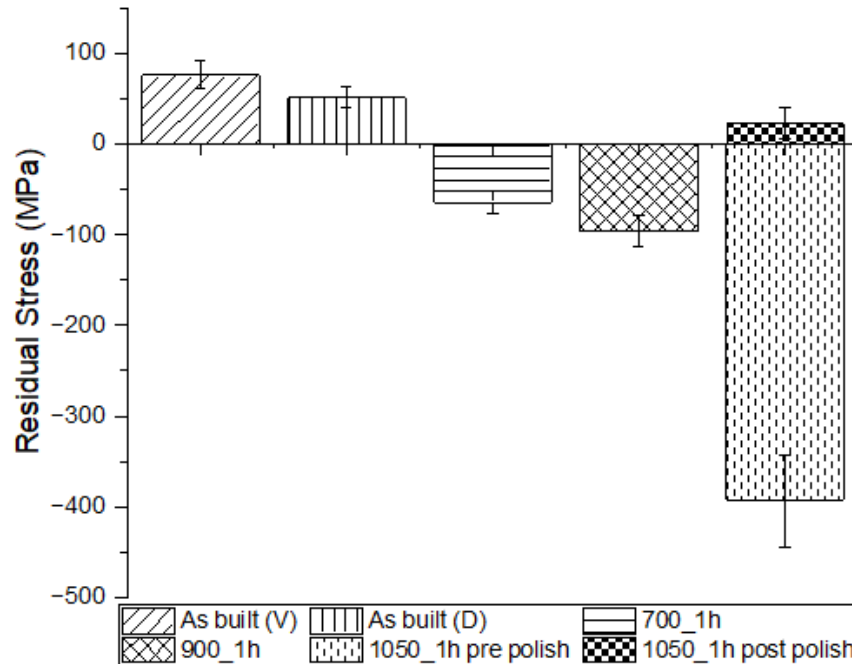
Figure 2.7. Residual stress of as-built vertically (V) printed, diagonally (D) printed, and heat-treated L-PBF IN625 samples. Positive values represent tensile and negative values represent compressive residual stress. Error bars provide the standard deviation.

The D-S ring distortion and (311) peak of the as-built vertical and diagonal oriented, 700 °C, 900 °C, and 1050 °C heat-treated samples are shown in Figure 2.8. The D-S ring, which is recorded on a two-dimensional detector, is taken by the single exposure of X-rays, and this is an important working principle of the cos α method. In Figure 2.8., the cyan ring represents the D-S ring, and the green and yellow rings indicate inner and outer FWHM, respectively. As seen in Fig. 2.8., the ring distortion from the standard D-S ring position can be used to understand the nature and value of residual stress. The grey lines in Fig 2.8 (lines appear as 'cross-hairs') indicate the position of a wrought IN625 D-S ring position. Tensile residual stress within a sample reallocates the D-S ring position below the grey lines. The presence of compressive residual stress moves the

D-S ring position above the grey lines. Residual stress magnitude has its influence on the circularity of D-S ring. The higher the stress magnitude, higher is the distortion in the ring circularity. The circularity of the D-S ring recorded in the vertically printed sample is seen to be more distorted compared to the diagonally printed indicating more micro strain present in the microstructure. 1050 °C pre polish D-S ring was observed to be most distorted with residual stress value of -394 ± 50 MPa. Post polishing, the D-S ring was observed to be less distorted since the residual stress magnitude was measured to be 23 ± 18 MPa. The intensity uncertainty of the (311) diffraction peak is maximum for the 1050 °C heat-treated sample which may be due to larger grain size. The intensity uncertainty is less for columnar grains elongated in build direction as observed in the as-built L-PBF samples. A similar level of uncertainty is observed in the residual stress results in Figure 2.7. indicated by the longer error bars.
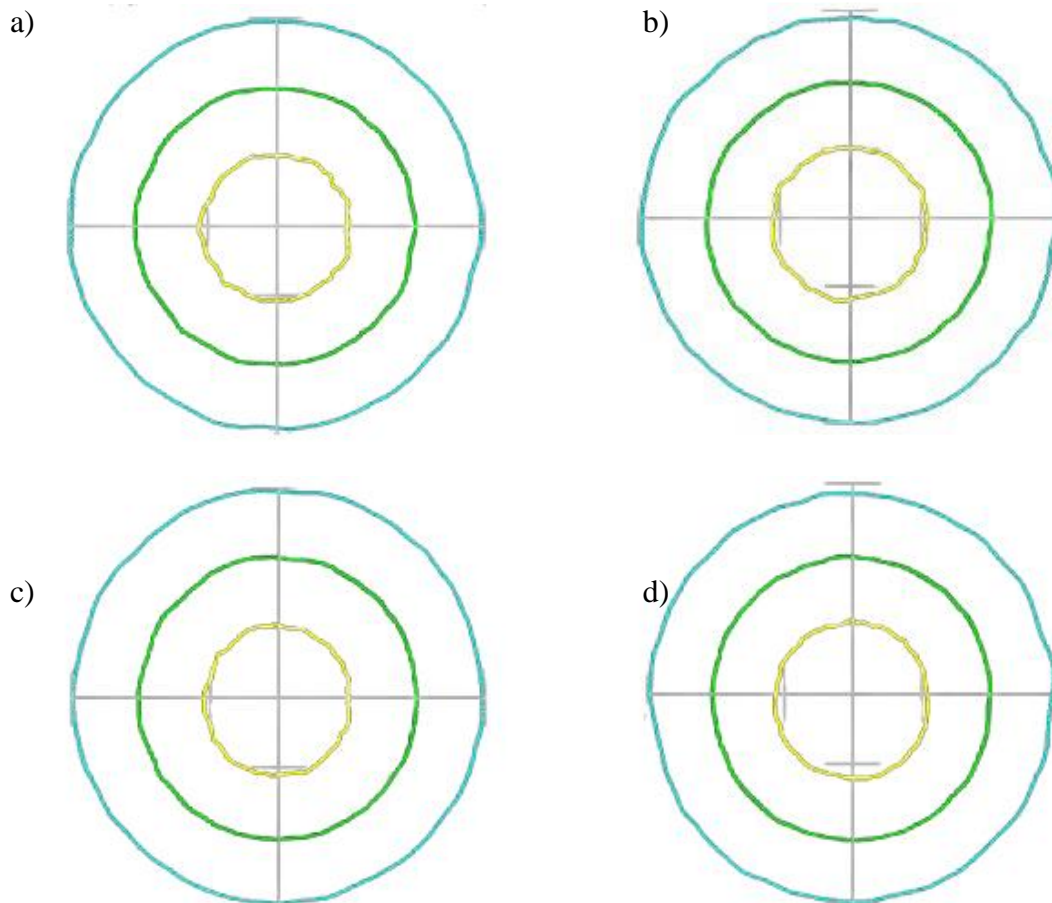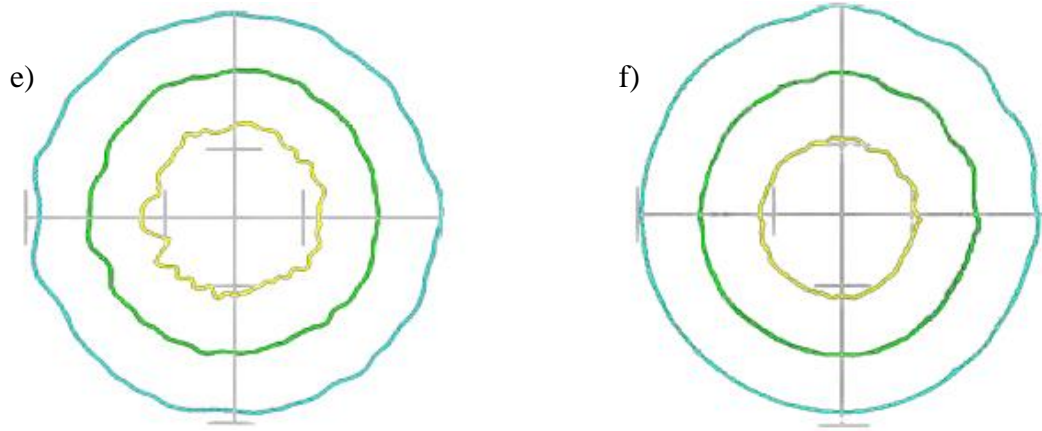
Figure 2.8. Debye-Scherrer ring distortion of (a) as-built vertical, (b) as-built diagonal, c) 700 ℃

d) 900 ℃, e) pre polish 1050 ℃, and f) post polish 1050 ℃ L-PBF IN625 samples. Cyan ring

represents the D-S ring, and green and yellow rings indicate inner and outer FWHM,

respectively.

The FWHM of the (311) diffraction peak for as-built vertical and diagonal oriented, 700

℃, 900 ℃, pre polish 1050 ℃, and post polish 1050 ℃ samples were quantified as 2.98 ± 0.11,

3.01 (+0.14/-0.1), 2.78 (+0.09/-0.14), 2.84 ± 0.09, 3.99 (+0.56/-0.42), 2.12 ± 0.10 degrees,

respectively is shown in Fig. 2.9. The reduction of the FWHM of the diffraction peak from the as-

built condition to 700 ℃ provides an indication of micro strain relaxation in grains. In 900 ℃ heat-

treated sample, the FWHM increases slightly implying the possible formation of metastable δ

precipitate in finer quantity. Precipitates are one source for forming strains [146]. After 1050 ℃

heat treatment, high compressive stress on surface and twinning phase causes peak broadening of

diffraction from (311) plane. After the surface was electropolished by 100 μm, the high

compressive stress on surface was removed and more uniform residual stress sub-surface was

exposed. The FWHM on this sub-surface was least as seen in Fig. 2.9 (f), the peak is sharpest,

indicating that the heat treatment effect was more prominent on external surface compared to

interior sub-surface. In addition, the formation of precipitates due to heat-treatment on external surfaces could be more prominent compared on sub-surfaces.
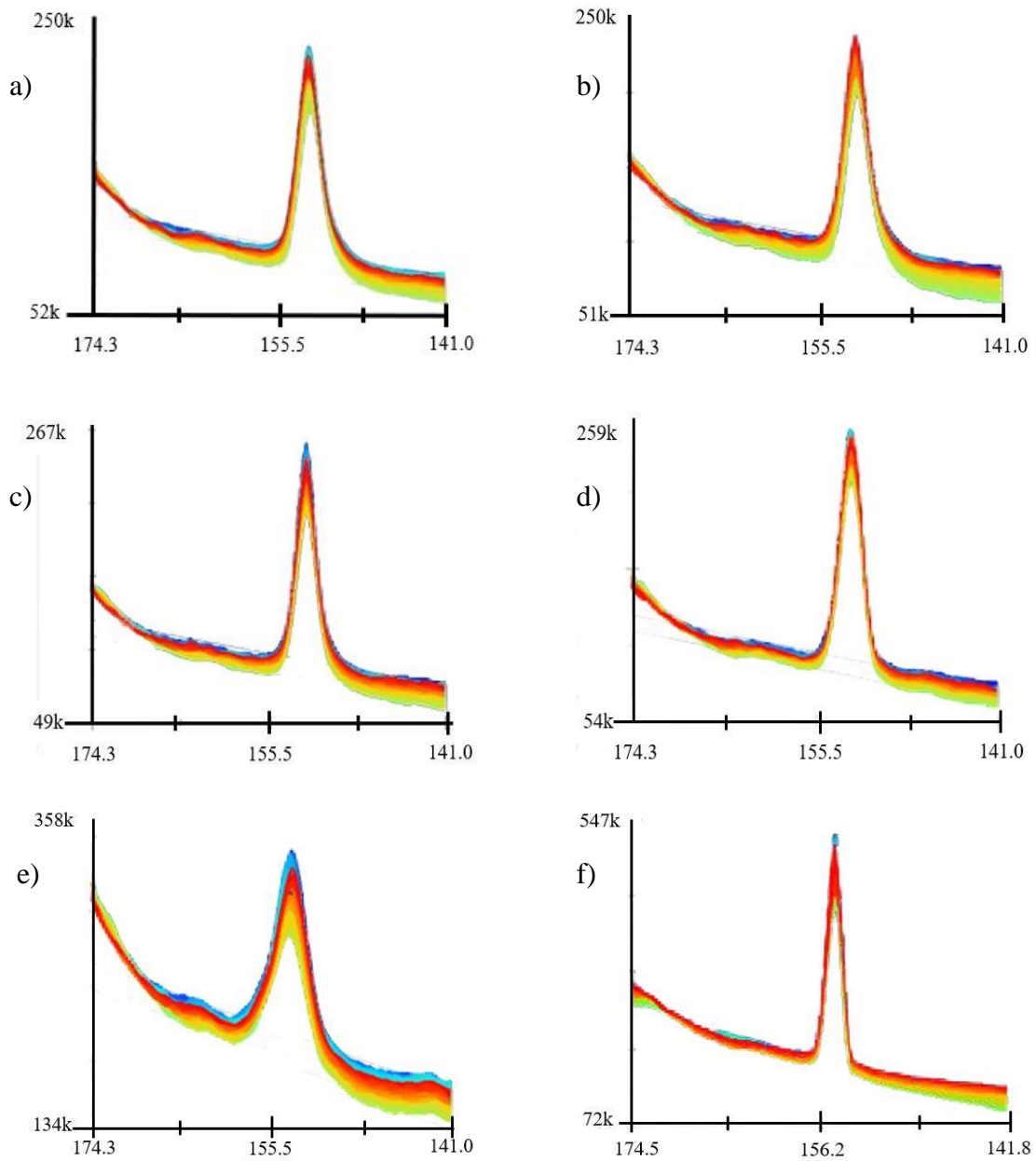
Figure 2.9. (311) diffraction peak for a) as-built vertical, b) as-built diagonal, c) 700 ℃, d) 900 ℃, e) pre polish 1050 ℃, and f) post polish 1050 ℃ L-PBF IN625 samples. X-axes represent 2θ and y-axes represent peak intensity.

2.2.2 Microstructural evolution after heat treatment

The trend in residual stress results is better understood by performing EBSD to study the microstructure evolution. The microstructural evolution from the as-built condition to the condition corresponding to 1-hour heat-treated at 1050 °C, was analyzed by performing EBSD. EBSD analysis helps to reveal the crystallography and morphology of grains. Similar analysis was conducted to understand the microstructure difference between vertically and diagonally printed samples. The EBSD results of L-PBF samples were compared with a wrought sample. Fig. 2.10. shows the inverse pole figure (IPF) maps of the YZ cross-sections for the as-built vertical, as-built diagonal, 1050 °C, and wrought samples. As seen in Fig. 2.10 (a), as-built sample exhibit texture, with grains oriented in Z- direction. The grains are elongated in Z-direction or build direction, which is inherited from the L-PBF process. The grains were found to be oriented parallel to the <001>. A series of columnar grains growing through several layers of powder oriented parallel to the build direction was seen in Fig. 2.10 (a). This is the consequence of directional heat transfer taking place during the solidification stage of fabricating. The high cooling rate supplied by the build substrate to every new melted powder layer helps to adhere with previously melted layer to form elongated grains. This observation is in line with the literatures, where elongated grains along the build direction was reported in L-PBF as-built parts [147]. The grains in diagonally printed sample as seen in Fig. 2.10 (b) were observed to arrange themselves at some angle with respect to build direction. The texture quality in both oriented samples were observed to be similar with minimal variations.
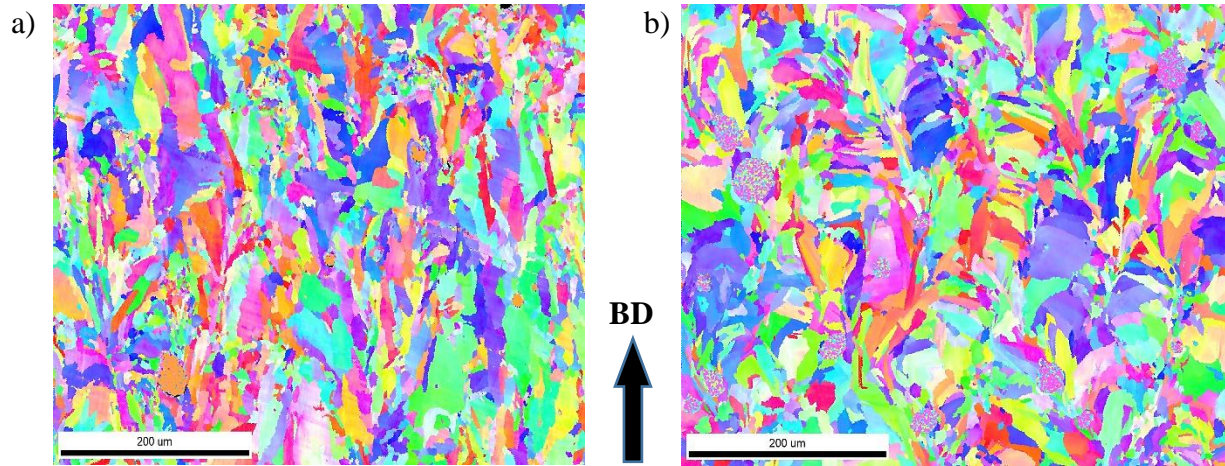
Figure 2.10. Microstructural texture in a) as-built vertical, b) as-built diagonal IN625 samples.

BD stands for build direction.

After heat treating at 1050 °C for 1-hour, the columnar grains observed in the as-built sample start to disintegrate, and grains oriented themselves in random angles as seen in Fig. 2.11 (a). The grain size can be seen to increase as well compared to the ones formed in as-built sample. The recrystallization process can be seen to start with the elimination of the fine dendritic and columnar grains. In addition, the annealing twins start to appear in the microstructure. This twinning highlighted in Fig. 2.11 (b) supports the partial relaxation of high tensile residual stress trapped in the as-built L-PBF sample, due to high thermal gradient during the building process as seen in Fig. 2.7. However, the 1050 °C-1-hour heat treatment seems to be not sufficient to obtain a complete homogenous microstructure like the one observed in the reference wrought IN625 sample presented in Fig. 2.11 (c). Following the 1050 °C-1-hour heat treatment, homogenization of microstructure took place and approached the one observed in wrought sample. The wrought sample exhibits fine, equiaxed grains oriented in random angles as seen in Fig. 2.11 (c).

49
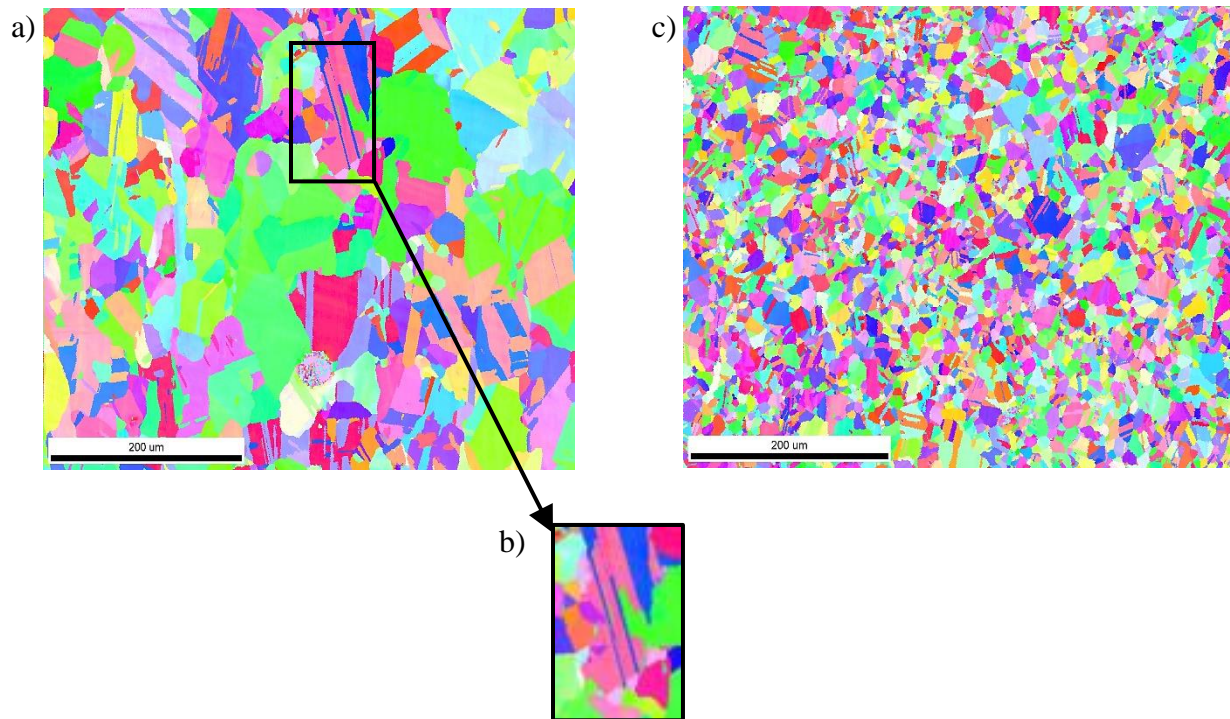
Figure 2.11. a) 1050 °C-1-hour heat treated vertical, b) Twinning phenomenon is zoomed in a box, and c) wrought IN625 samples. BD stands for build direction.

The grain size distribution (area fraction) is presented in Figure 2.12. As presented in Figures 2.12 (a) and (b), the grain size distribution in vertically and diagonally printed samples was observed to be similar. The grain size ranged between 15-30 μm had maximum area fraction. This can confirm the minimal difference in grain morphology in vertically and diagonally printed samples.
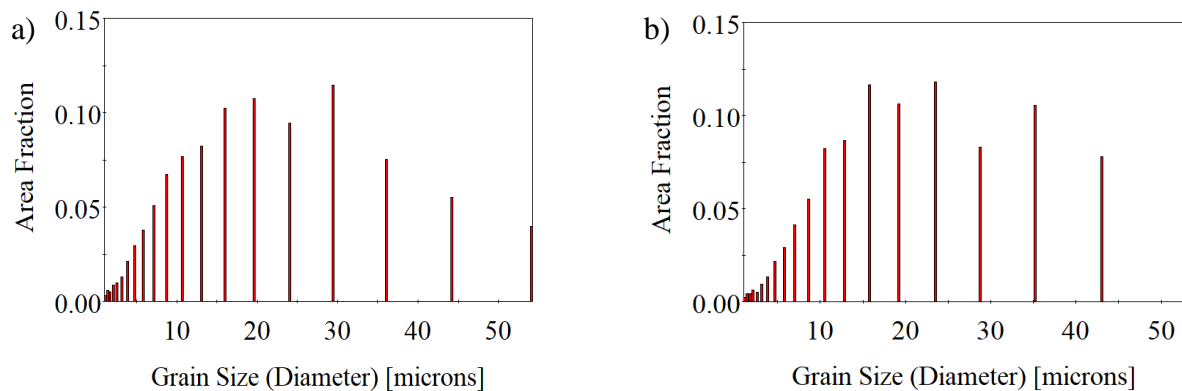
Figure 2.12. Grain size distribution (in area fraction) for a) as-built vertical, b) as-built diagonal.

Heat treating the as-built vertical oriented sample at 1050 ℃ for 1-hour, resulted in recrystallization of grains. The grain size increased where grain sizes ranging between 35-65 μm occupied the maximum area fraction as showed in Figure 2.13 (a). Figure 2.13 (b) shows grain size distribution in wrought IN625 sample. Since post processing procedure is different for conventional machined sample, the grain morphology is mostly equiaxed and grain size ranging between 5-15 μm had maximum area fraction.
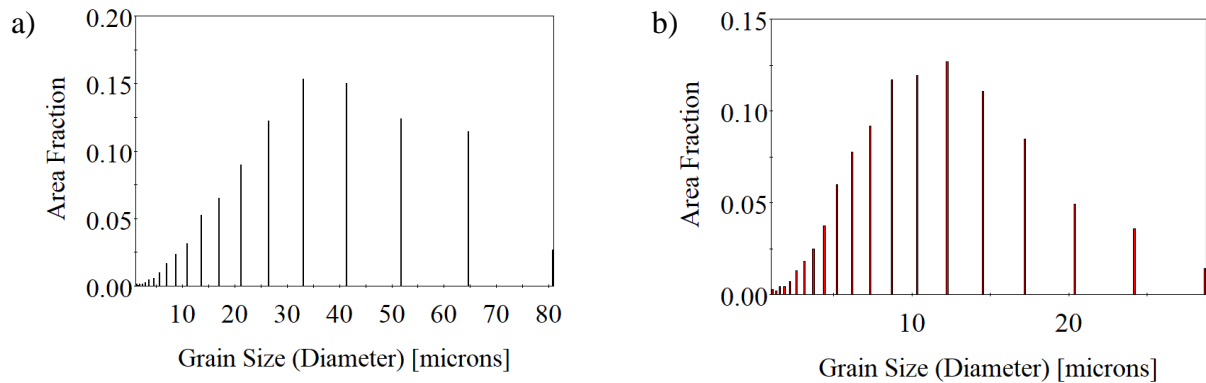
Figure 2.13. Grain size distribution (in area fraction) for a) 1050 ℃-1-hour vertical, and d) wrought IN625 samples.

Kernel average misorientation (KAM) maps shown in Figures 2.14 (a) and (b) for as-built vertical and as-built diagonal IN625 samples, respectively. IN625 samples were used to further analyze the correlation between micro strain caused by geometrically necessary dislocations in the microstructure. KAM plotted as a map discloses regions with an increased density of the defects, and as an average value for the whole scan, may indicate material strain history. Average KAM values and its modifications under different material conditions are commonly used to measure plastic strain. Regions with high KAM values commonly represent regions with plastic strain [148]. The scales enclosed in each KAM map indicate the level of misorientations. The scales are very low in value which helps address the misorientations caused by dislocations in grains. The micro strain present in the microstructure is highlighted by the green regions. As seen in Figure

2.14 (a), the micro strain in the as-built vertically printed sample is dense indicating presence of high residual stress. The micro strain is associated with the presence of high dislocation density which is inbred during the L-PBF process. Dislocations in diagonally built sample were less dense compared to vertically built IN625 sample in Figure 2.14 (b). This confirms the lower residual stress caused by local strain in diagonally printed sample observed in Figure 2.7. The blue circular spots in as-built samples KAM maps indicate presence of pores which were inherited during the L-PBF build process.
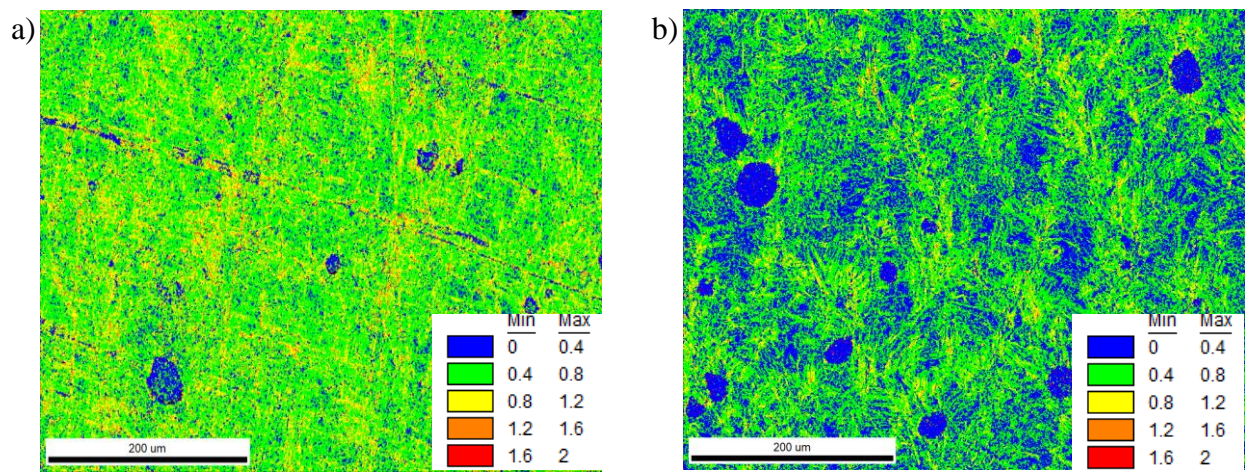
Figure 2.14. KAM maps for a) as-built vertical and b) as-built diagonal IN625 samples showing minor misorientations caused by dislocations highlighted in green regions.

Post 1050 °C-1-hour heat treatment, the dislocations reduced significantly as seen in Figure 2.15 (a) with the reduction in the green regions. This indicates the initialization of microstructure recrystallization process. The reduction in dislocations evidently relaxes the high residual stress observed in the as-built vertically built sample. Heat-treatment at high temperature dissolves the dislocations formed on the grain boundaries and the microstructure is cleaned. The micro strain in 1050 °C-1-hour heat treated sample can be seen to be lower than that measured in the reference wrought IN625 sample as seen in Figure 2.15 (b).
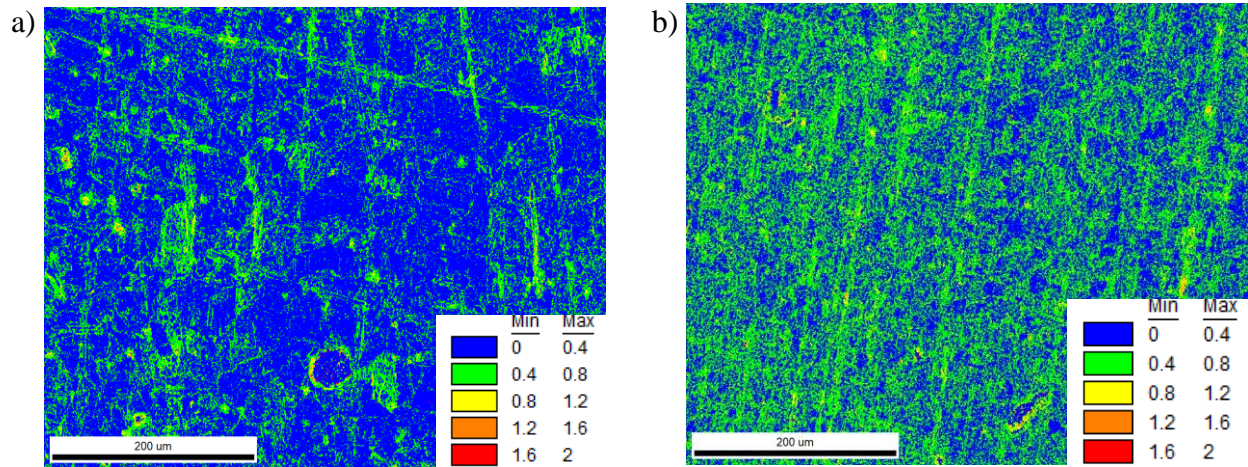
Figure 2.15. KAM maps for a) 1050 °C-1-hour heat treated and d) wrought IN625 samples showing minor misorientations caused by dislocations highlighted in green regions.

2.2.3 Nano-hardness

Misorientations caused by formation of dislocations in microstructure increase the hardness. The hardness indenter motion below the external surface and in the sample is resisted by the dislocations present in the microstructure. The higher the dislocation, higher will be the force required to reach the desired depth by the indenter. As a result, the as-built vertically printed sample measured highest nano-hardness with an average value of 3.7 GPa over the depth of 500 μm depth as seen in Figure. 2.16 (a). In addition, it can be observed that as-built vertically printed sample measurements inherited larger standard deviations and fluctuation between two measurements indicating anisotropic microstructure. The anisotropic microstructure here indicates the presence of micro strain caused by dense dislocation density as seen in Figure. 2.16 (a) which leads to anisotropic trend in nano hardness values. Similarly, in as-built diagonally printed sample measured an average nano hardness of 3.7 GPa over the depth of 500 μm depth as seen in Figure. 2.16 (b). However, the presence of dislocation density is less compared to vertically printed

53

sample, the nano hardness values from the surface to 500 μm depth has lower standard deviations in nano hardness values as seen in Figure. 2.16 (b).
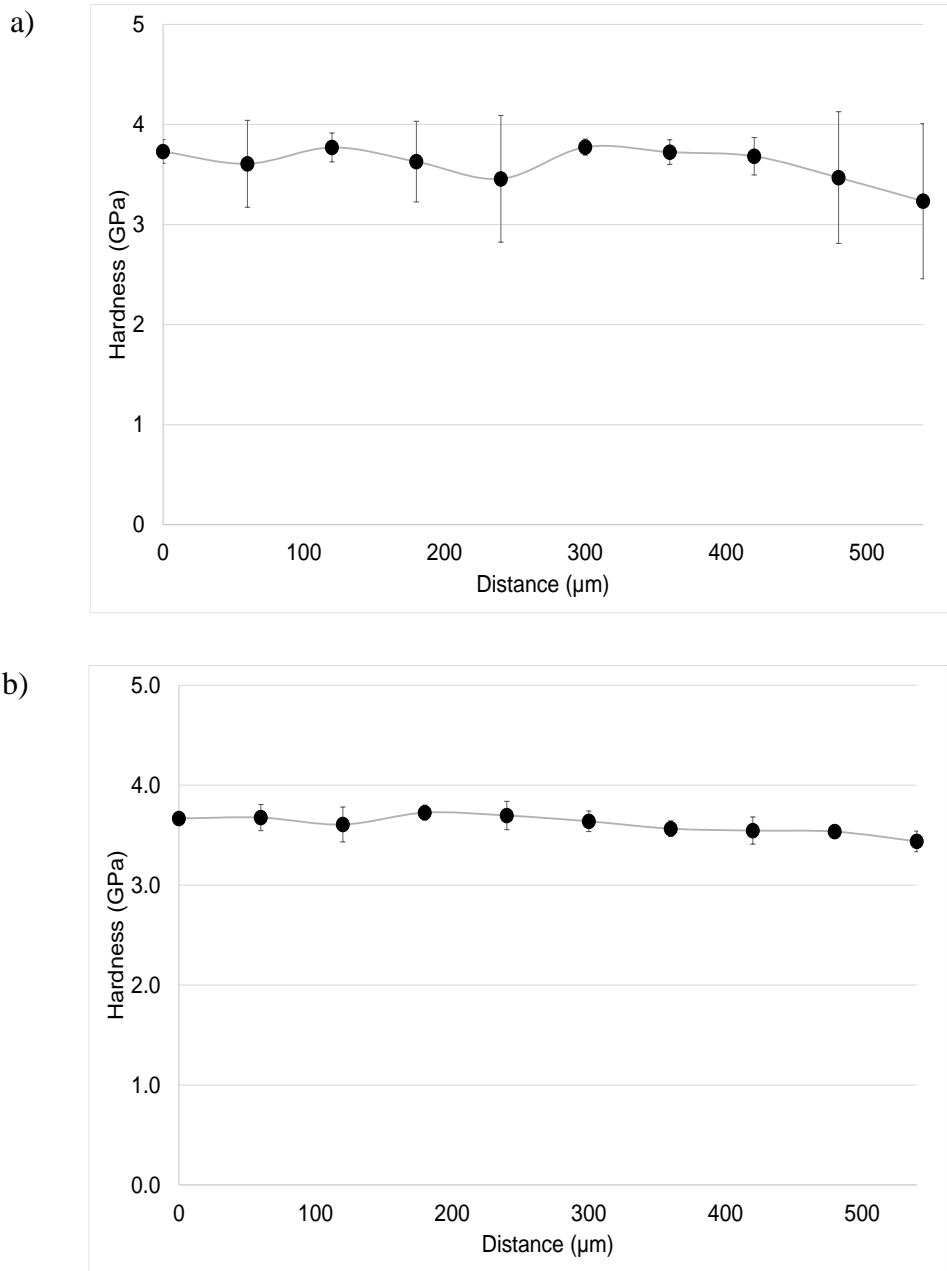
Figure 2.16. Nano-hardness measurements on the top surface of a) as-built vertical and b) as-built diagonal IN625 samples. Vertical lines on each measurement indicate error bars.

1050 °C-1-hour heat treatment introduced homogeneity in microstructure by reducing the dislocation density and residual stress, which ultimately reduced the nano-hardness as seen Figure. 2.17 (a). The hardness of 1050 °C-1-hour heat treated sample was reduced to an average value of 2.98 GPa. Even the standard deviation of each measurement and fluctuations in value between two spatial measurements were reduced significantly. Since the dislocation density which restricts the motion of plastic strain introduced during hardness test is reduced in 1050 °C-1-hour sample, the force required by indenter to reach desired depth is reduced. The average nano-hardness measured in 1050 °C-1-hour sample was lower than the conventional wrought IN625 sample which measured an average value of 3.25 GPa as shown in Figure. 2.17 (b). Both 1050 °C-1-hour and wrought measurements showed lower standard deviation indicating homogeneity in microstructure and mechanical property.

a)
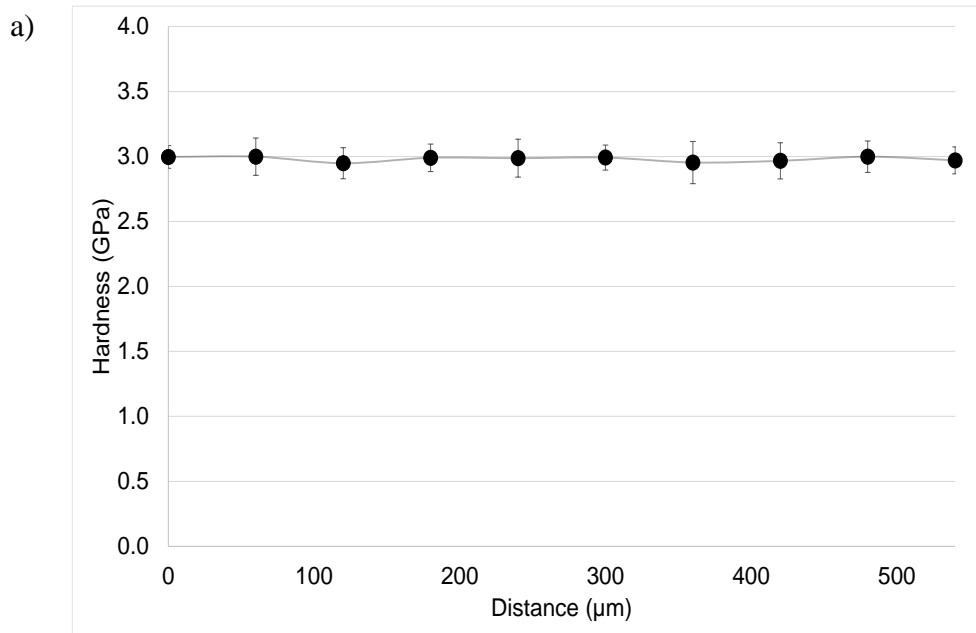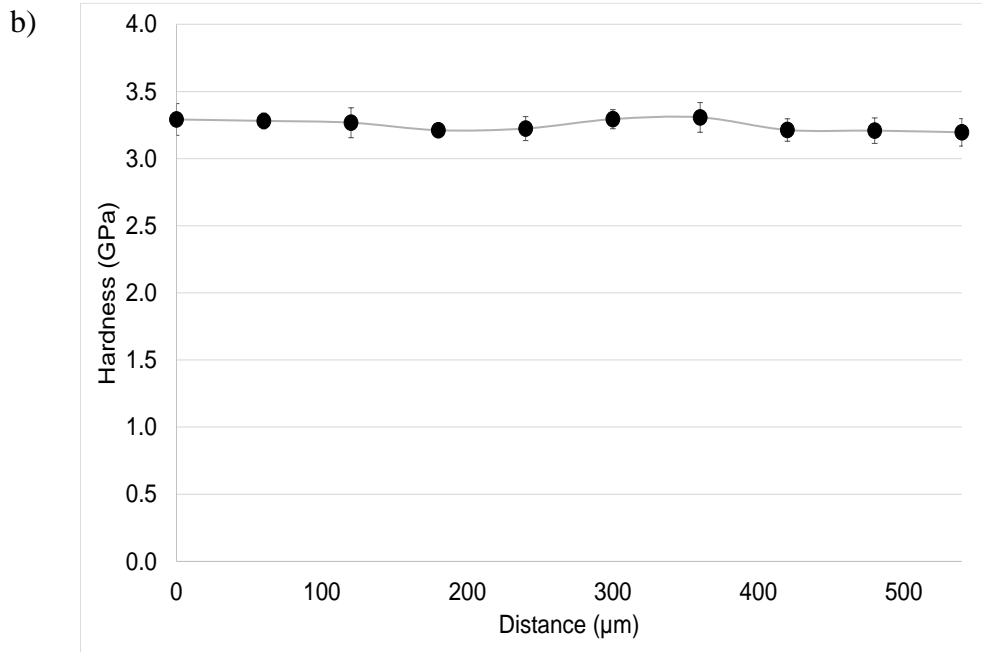
Figure 2.17. Nano-hardness measurements on the top surface of a) 1050 ℃-1-hour vertical and

b) wrought IN625 samples. Vertical lines on each measurement indicate error bars.

2.3 Concluding remarks

In this chapter, a novel method of XRD was employed to measure RS in L-PBF IN625 samples. The effects of different L-PBF AM build orientations (vertical & diagonal) and heat-treatment temperatures on the level of RS magnitude were studied. To completely understand the effects of RS, a thorough EBSD and mechanical test (nano-indentation) was performed. The EBSD and nano-indentation results helped to correlate with the magnitude of RS in the samples. This chapter also provided strategies to mitigate the formation of detrimental surface RS in the IN625 sample. Some of the valuable observations from this chapter are summarized below:

1. The complex thermal gradient incurred during the L-PBF process introduced detrimental tensile RS in the as-built vertical and diagonal oriented sample.

2. The unfavorable tensile RS was mitigated by using the post-processing heat-treatment method. The heat-treated samples were observed to possess advantageous compressive RS.

56

3. EBSD results indicated the presence of strong texture in the as-built samples with grains oriented along the build direction.

4. Heat-treated at 1050 ℃ for 1-hour, changed the fine microstructure in the as-built sample to coarse microstructure and introduced twinning indicating recrystallization process.

5. KAM maps indicate presence of higher dislocation quantity in the as-built vertical sample compared to the as-built diagonal IN625 sample which results in higher tensile RS in the as-built vertical sample.

6. Nano-indentation results showed the as-built samples had higher hardness value compared to the 1050 ℃ for 1-hour heat-treated and wrought samples. This is due to the higher dislocations in the as-built samples observed in the KAM maps.

Chapter 3 - Full-Spectrum Neutron Irradiation Effects

This chapter focuses on investigating the full-spectrum (thermal neutrons) nuclear irradiation effect, which is more representative of real-life nuclear environments, on L-PBF, L-PBF/heat-treated, and wrought IN625. The effects of two build orientations (vertical and diagonal) and different heat treatment temperatures in L-PBF IN625 are also explored while considering their porosity distributions. Irradiation-induced hardening or embrittlement was measured using Vickers microhardness on all samples, before and after irradiation. Comparing the hardening performance of L-PBF and wrought IN625 samples under neutron irradiation provides a better understanding of how different manufacturing techniques affect the structural integrity of this nickel-based superalloy of interest under a harsh radiation environment.

3.1 Experimental methods

3.1.1 Porosity measurement

To interpret the influence of microstructure defects such as porosity level on post irradiation results, porosity mapping was performed on selected pre-irradiated L-PBF samples. Porosity measurements were performed via 3D X-ray computed tomography (XCT) scanning to compile digital X-rays of each sample into a 3D volume which provides a map of the porosity distribution in each sample. Porosity in a 3D XCT scan is identified as a low-density area (i.e., void space / air bubble) surrounded by higher density material. Raw XCT scan data for the part was reviewed and the region of interest to be analyzed was established and adjusted parameters which are used to define the pores. This parameter tuning phase increases the accuracy of both identification and quantification of each pore. A wealth of pore attribute data is calculated for each pore and includes pore count, size, and sphericity. Porosity map for all samples measured using a NSI X5000 225 XCT system available at Delphi Precision Imaging Corporation (Redmond, WA

USA). Samples were mounted on a rotating stage and imaged using 255 kV and 160 μA with 0.25 mm of copper (Cu) filter for beam hardening. A total of 5600 projections were taken using an oversampled sub-pixel scan technique with five integrated frames yielding a voxel size of 15 μm. 3D XCT reconstruction was done with NSI EFX software. Analysis / Visualization was performed using the commercial software VGSTUDIO MAX 2022 (Volume Graphic, Heidelberg, Germany). Pores with probability (P) > 1 were considered in this analysis. 'Probability,' in the context of the software, quantifies the certainty in a detected pore being a real pore and not any surface imperfection, inclusion, or artifact. To help understand the effect of build orientation (during L-PBF) and heat treatment, the porosity distributions in the as-built and 1050 ℃-1-hour heat-treated vertically- and diagonally printed L-PBF samples were measured and analyzed.

3.1.2 Full spectrum irradiation

IN625 samples were wrapped in aluminum foil for stability and positioned inside a 2.54 cm diameter vessel. As shown in Figure 3.1, the vessel was then suspended inside the beryllium reflector of the 10 MW reactor at the University of Missouri Research Reactor (MURR) for 310 hours. All samples experienced a total flux of 6.61 x 10^{13} neutrons/cm²/s corresponding to a fluence of 7.37 x 10^{19} neutrons/cm². Out of the total fluence experienced by the samples, 90% consisted of thermal neutrons and 10% of fast neutrons. The thermal neutrons were produced by using a moderator (water) to slow down the fast neutrons. For safety, all microhardness measurements on radioactive samples were performed inside a hot cell equipped with manipulator arms. Hardness measurements were taken approximately 180 days after removal of the irradiated specimens.
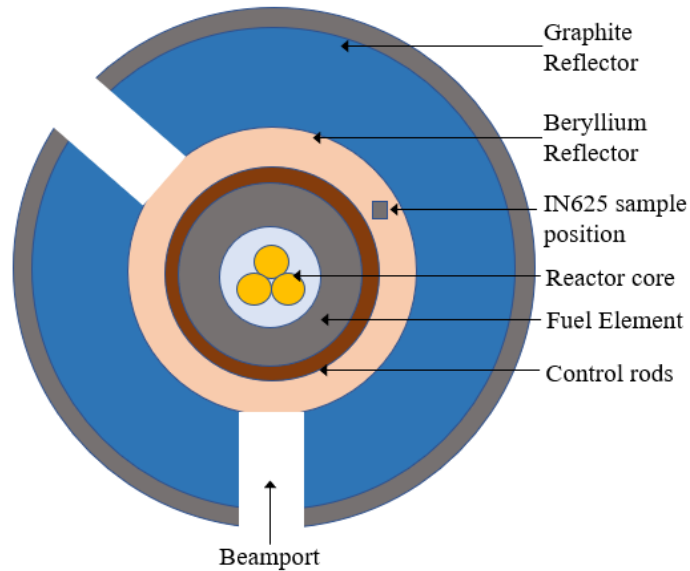
Figure 3.1. Cross section view of MURR showing position of IN625 samples.

3.1.3 Vickers microhardness testing

The extent of radiation-induced hardening in the samples was evaluated using a Vickers microhardness testing method. This specific microhardness measurement scale is good for inspecting the surface and sub-surface layers of the material. Microhardness indentations were performed using a Phase II 900-391D microhardness tester as shown in Figure 3.2. This system is automatic with the ability to perform measurements using the eyepiece (hardware) and the camera using the software equipped in the system. For each sample, five microhardness measurements were taken on the sample surface before and after full spectrum neutron irradiation. A total of five indentations were made on each sample using a 1 kgf (9.8 N) load applied with a dwell time of 15 secs. The distance between each indentation was approximately 3-4 times the indentation diagonal length. Five measurements were performed on each sample to get a reliable average and standard deviation values.
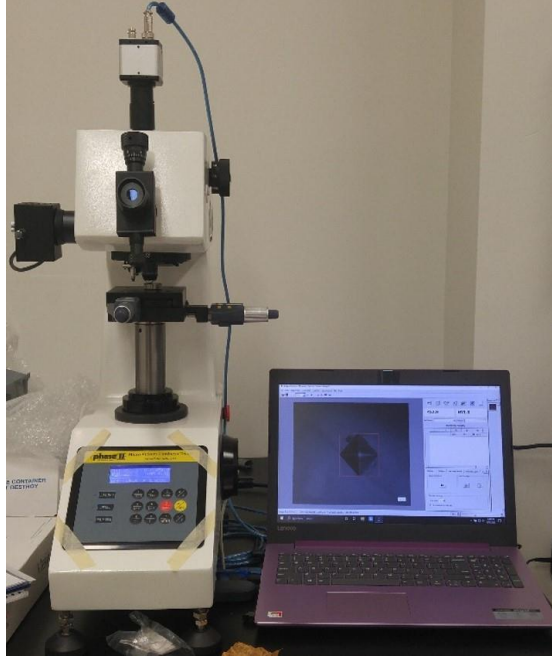
Figure 3.2. Phase II 900-391D Vickers microhardness tester system.

After performing five indentations on each sample, the diagonal length of the square indentation mark was measured. This diagonal length was used to calculate microhardness value. An average of five microhardness values was calculated. The standard deviation (σ) value for each sample was calculated using the equation (3.1).

$$\sigma = \sqrt{\frac{1}{N}\sum_{i=1}^{N}(x_i - \bar{x})^2} \tag{3.1}$$

where, N is the total number of microhardness measurements for each sample, x_i is individual microhardness value, $\bar{x}$ is the average of five microhardness values for the selected sample. The σ value is presented as an error bar in the graphs showed in the results section. The (σ) value gives an indication of the anisotropic behavior in the mechanical property of the sample under different conditions.

3.1.4 Estimation of yield strength

Hardness values can be used to estimate the yield strength of the sample using the following formulation-

$$\text{Mean pressure under the indenter } (P_m) = \frac{\text{Applied load (F)}}{\text{Projected area (A)}} \tag{3.2}$$

Mean pressure is related to the flow stress $\sigma_f = \dfrac{P_m}{C}$ where C is constraint factor [149].

$$\text{Pm acting on surface is also expressed as } P_m = 2\tau_c \, (1+\theta) \, [150] \tag{3.3}$$

where, τ_c is critical maximum shear stress and θ is half angle of the tip of indenter.

$$\text{Using the Von-Mises yield criterion } 2\tau_c = 1.15 \, \sigma_{ys} \tag{3.4}$$

$$\text{And for Vickers indenter, } \theta = \frac{\pi}{2} \text{ approximately.} \tag{3.5}$$

Substituting equations (3.4) and (3.5) in (3.3)

$$P_m = 2.95\sigma_{ys} \tag{3.6}$$

$$\text{HV can be related to Pm as HV} = 0.927 \, P_m \tag{3.7}$$

Combining equations (3.6) and (3.7), we get the following equation to get an approximate σ_{ys} value-

$$\sigma_{ys} \cong \frac{HV}{3} \tag{3.8}$$

Peak stress in the sample occurs where the indenter tip contacts the surface. The tip after the indentation create the largest displacement in the -Z direction. The shape for different indenters are different. For example, Vickers indenter is a pyramidal in shape which create a square impression on the sample surface. The peak stress (σ_p) occurs at the tip of the indenter as the contact area is smallest.

$$\sigma_p = \frac{\text{Force applied (gf or kgf)}}{A}$$

3.1.5 Residual stress vs indentation

An example of a finite element analysis (FEA) was performed to simulate the effects of surface and sub-surface residual stress on indentation depth. A static structural method was used in Ansys 2023 R2. A spherical ball indenter of diameter 1 mm was used to indent on the sample surface. A displacement control method was used where the indenter was allowed to move in the sample by 0.6 mm in the -Y direction. The spherical indenter is made of IN625 whereas the sample material was assigned as structural steel since the indenter should be harder than the target surface. The geometry and dimensions of the sample and the indenter is shown in Figure 3.3. All dimensions are in mm. The indenter was placed at the center of the surface.
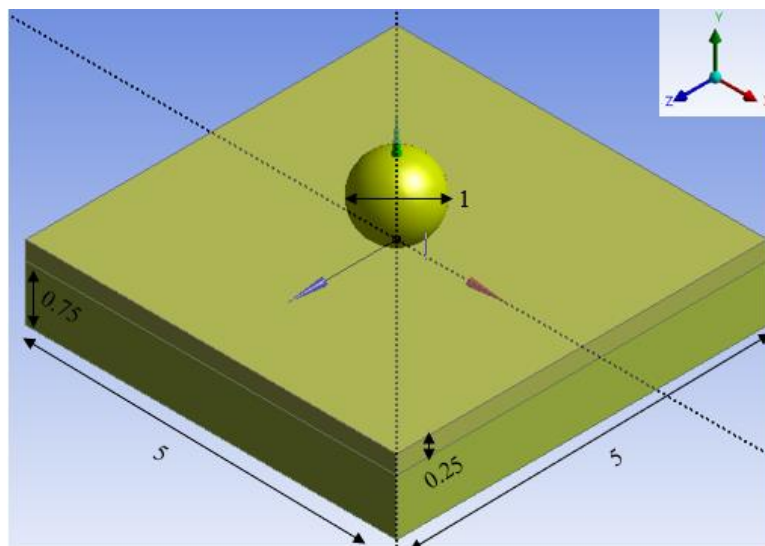
Figure 3.3. Schematic of sample and spherical indenter used for simulation.

A bonded connection was assigned between the indenter and the sample top surface as shown in Figure 3.4. The indenter was assigned as a contact body and the sample surface as target body. The indenter was set to be completely rigid to eliminate any deformation to it. The sample was sliced at 0.25 mm in -Y direction to represent the surface and sub-surface region to apply stress.
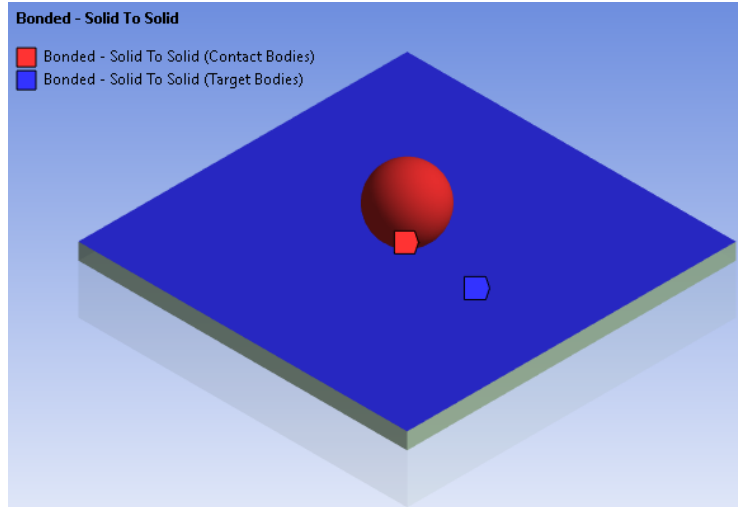
Figure 3.4. Illustration of the bonded regions.

A program-controlled mesh was applied to the sample and the indenter. A total of 14948 elements and 2720 nodes were generated over the entire model. The final mesh is shown in Figure 3.5. The indenter and bottom part of the sample was meshed using a default element size of 0.5 mm. A body sizing of 0.15 mm was applied in the sliced body to increase the accuracy of the results. The bottom face of the sample was fixed to restrict its motion during the interaction with the indenter.
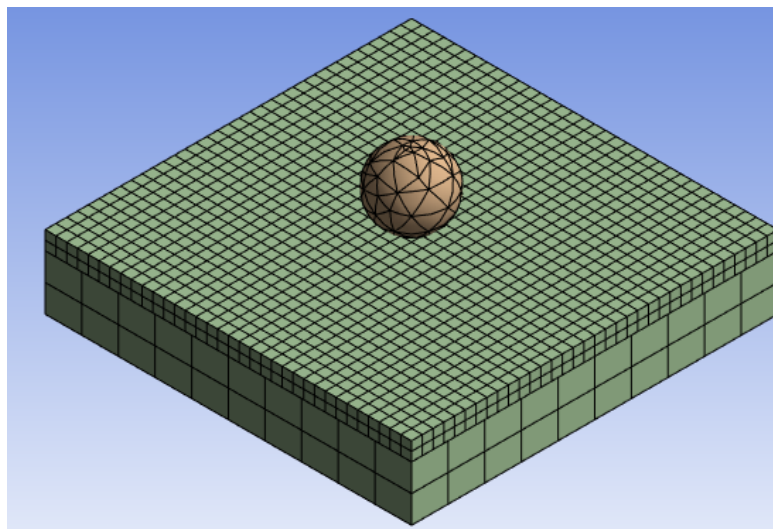
Figure 3.5. Illustration of the meshed regions.

A displacement control model was used on the spherical indenter. It was allowed to displace by -0.6 mm in the Y direction and penetrate the sample surface. Two different cases i.e., tensile stress and compressive stress were applied on the sliced body. A force of 100 N was applied on each opposite face in X-direction as shown in Figure 3.6 (a) and (b). A force value of 100 N acting on the cross-sectional area of 1.25 mm^2 creates a total stress of 80 MPa. The presence of tensile or compressive stress will influence the deformation caused by the spherical indenter on the sample in X and Y direction.
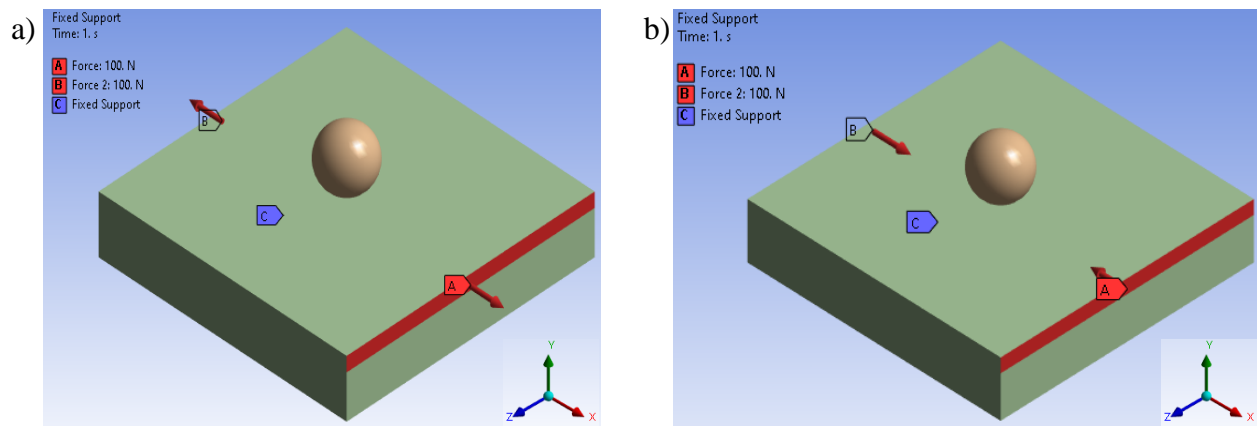
Figure 3.6. Illustration of a) tensile stress and b) compressive stress applied on the sliced body.

3.2 Results and discussion

3.2.1 Porosity measurement

Figure 3.7 shows the total porosity count in all samples. The total porosity count in as-built vertical (V), diagonal (D), heat treated vertical, and diagonal samples are 186, 367, 1117, 1389, respectively. The as-built vertically printed sample has a lower porosity count compared to diagonally printed sample. This may be due to the presence of different heat transfer paths involving conduction between adjacent powder layers and Marangoni convention. The difference in the thermal conductivity between layers oriented in vertical and diagonal directions also has influenced different porosity levels in the samples. 3D porosity maps of vertically and diagonally

printed as-built and 1050 ℃ -1-hour heat treated IN625 samples are presented in Figures 3.8 and 3.9 As seen in Figures 3.8 and 3.9, there is a considerable influence of build orientation and heat treatment on the porosity counts in the AM IN625 samples.
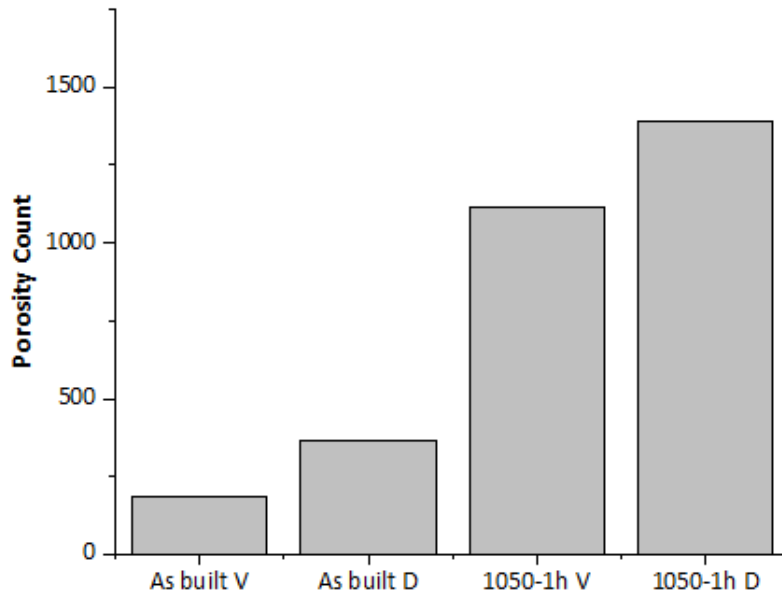
Figure 3.7. Porosity count in as-built vertical (V), as-built diagonal (D), 1050 ℃- 1-hour heat treated vertical printed, and 1050 ℃- 1-hour heat treated diagonal printed IN625 samples.
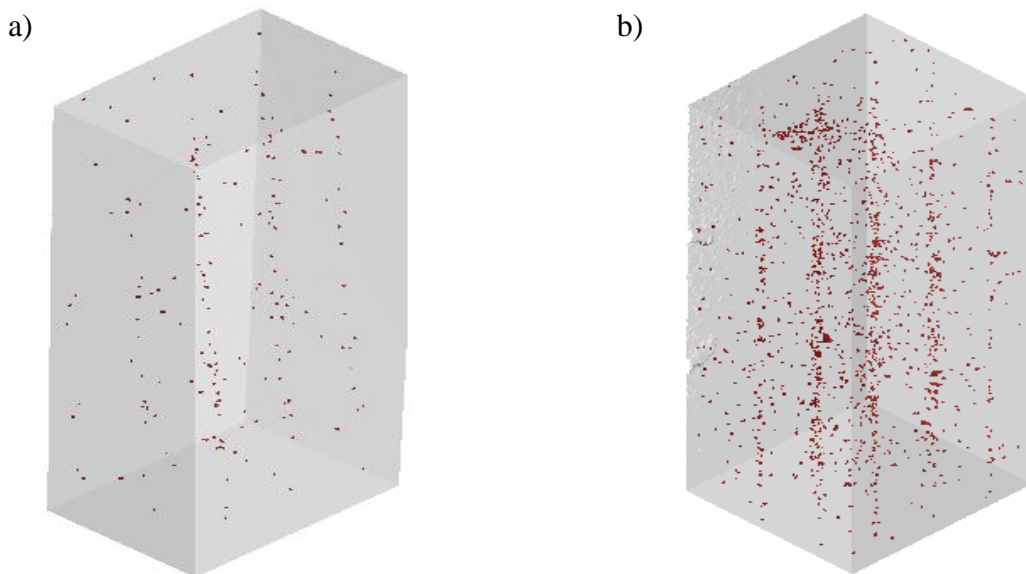
Figure 3.8. Porosity maps of a) as-built vertical and b) 1050 ℃- 1-hour heat treated vertical printed AM IN625 samples. Red points represent pores.
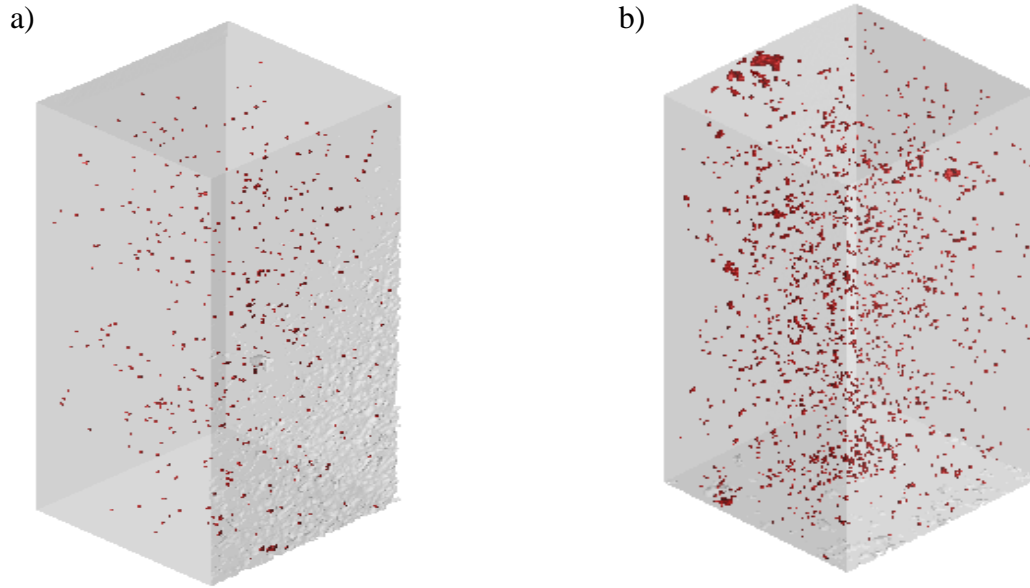
Figure 3.9. Porosity maps of a) as-built diagonal and b) 1050 ℃- 1-hour heat treated diagonal printed AM IN625 samples. Red points represent pores.

Pore diameter distribution found within as-built and 1050 ℃ - 1-hour heat treated vertically printed samples is presented in Figures 3.10 (a) and (b) respectively. Post 1050 ℃ - 1-hour heat treatment, the pore diameters in the vertically printed samples were observed to increase. The average pore diameter for the as-built and 1050 ℃ - 1-hour heat treated vertical samples are 60.226 ± 10 and 67.35 ± 10.2 μm, respectively. The formation of pores and the increased pore diameter due to heat treatment presumably resulted from the temperature-driven equilibrium diffusion and increase gas (argon) pressure inside of the pores. Similar observations of porosity growth were reported in previous studies [38], [151]–[153].

a)

mu	60.226
sigma	10.064

b)

mu	67.35
sigma	10.20
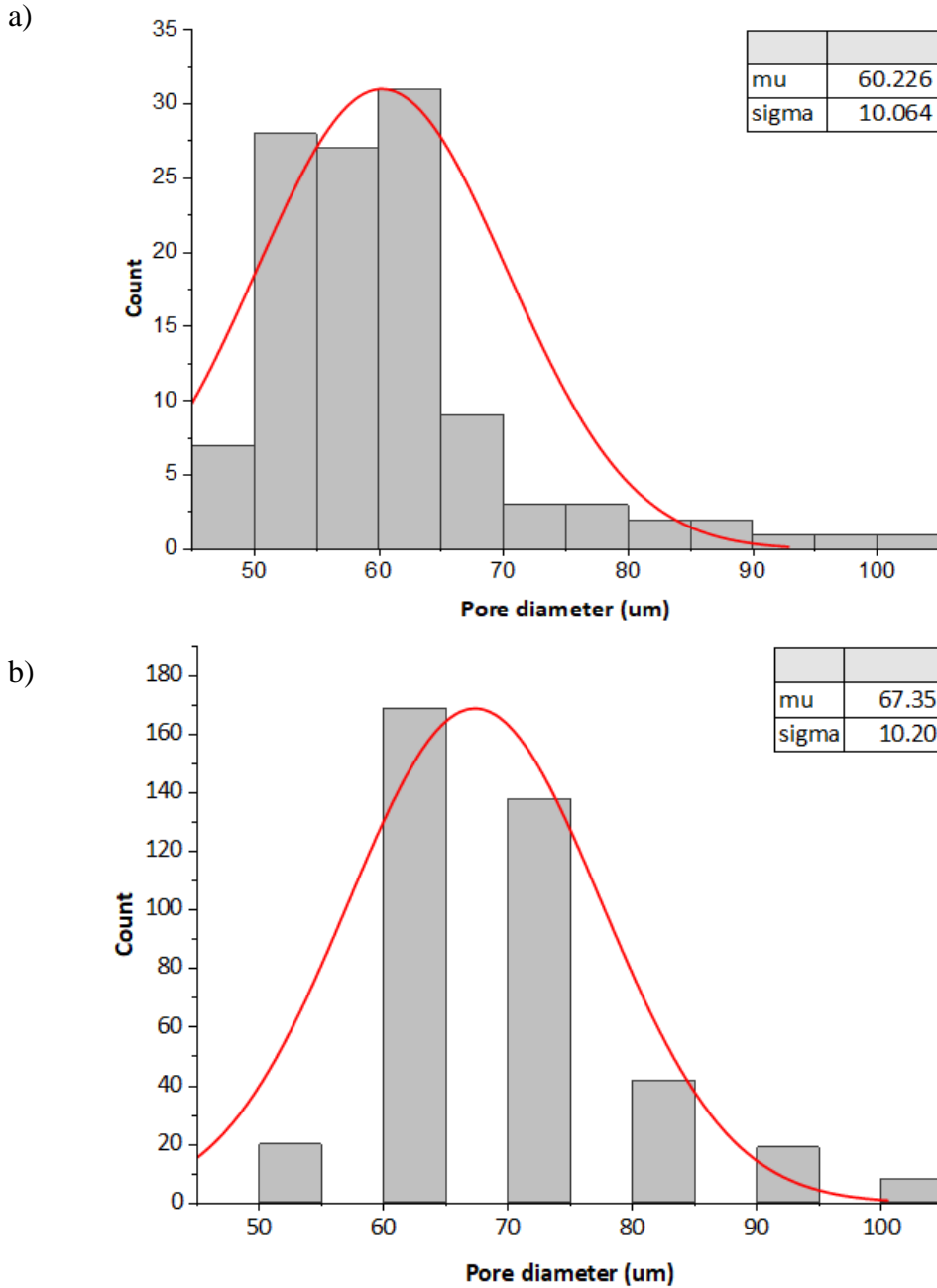
Figure 3.10. Pore diameter distribution (in μm) in a) as-built vertical and b) 1050 ℃- 1-hour heat treated vertical printed AM IN625 samples. Average and standard deviation are represented with mu and sigma values, respectively.

Pore diameter distribution found within as-built and 1050 ℃ - 1-hour heat treated diagonally printed sample is presented in Figure 3.11. A similar trend compared to vertically printed samples was observed in the diagonally printed samples. The average pore diameter for

the as-built and 1050 ℃ - 1-hour heat treated diagonal samples are 59 $\pm$ 8.13 and 68.48 $\pm$ 10.59 μm, respectively. This indicates regardless of build orientation, heat treatment resulted in the expansion of the pores. In addition, it can be observed that pore diameter distribution in the as-built vertically and diagonally samples showed very slight variation in the average pore diameter value, indicating minimal effect of the build orientation on the average pore diameter. This is indicated by the similarity in the mu values shown in Figures 3.11 (a) and 3.8 (a).
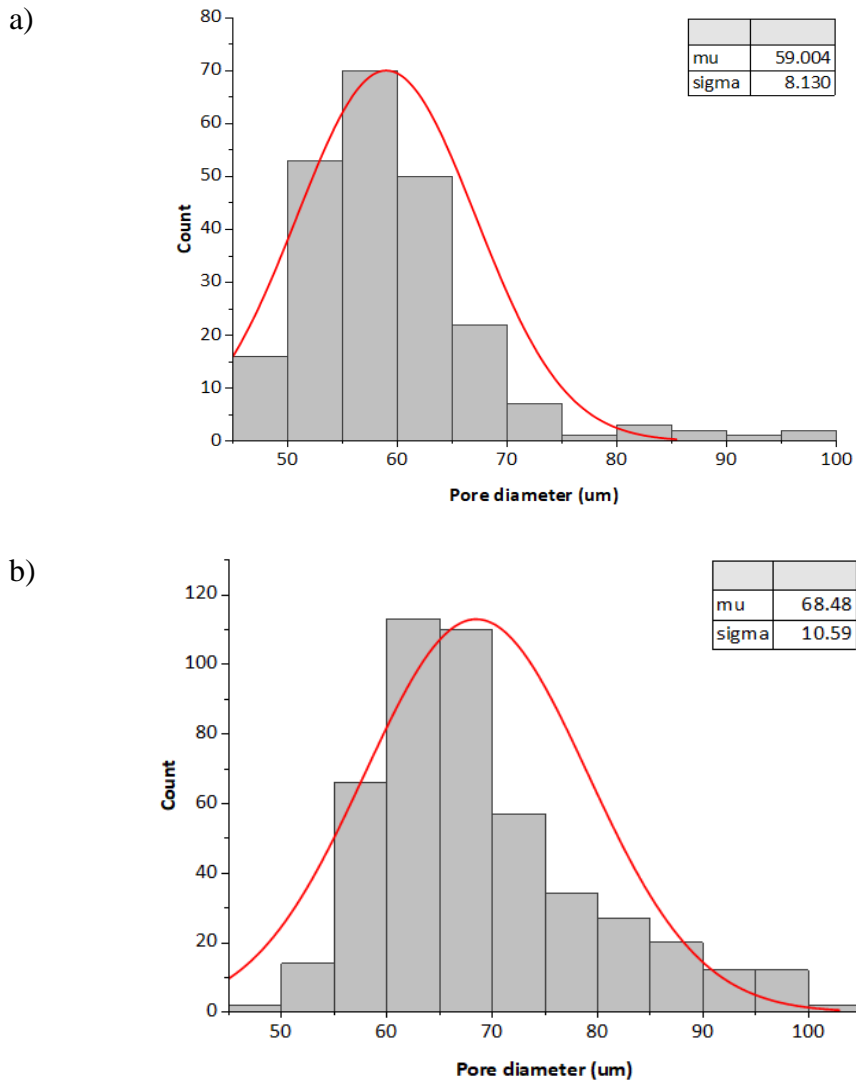
Figure 3.11. Pore diameter distribution (in μm) in a) as-built diagonal and b) 1050 ℃- 1-hour heat treated diagonal printed AM IN625 samples. Average and standard deviation are represented with mu and sigma values, respectively.

Pore sphericity within the as-built and 1050 ℃ - 1-hour heat treated vertically printed samples is presented in Figure 3.12. As presented in Figure. 3.12, the effect of heat treatment on the sphericity of the pores is not noticeable at all. The average pore sphericity in the as-built and 1050 ℃ - 1-hour heat treated vertically built samples are 0.94 ± 0.2.
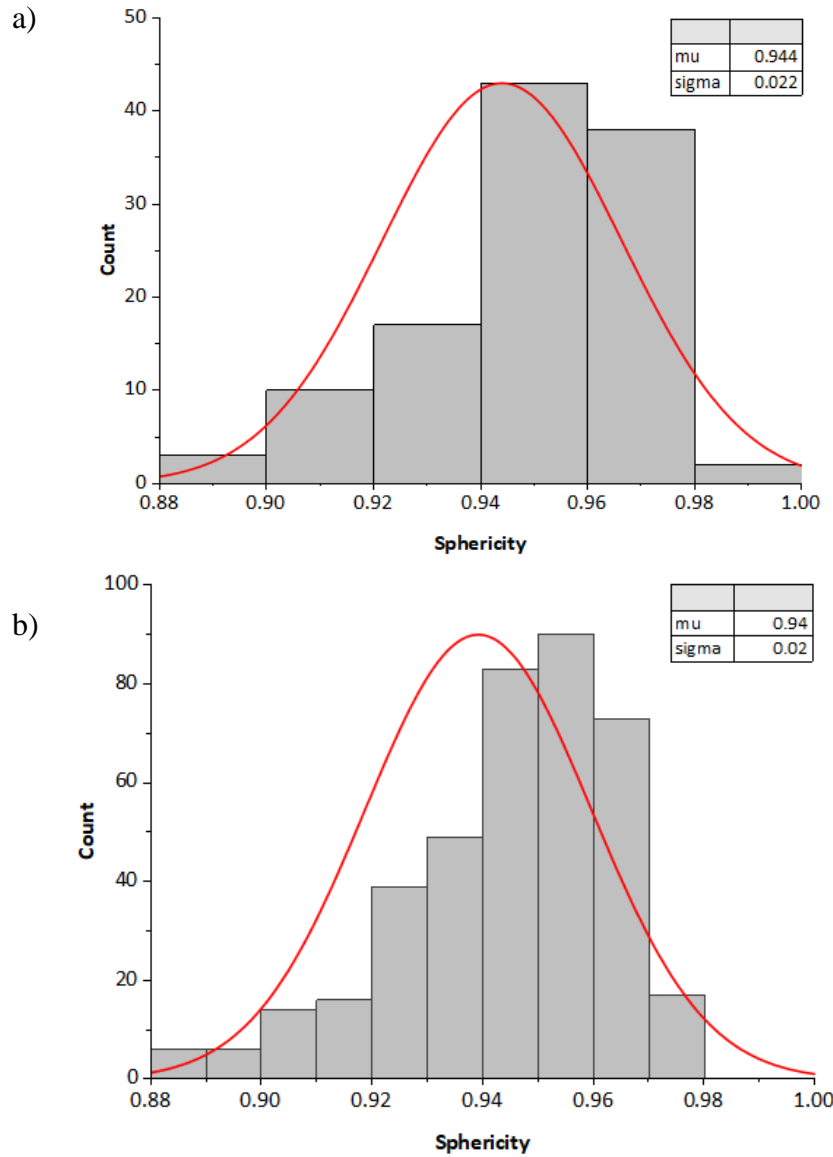
Figure 3.12. Pore sphericity distribution in a) as-built vertical and b) 1050 ℃- 1-hour heat treated vertical printed AM IN625 samples. Average and standard deviation are represented with mu and sigma values, respectively.

Pore sphericity within the as-built and 1050 ℃- 1-hour heat treated diagonally printed samples is presented in Figure 3.13. Similar observation was made in diagonally built samples compared to the vertically built samples. The average pore sphericity in the as-built and 1050 ℃-1-hour heat treated diagonally built samples are 0.94 ± 0.2. In addition, from Figures. 3.12 and 3.13 it can be observed that the difference in the build orientation has a negligible effect on the average pore sphericity value. The mu and sigma values in Figures 3.12 and 3.13 represent average and standard deviation values. The red curve represents the distribution curve of the data.

a)

b)
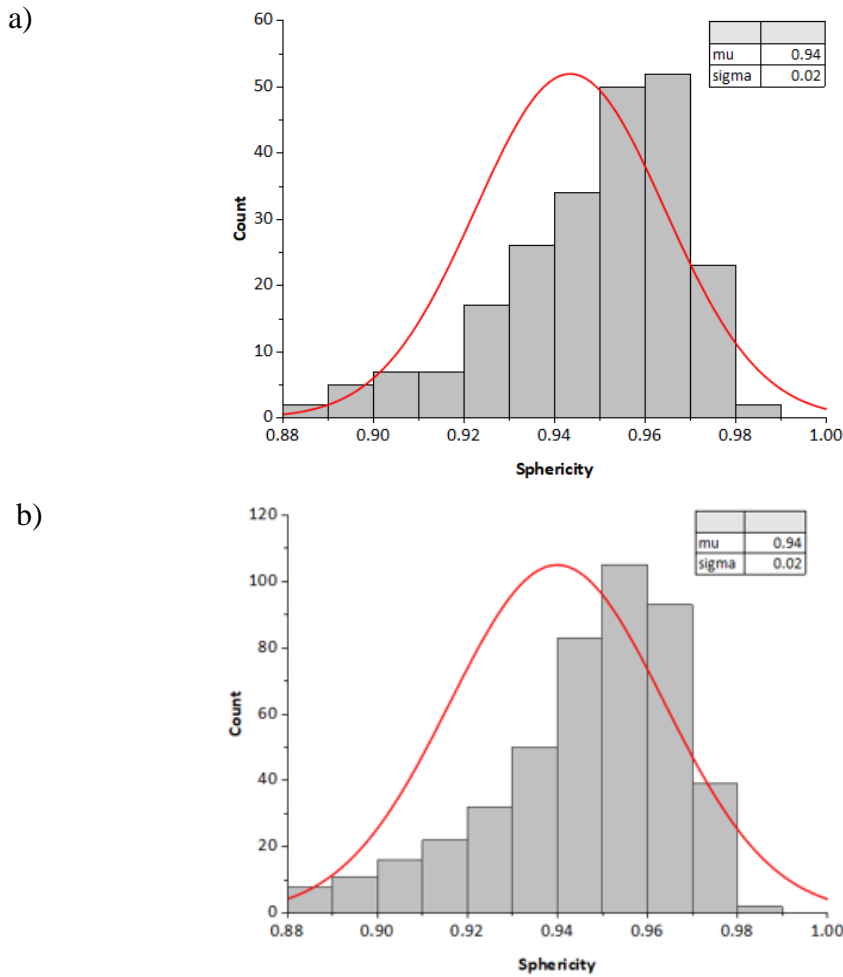
Figure 3.13. Pore sphericity distribution in a) as-built diagonal and b) 1050 ℃- 1-hour heat treated diagonal printed AM IN625 samples. Average and standard deviation are represented with mu and sigma values, respectively.

3.2.2 Vickers microhardness

The Vickers microhardness values of the pre-irradiated, as-built, heat-treated L-PBF (built in vertical and diagonal directions) and wrought IN625 samples are shown in Figure 3.14. As-built vertical and diagonal samples were measured to be 364 ± 1.2 HV and 359.2 ± 2.6 HV, respectively. This weak dependence of microhardness on build orientation was also reported in the past in Inconel 718 (IN718) fabricated using selective laser melting technology (SLM) [154], [155]. This indicates that the sub-surface porosity, which is dependent on build orientation, has little effect on the surface hardness. On the other hand, when comparing the microhardness between L-PBF and wrought samples, the wrought sample was found to be softer. The as-received wrought IN625 sample was found to have an average microhardness value of 243.8 ± 1.1 HV. This substantial difference in microhardness between L-PBF and wrought IN625 samples can be attributed to the presence of finer dendritic microstructures and high dislocation densities within L-PBF as-built samples. These microstructural features derive from high thermal gradients and cooling rates ($\sim 10^6$ °C/s) inflicted by the fast-moving, high-heat-flux laser during the L-PBF process. These high cooling and solidification rates result in alloy's heavy atoms, i.e., Mo and Nb, becoming trapped along interdendritic boundaries. The presence of these refractory metals along sub dendritic boundaries restricts the sliding of dislocations under external stress (hardness load), which ultimately increases the hardness of the material. The lower hardness of the as-received wrought IN625 is potentially due to it possessing a more homogenous microstructure with coarser equiaxed grains due to fabrication of this sample using conventional machining method with different heat treatment schedule. In addition, there may be less segregation of heavy atoms, like Nb, along the grain boundaries since the amount of Nb in the AMS5599 standard wrought samples was less than that of the L-PBF IN625 powder. The higher standard deviation in microhardness for the L-PBF

samples may be due to them possessing a less homogeneous and highly textured microstructure and higher micro segregation of heavy atoms, like Nb and Mo, in the microstructure.

Figure 3.14 also shows the microhardness measurements of heat-treated vertical and diagonal L-PBF IN625 samples. As presented in Figure 3.14, increasing the heat treatment temperature resulted in the reduction of sample microhardness regardless of its build orientation. The slight decrease in microhardness from the as-built state to 700 ℃ for the V and D built L-PBF IN625 samples is potentially due to relaxation of micro strains and other residual stresses. Further heat treating at 900 ℃ for 1-hour, the samples experienced reduction in hardness indicating potential dissolution of γ'' precipitate back in the Ni-Cr grains. Heat treating the L-PBF vertical and diagonal samples at 1050 ℃ for 1-hour brought their hardness values closer to that of the as-received wrought IN625 which follows AMS5599 standard. The significant fall of microhardness after 1050 ℃ - 1-hour heat treatment is primarily due to the increase in the porosity count and size. Under the microhardness load, the pores completely collapse and there is less restriction. Other factors contributing to this observation can be due to the decline in dislocation densities, solid state transformations, and grain recrystallization or grain coarsening. Similar microhardness trend was observed in past studies [89], [92].
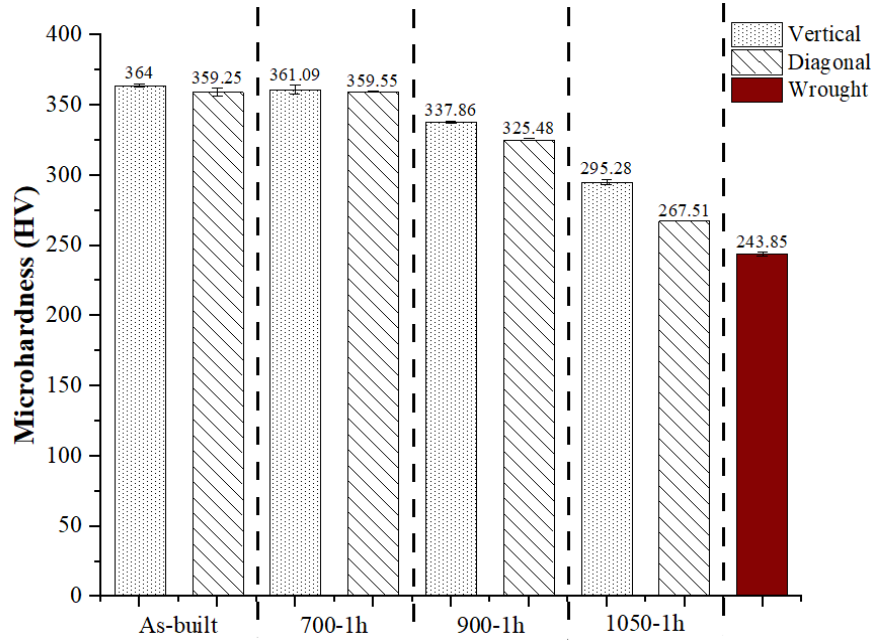
Figure 3.14. Pre-irradiation microhardness measurements of the as-built and heat-treated L-PBF vertical and diagonal, and the wrought IN625 samples. Error bars represent standard deviation in measurements.

The microhardness values of L-PBF and wrought IN625 samples after full spectrum neutron irradiation are presented in Figure 3.15. It can be observed that irradiation-induced hardening occurred in all L-PBF and wrought IN625 samples. Irradiation-induced hardening was more prominent in the as-built diagonal L-PBF sample compared to the as-built vertical sample. The as-built diagonal L-PBF sample microhardness increased ~8% compared to only 1.2% in the as-built vertical L-PBF samples as presented in Figures 3.15 (a) and (b). The diagonal specimen layer-to-layer porosity and texture are slightly different than that of the vertical specimens due to how they were oriented and manufactured (i.e., layer-wise scan strategy) during L-PBF and this clearly impacted its more pronounced hardening. From Figure 3.15 (b), it is observed that all vertically printed L-PBF IN625 samples possessed better resistance to irradiation-induced hardening compared to all wrought IN625 samples. Even after the 1050 °C heat treatment softened

the as-built vertical and diagonal L-PBF samples, making their pre-irradiation hardness comparable to those of the wrought, the L-PBF samples were observed to be resilient toward irradiation-induced hardening. This observation can be attributed to one of the irradiation-induced defects categorized into four types: point defects (e.g., interstitials and vacancies), one-dimension (e.g., dislocation), two-dimension (e.g., dislocation stack), three-dimension (e.g., voids, pores, precipitates) [156]. Vertically and diagonally built, 1050 °C heat-treated samples hardened by 1.32% and 3.82% respectively, as compared to the as-received wrought which hardened by 5.25%. Finally, from the Figures 3.15 (a) and (b), it can be observed that neutron irradiation-induced significant radiation hardening effects in relatively softer pre-irradiated material (i.e., the wrought IN625) than in the harder pre-irradiated material (except the as-built diagonal sample). This result agrees with some previously reported observations where the initial softer materials hardened more after irradiation [157], [158].
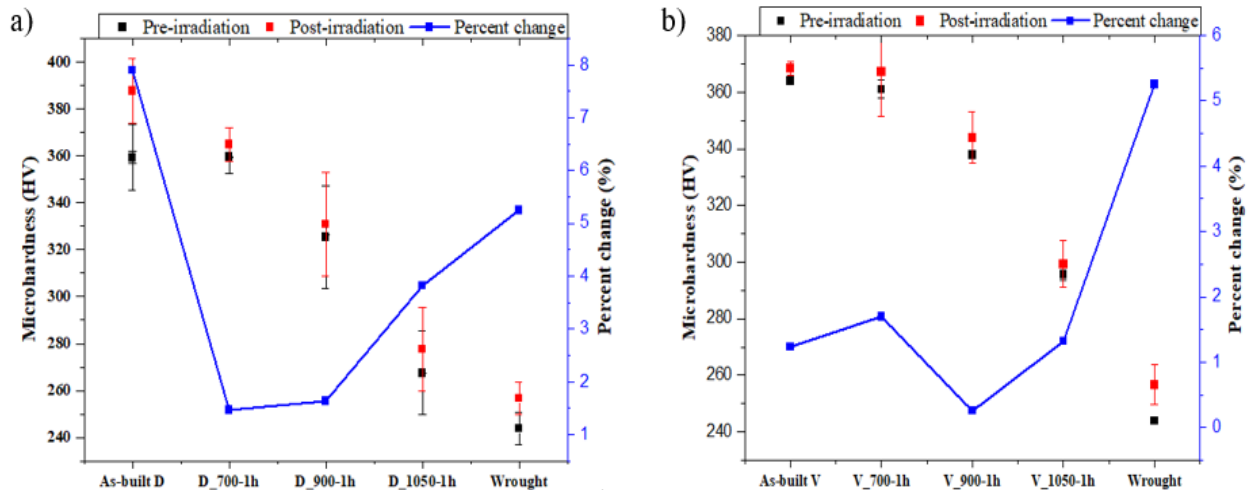
Figure 3.15. Pre and post thermal neutron irradiation microhardness measurements of (a) all diagonal oriented L-PBF and wrought IN625 specimens, and b) vertical orientated L-PBF and wrought IN625 samples. Percent change in microhardness is presented on the right Y-axis.

The sensitivity to radiation hardening in materials depends on the pre-irradiation microstructural features, which is determined by the fabrication and thermomechanical processes employed. Microstructural features include the amount and distribution of pre-existing dislocations, carbides, other precipitates, impurity segregation, inclusions, porosity, and so on. Increase in porosity level and size along the grain boundaries creates barrier for the dislocation motion under external force. The correlation between pre-irradiation porosity and microhardness percent change after neutron irradiation is presented in Figure 3.16. As it is observed in Figure 3.16 (a), the as-built diagonal sample has higher porosity which results in higher restriction in dislocation motion during the irradiation and ultimately causing higher percent change in microhardness post irradiation indicating a more pronounced hardening effect as compared to the vertical sample. A similar trend can be observed in the 1050 °C-1-hour heat treated vertical and diagonal samples as presented in Figure 3.16 (b).
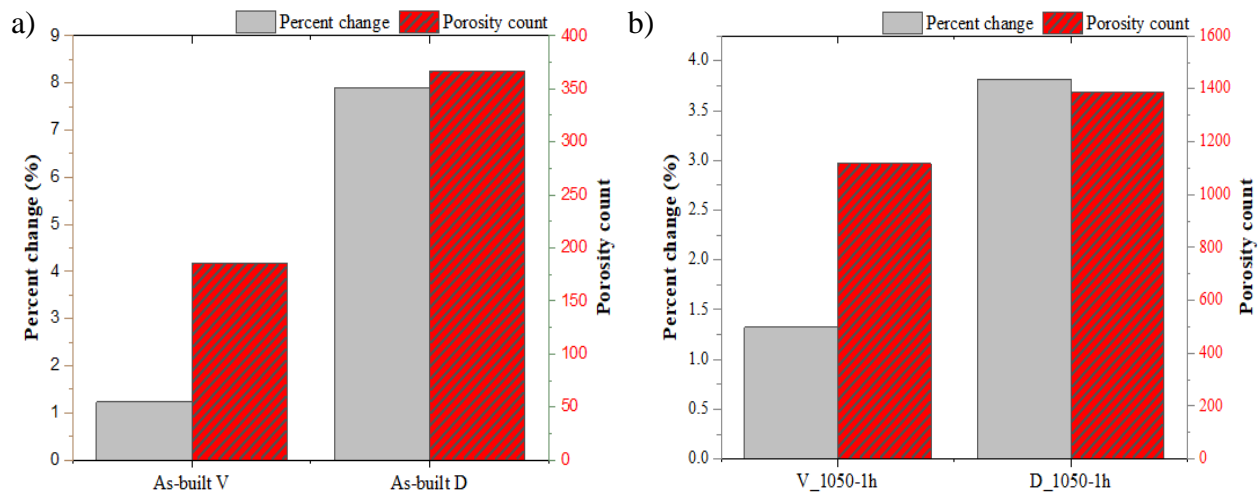
Figure 3.16. Correlation between pre-irradiation porosity levels and percent change in microhardness post full spectrum neutron irradiation in a) as-built vertical and b) 1050 °C- 1-hour heat-treated vertical (V) and diagonal (D) oriented IN625 samples.

3.2.3 FEA results

The deformation caused by the indenter after penetration in the sample is plotted in X and Y directions. The presence of stress on the sample surface was observed to have influence on the deformation caused by the indenter. The deformation in X-direction caused by the spherical indenter in the presence of tensile and compressive stress on the sample surface is shown in Figure 3.17(a) and (b), respectively. As seen in Figure 3.17(a) and (b), presence of tensile or compressive stress has effects on the deformation caused by the indentation. The tensile stressed sample had higher deformation compared to the compressively stressed sample. The compressed surface restricted the motion of spherical indenter into the sample and thus creates lower deformation compared to the tensile stressed surface. Similar results were plotted in the Y-direction. The deformation in the Y-direction for tensile and compressive stressed is shown in Figure 3.18 (a) and (b), respectively. The indenter is observed to caused maximum deformation of 591 and 540 μm in -Y direction in tensile and compressively stressed samples, respectively. This indicates that presence of tensile stress on the surface makes it easier for the indenter to deform the surface compared to the presence of compressive stress.

a)

Directional Deformation
Type: Directional Deformation(X Axis)
Unit: μm
Global Coordinate System
Time: 10 s

60.2 Max
45.5
30.8
16.1
1.45
-13.2
-27.9
-42.6
-57.3
-72 Min
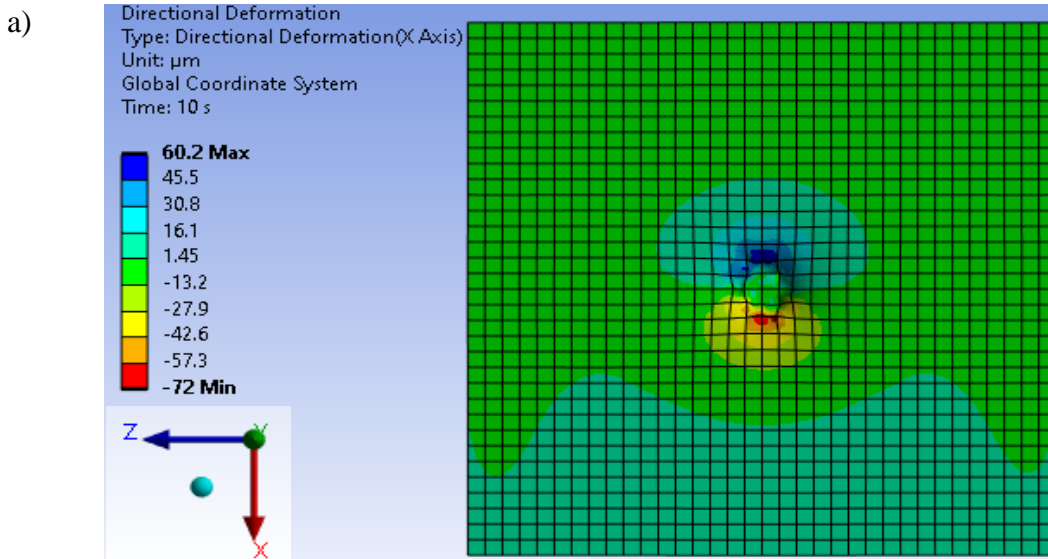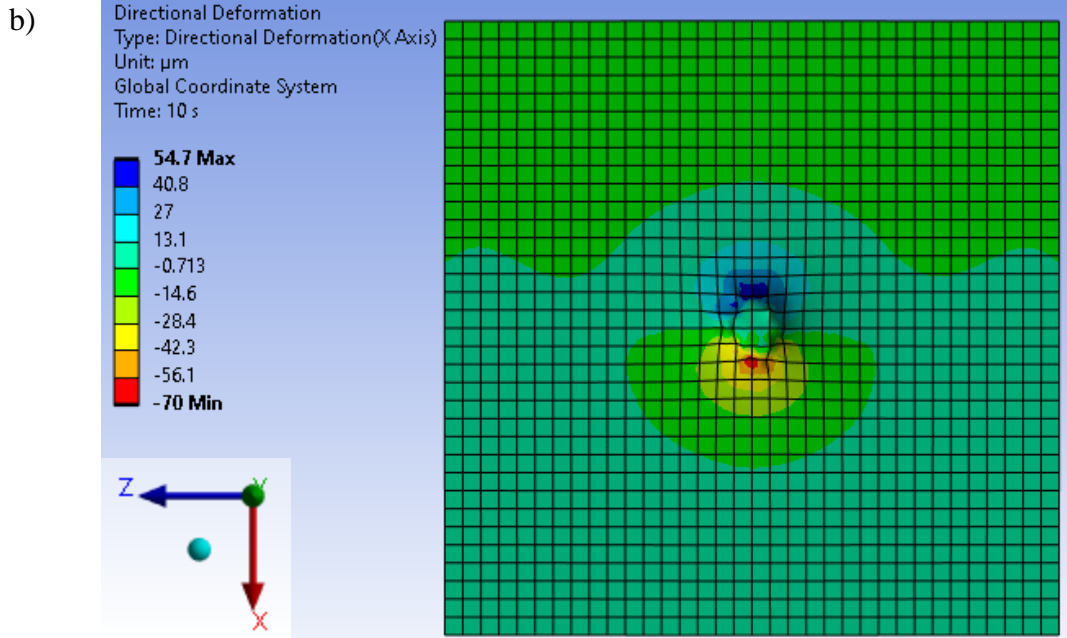
Figure 3.17. Deformation in X-direction caused by the spherical indenter in a) tensile stressed

and b) compressive stressed sample.

b)
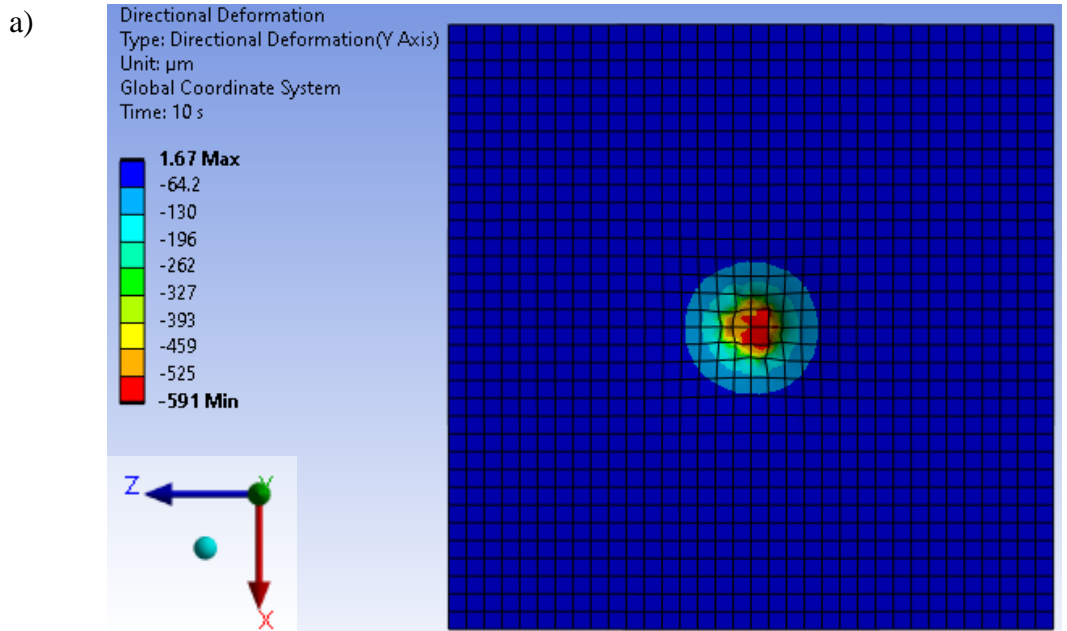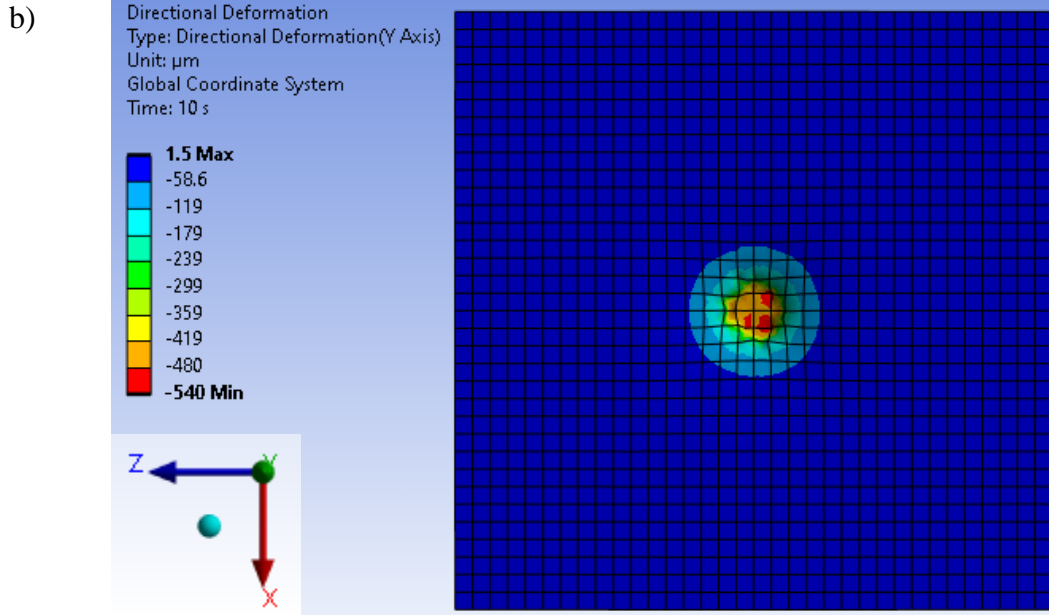
Figure 3.18. Deformation in Y-direction caused by the spherical indenter in a) tensile stressed and b) compressive stressed sample.

3.3 Concluding remarks

In this chapter, a successful full spectrum neutron irradiation experiment on L-PBF and wrought IN625 samples was conducted. The porosity level and size in the samples were investigated before the irradiation to understand its influence on post irradiation defect magnitude. Samples were irradiated in the highest and largest powered university level research reactor in the USA. The samples were irradiated for a total duration of 310 hours in the 10 MW reactor. The samples experienced a total fluence of 7.37 x 10^{19} neutrons/cm². Major conclusions drawn from this chapter are summarized below:

1. Porosity maps indicated the porosity count and size were influenced by different build orientations and heat-treatment at 1050 ℃-1-hour.

2. The sphericity of the pores was unaffected by different build orientations and heat-treatment.

3. The as-built vertical and diagonal L-PBF IN625 samples had higher pre-irradiation hardness values compared to the as-received wrought IN625 samples.

4. After irradiation, the as-built vertical L-PBF sample underwent less hardening (1.2%) than the as-built diagonal L-PBF sample (8%) indicating potential orientation effects. As-received wrought samples faced 5.25% irradiation-induced hardening.

5. Overall, the original hard L-PBF IN625 samples experienced lower irradiation-induced hardness change compared to the original softer wrought IN625 sample.

6. FEA simulation results demonstrate after applying compressive stress to the surface the deformation and penetration depth caused by spherical indenter was lower compared to when tensile stress is applied.

Chapter 4 - Fast Neutron Irradiation on IN625 & IN718

4.1 Experimental methods

4.1.1 AM process for IN718

The IN718 powder produced using gas atomization process was supplied by Carpenter Technologies. The powder particles had an average diameter size of 35 μm. The elemental composition of IN718 powder used in L-PBF in this study followed the ASTM F3055-14 standard for Additive Manufacturing Nickel Alloy (UNS N07718). L-PBF IN718 samples of dimensions 10 x 4 x 3 mm^3 were fabricated using a Concept Laser Mlab Cusing 100R system. The Concept Laser is equipped with a 100 W fiber laser with a wavelength of 1070 nm. The building process was carried out in an enclosed argon atmosphere for minimization of oxidization and spattering of powder upon its interaction with laser. The spattered powder can interact with the laser beam and create sparks which can ultimately damage the lens system. Samples as shown in Figure 4.1. were iteratively built at various process parameters and then inspected for density. The density matrix for laser power = 90 W and varying laser scan speed (mm/s) and hatch spacing (μm) is presented in Figure 4.2. Final process parameters consisting of power = 90 W, scan speed = 800 mm/s, laser diameter = 80 µm, hatch spacing = 60 μm, and layer thickness = 30 μm yielded 99.88% dense samples. The optimized sample is highlighted with an arrow in Figure 4.1 and designation number 14 in Figure 4.2. Other unoptimized samples possessed defects such as lack of fusion porosity and keyholes as seen in Figure 4.2. For baseline purposes, wrought IN718 plate was procured from Metalmen NY, USA. The plate was manufactured as per ASTM B 670-07 (2018). Small 7.5 x 5 x 3 mm^3 samples were sectioned from the plate using wire electrical discharge machining (EDM). The chemical composition of all forms of IN718 samples used in this study is indicated in Table 4.1.
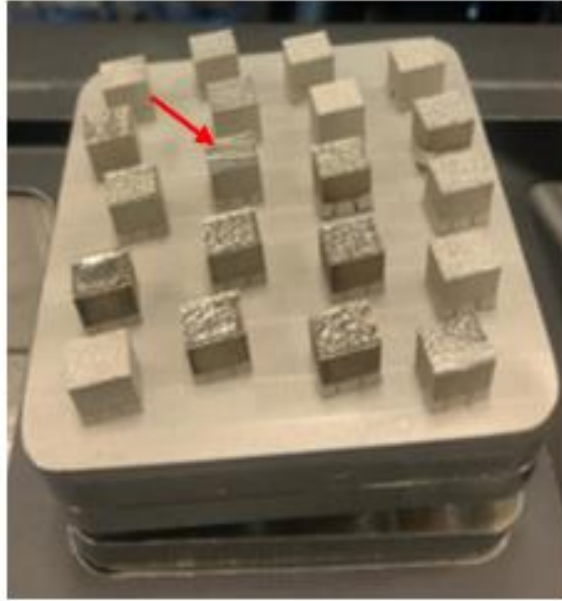
Figure 4.1. L-PBF IN718 samples on the substrate build using different process parameters

Highlighted sample indicate the optimized dense sample used in this study.
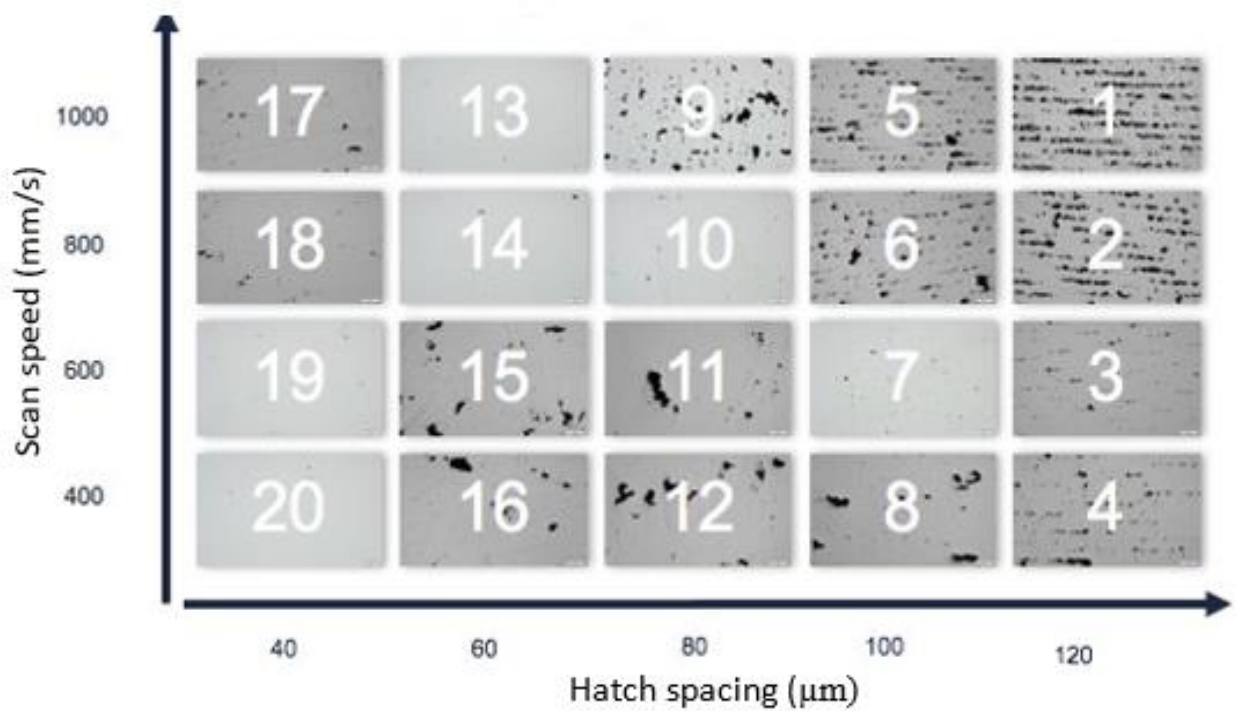
Figure 4.2. Density matrix prepared using different scan speed on Y-axis and hatch spacing on

X-axis for L-PBF IN718 samples. The dark regions represent defects in the sample.

Table 4.1. Elemental composition of L-PBF powder and wrought IN718 (% in weight).

% wt.	Ni	Cr	Mo	Fe	Nb+Ta	Co	C	P	Ti	Al
ASTM	50-55	17-21	2.8-3.3	Bal	4.75-5.5	<1	<0.06	<0.015	0.65-1.15	0.2-0.8
L-PBF	50-55	17-21	2.8-3.3	Bal	5.22	<1	0.05	<0.015	0.75-1.15	0.3-0.7
Wrought	53.55	18.76	2.95	17.5	5.08	0.16	0.03	0.01	0.97	0.55

The scan strategy employed to print IN718 samples was same as that used to print IN625 samples (i.e., island strategy). Like the as-built IN625 sample, the as-built IN718 sample was subjected to three heat-treatment temperatures for 1-hour. The three temperatures are 700, 900, and 1050 ℃. The rationale behind selecting these temperatures was the formation of δ phase in L-PBF IN718 as discussed in the TTT diagram in Chapter 1. Heating ramps used during heat treatment were ~5 ℃/min. All specimens were subjected to air cooling to room temperature while remaining in the furnace. The uncertainty in heat treatment temperatures is ± 5 ℃.

4.1.2 Fast neutron irradiation

Fast neutron irradiation was conducted using a positron emission tomography (PET) cyclotron located at the University of Missouri Research Reactor (MURR). The fast neutrons were generated as a by-product following the ^{18}O (p, n) ^{18}F reaction and were used to bombard IN625 and IN718 samples as shown in Figure 4.3. Four individual sets of IN625 and IN718 samples were irradiated together using the fast neutrons for 7, 12, 17, and 22 weeks. Meaning, after 7 weeks, for example, one of the four sets (consisting of L-PBF IN625, L-PBF IN718, and wrought samples) would be removed, thus leaving 3 remaining sets. The corresponding neutron fluence for each set is shown in Table 4.2. Vickers microhardness measurements were performed following ASTM

E92-23 using a Phase II 900-391D microhardness system. Hardness measurements on irradiated

specimens were performed in a hot cell using robotic manipulator arms for safety.
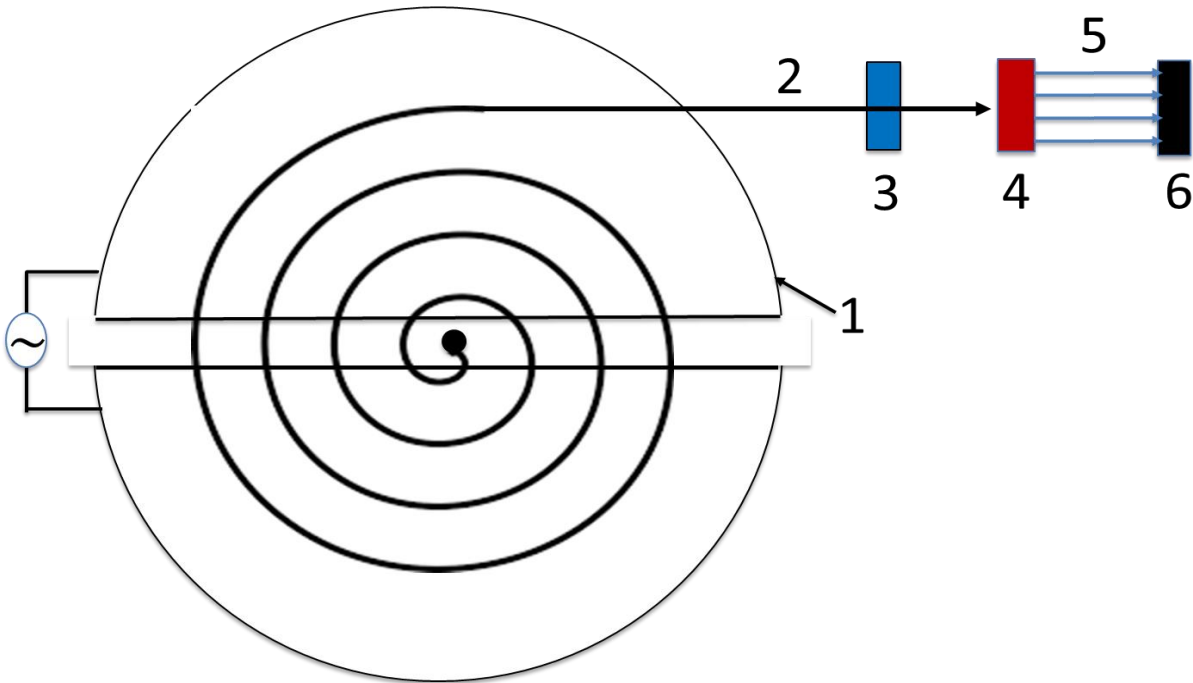
Figure 4.3. Schematic of employed cyclotron and its operation showing: (1) dees, (2) accelerated

proton, (3) charge filter, (4) fluorine target, (5) fast neutrons emitted, and (6) IN625 and IN718

samples.

Table 4.2. Approximate irradiation time with corresponding neutron fluence (n/m^2) for each set of

samples investigated.

Irradiation Time	Neutron Fluence (n/m²)
7 weeks	2.74×10^{19}
12 weeks	6.61×10^{19}
17 weeks	7.90×10^{19}
22 weeks	9.67×10^{19}

4.2 Results & discussions

4.2.1 7-weeks of fast neutron irradiation

The microhardness of L-PBF and wrought IN625 and IN718 samples after 7, 12, 17, and 22 weeks of fast neutron irradiation are presented in Figures 4.4. and 4.5., respectively. Results indicate that the initial 7 weeks of fast neutron irradiation resulted in hardening/embrittlement in almost all IN625 samples while the IN718 samples experienced only minimal hardening. The wrought IN625 sample hardened more than all L-PBF IN625 samples, changing from 244.4 ± 5.7 HV to 262.1 ± 11 HV with an overall percent change of +7.2%, while the as-built L-PBF samples only changed from 327.3 ± 9.2 HV to 330.3 ± 9.5 HV with an overall percent change of +0.9%. The pronounced hardening is most likely due to the formation of helium (He) bubbles along the grain boundaries. He is produced during the transmutation process caused by nuclear reactions triggered by fast neutrons. These reactions, which include neutron capture followed by α-particle ($^4\text{He}^{2+}$) emission (n, α), and neutron capture and proton emission (n, p), have a lower probability of occurring than the major (n, γ) reactions but still have a much greater effect on material properties. He particles, even in small concentration, can have significant life-limiting repercussions for materials. Because of its limited solubility in the crystal lattice, He accumulates around defects, dislocations, and grain boundaries, resulting in embrittlement. He bubbles can embrittle grain boundaries by the stress developed growth of voids along the grain boundaries [159]. He is primarily produced in Ni-based superalloys by high energy (fast) neutron reactions in natural Ni containing 68% ^{58}Ni and 26% ^{60}Ni, with the fast neutron (n, α) reactions. This can be explained by the neutron reactions presented in equations (4.1) and (4.2) [160].

$$^{58}\text{Ni} + \text{n}_\text{f} \rightarrow {}^{55}\text{Fe} + {}^4\text{He} \tag{4.1}$$

$$^{60}\text{Ni} + \text{n}_f \rightarrow {}^{57}\text{Fe} + {}^{4}\text{He} \tag{4.2}$$

Although hardness increased only slightly after the 7-week irradiation period, this can be an indicator of crack initiation/development within the samples. The irradiation-induced hardening was almost identical in all IN718 samples, independent of heat treatment, including wrought. This suggests that the structural integrity of L-PBF components under fast neutron irradiation is comparable to that of traditional wrought samples. Fast neutron irradiation had a greater effect on IN625 samples. IN718 was more resistant to radiation hardening defects, presumably because IN718 contains more Nb and Ta composition which leads to the formation γ' and γ" precipitates which act as a sink for irradiation point defects such as interstitials and vacancies [161]. Also, IN718 is generally known for its high strength at high temperatures while IN625 is more known for its corrosion resistance [162]. Similar radiation hardening or embrittlement in different materials under a similar fluence have also been reported in the past [158], [163], [164].

4.2.2 12-weeks of fast neutron irradiation

For 12 weeks of total irradiation time, IN625 samples were observed to harden less, and even often, when compared to the 7-week irradiated samples. L-PBF IN718 samples softened instead of hardening like that observed in its counterpart wrought sample. In the as-built IN718 sample, the average hardness slightly changed from 326.6 $\pm$ 6.2 HV to 324.4 $\pm$ 13.6 HV with an overall percent change -0.7%, and in the wrought, from 232.4 $\pm$ 4.2 HV to 257.4 $\pm$ 8.6 HV with an overall percent change +10.75%. This significant hardening in the wrought IN718 sample is most likely due to the formation of defect clusters mitigating the sliding of dislocations under the external load imposed from the Vickers indenter. The 700 ℃ 1-hour heat treated IN625 and IN718 samples experienced softening since they potentially contained the γ' precipitates. The softening effect, also known as 'irradiation softening', results from the distortion of ordered strengthening

γ' precipitates formed along the grain boundaries during the L-PBF process [165]. Increasing the neutron fluence on the samples, the microhardness measurements were observed to decrease. There appears to be a balancing effect of hardening and softening in all samples at this fluence level. IN625 samples were still observed to have higher variation in hardness compared to IN718 samples indicating, to some extent, lower structural integrity.
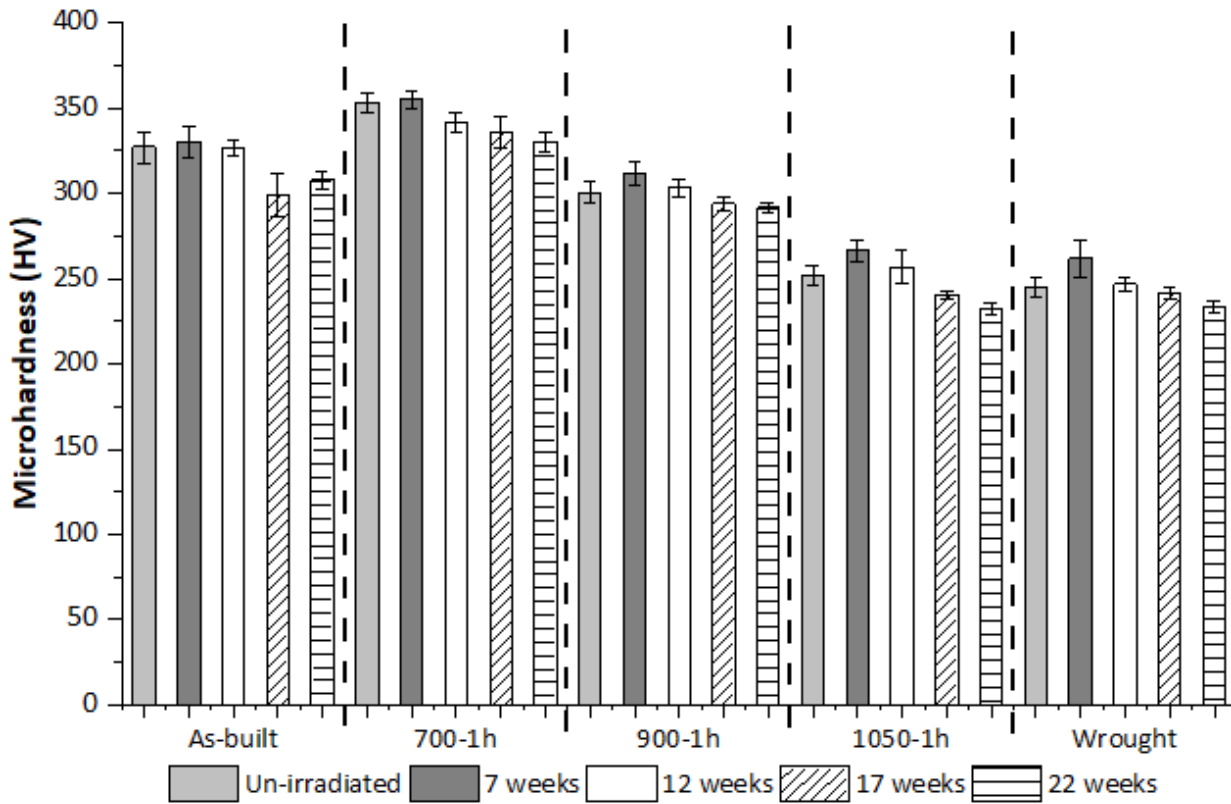
Figure 4.4. Microhardness of as-built L-PBF, heat treated L-PBF, and wrought IN625 samples in un-irradiated and irradiated states.
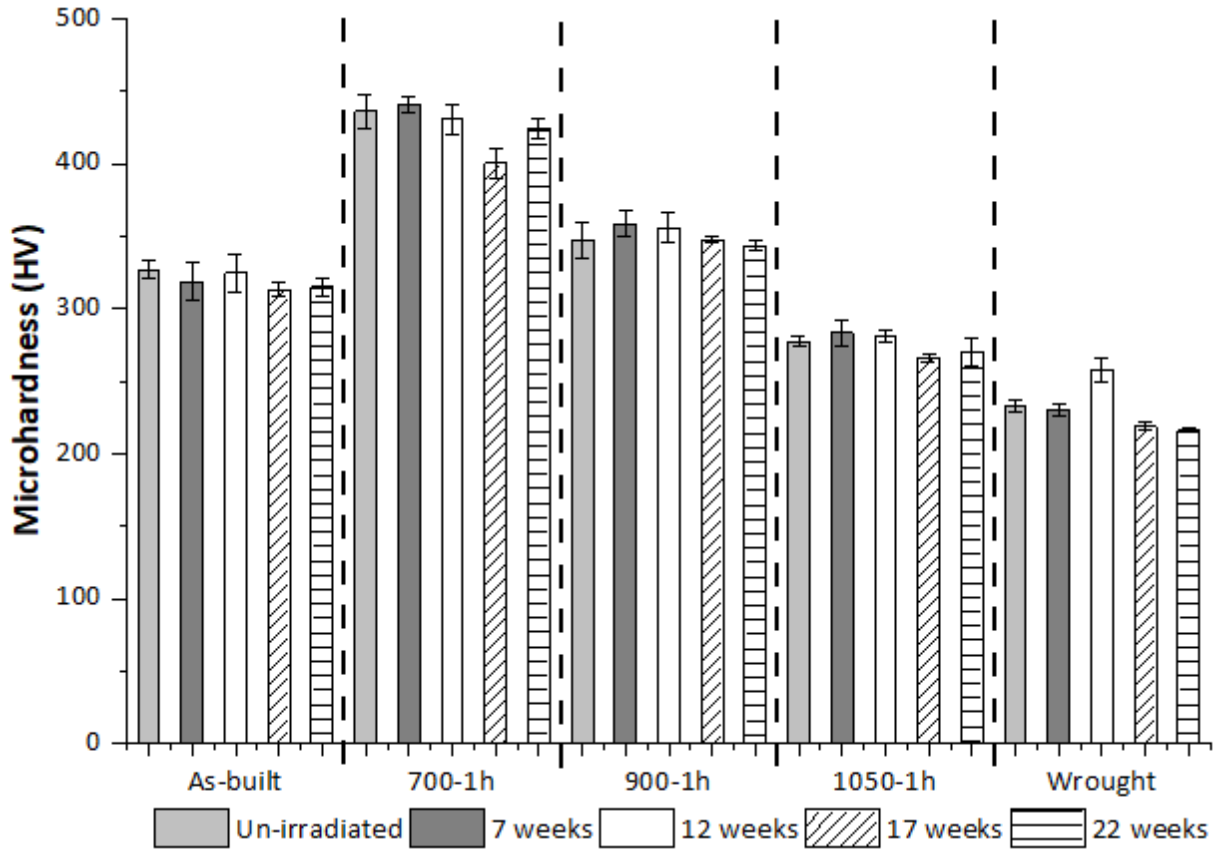
Figure 4.5. Microhardness of as-built L-PBF, heat treated L-PBF, and wrought IN718 samples in un-irradiated and irradiated states.

4.2.3 17-and-22 weeks of fast neutron irradiation

For experiments providing 17 and 22 weeks of total irradiation time, all IN625 and IN718 experienced radiation softening. The neutron fluence experienced by the samples after 17 and 22 weeks was 7.9 x 10^{19} n/m^2 and 9.67 x 10^{19} n/m^2, respectively. After 17 weeks of irradiation, neither the IN625 nor the IN718 samples demonstrated radiation hardening defects as presented in Figures 4.4 and 4.5. The as-built IN625 sample experienced radiation softening where its hardness changed from 327.3 ± 9.2 HV to 299.0 ± 12.5 HV with an overall percent change of -8.6%. On the other hand, the as-built L-PBF IN718 hardness changed from 326.6 ± 6.2 HV to 312.9 ± 4.8 HV with an overall percent change of -4.2%. This indicates that the IN718 sample had more tolerant to

neutron irradiation effect relative to the IN625 sample under the same neutron fluence. A similar trend was observed after 22 weeks of irradiation as shown in Figures 4.4 and 4.5. The as-built IN625 sample experienced radiation softening where its hardness changed from 327.3 ± 9.2 to 308 ± 5.0 HV with an overall percent change of -5.9%. On the other hand, the as-built L-PBF IN718 sample hardness decreased from 326.6 ± 6.2 to 314.9 ± 6.7 with an overall percent change of -3.6%. At this stage, the samples experienced enough neutron fluence to cause potential disintegration of dislocations and He bubbles to free the grain boundaries motion under an external load. The prolonged fast neutron bombardment potentially generated enough kinetic energy that was transferred to the dislocations, solute-segregated particles, and precipitates along the grain boundaries, removing the impediments for gliding dislocations under the external load of the Vickers indenter. Similar softening effects after exposure to various irradiation environments in different materials have also been reported [166]–[168].

4.3 Concluding remarks

In this chapter, a successful accelerated nuclear irradiation experiment was performed on two Inconel alloys i.e., IN625 & IN718. Samples irradiated were in the L-PBF as-built, three different heat-treated and wrought IN625 and IN718 conditions. This was an accelerated method of irradiation in the sense that the fast neutrons used in this study did not result in much radioactivity in the samples and the post-irradiation testing was performed in a quicker time compared to the full-spectrum neutron irradiated samples. Four individual sets of IN625 and IN718 samples were irradiated together using the fast neutrons for 7, 12, 17, and 22 weeks. Meaning, after 7 weeks, for example, one of the four sets (consisting of L-PBF IN625, L-PBF IN718, and wrought samples) was removed, thus leaving 3 remaining sets. The major observations from this chapter are summarized below:

1. The pre-irradiation hardness of IN718 samples indicate a spike after heat-treated at 700 ℃ for 1-hour. This increase in the hardness can be attributed to the formation of hardening γ'' phase in the microstructure that potentially increased the resistance of the sliding dislocations under the indenter's external force.

2. After the initial 7 weeks of irradiation, almost all samples experienced irradiation-induced hardening effect. IN625 samples were observed to have more irradiation-hardening compared to IN718 samples.

3. After 12 weeks of irradiation, the wrought IN718 sample was the standout with the highest irradiation hardening effect. Overall, the IN625 samples still experienced higher hardness fluctuations compared to IN718 samples indicating lower structural integrity.

4. Post 17-and-22 weeks, a majority of the IN625 and IN718 samples experienced irradiation-induced softening effect due to the potential microstructure refinement and reduction of dislocations.

Chapter 5 - Conclusions

The present work was dedicated to investigating the effects of nuclear irradiation on additive manufactured (AM) Inconel 625 and 718 nickel superalloys. Firstly, the defect arising during the laser powder bed fusion (L-PBF) AM technology. The microstructure of L-PBF produced samples is studied and compared with the conventionally machined one. Detrimental residual stress was measured using the novel Cos α X-ray diffraction method. The effects of build orientations adopted during the L-PBF process and heat treatment temperatures on residual stress measurement and microstructure were studied. Secondly, the L-PBF and wrought IN625 samples were irradiated in the 10 MW nuclear reactor using thermal neutrons and the neutron irradiation-induced hardening defect was measured. Finally, the IN625 and IN718 samples were irradiated using the accelerated irradiation technique of using fast neutrons. The neutron irradiation hardening defect and the structural integrities of L-PBF and wrought IN625 and IN718 samples were evaluated and compared. The major conclusions drawn from this dissertation are summarized below:

5.1 Residual stress

1) The as-built vertically oriented sample exhibited higher tensile residual stress value (77 $\pm$ 15 MPa) compared to diagonally printed sample (52 $\pm$ 12 MPa). This is inherited from the L-PBF additive manufacturing process which includes high thermal gradient. High thermal gradient occurs from simultaneous laser heat and solidification provided by relatively cooler build substrate.

2) Post 700, 900, and 1050 ℃ heat treatments, the detrimental tensile residual stress on as-built surface was transformed to compressive residual stress which helps improve the

fatigue life, fatigue strength, slow crack propagation, and increase resistance to environmentally assisted cracking.

5.2 Microstructure analysis

1) The relaxation in residual stress is confirmed with recrystallization of grains observed in EBSD results. The as-built vertical and diagonally printed samples displayed columnar grains oriented parallel to build direction. Post 1050 ℃ heat treatment, the columnar grains were changed to equiaxed grains larger in size and arranged in random orientations. Wrought sample had small equiaxed grains oriented in random orientations.

2) Twinning was observed in the 1050 ℃ heat treated IN625 sample indicating initialization of microstructure recrystallization process.

3) Kernel average misorientation maps showed the as-built vertically printed sample inherited most dense dislocations which contributes to high residual stress. Post 1050 ℃-1-hour heat treatment, the dislocations reduced significantly and so did the tensile residual stress.

5.3 Nano-indentation

1) Nano-indentation results confirmed the as-built vertically and diagonally printed samples showed the highest average value (3.74 GPa). Standard deviation in nano hardness of vertically printed sample was highest which results from anisotropic microstructure. Post 1050 ℃ heat treatment the nano-hardness reduced significantly to 2.98 GPa and showed uniform property with lower standard deviations in values. The 1050 ℃ sample showed similar nano-hardness values as wrought IN625 sample (3.25 GPa).

5.4 Porosity analysis

1) Porosity analysis of pre-irradiated L-PBF IN625 samples indicates that both build orientation and heat treatment affect pore count and size. As-built vertically build sample had a lower porosity count (186) compared to the as-built diagonally build sample (367).

2) Heat treating the as-built samples increased the pore size and number indicating increase in the gas pore pressure. As-built vertical and diagonal oriented samples had an average pore diameter 60.23 ± 10 and 59 ± 8 μm, respectively. Heat treating at 1050 °C-1-hour increased it to 67.35 ± 10 and 68.48 ± 10.5 μm, respectively.

3) The pore sphericity was observed to remain unaffected at 0.94 ± 0.2 regardless of changing the build orientation or heat treating at 1050 °C for 1-hour.

5.5 Pre-irradiation hardness

1) The as-built vertical (364 ± 1.175 HV) and diagonal (359.25 ± 2.625 HV) L-PBF IN625 samples had higher pre-irradiation hardness values compared to the as-received wrought (243.85 ± 1.15 HV) IN625 samples.

2) After the 700 °C for 1-hour heat treatment, L-PBF IN718 sample was observed to have a spike in microhardness value indicating formation of precipitates that restrict the motion of dislocation that ultimately resulted in the higher hardness.

3) In IN625 samples, it was observed that the microhardness value kept decreasing as the heat treatment temperature was increasing. After the 1050 °C- for 1-hour heat treatment, the microhardness value was close to the as-received wrought sample microhardness value.

5.6 L-PBF vs wrought irradiation effects

1) Even after modest thermal neutron irradiation, all IN625 samples experienced radiation damage in the form of hardening.

2) The as-built, vertical, L-PBF sample underwent less hardening (1.2%) than the as-built, diagonal, L-PBF sample (8%) indicating orientation effects. The as-received wrought samples showed an irradiation-induced hardening of 5.25%.

3) The correlation between porosity and the percent change in microhardness after irradiation indicates that a higher part porosity results in higher irradiation-induced hardening.

4) All vertically oriented L-PBF IN625 samples displayed more resistance to radiation hardening (lower percent change) as compared to wrought IN625 samples (higher percent change).

5) Overall, the original hard L-PBF IN625 samples experienced lower irradiation-induced hardness change compared to the original softer wrought IN625 sample. This is an indication that the finer microstructure in L-PBF samples reduced the irradiation-induced hardening effect.

6) Post 7-weeks of fast neutron irradiation, the wrought IN625 sample underwent microhardness change of 7.18% compared to the 0.91% in as-built L-PBF IN625 sample indicating AM part showed better resistance to the hardening defect.

7) For both materials i.e., IN625 and IN718, heat treatment schedule of 1050 ℃-1h, proved to be most optimal one to resist radiation hardening or softening effect caused by the fast neutrons. Considering all four sets, average percent change for 1050 ℃ for 1-hour heat treated IN625 and IN718 samples was -1.09 and -0.73%, respectively.

8) After 12 weeks of fast neutron irradiation, the as-built IN718 sample experienced a percent change of -0.7%, and the wrought underwent a percent change of +10.75% in microhardness. This again represented the strong structural integrity of L-PBF sample after irradiation.

9) After 22 weeks of irradiation, for a total fluence of 9.67×10^{19} n/m^2, the L-PBF IN625 samples experienced a more softening effect. All IN625 samples had an average percent change of -5.75% while IN718 samples still maintained their structural integrity with a lower average percent change of -2.45%.

5.7 Goal accomplishment

The main goal of this dissertation was to tailor the properties of AM metal to make it more resistant towards nuclear irradiation hardening damage as compared to conventionally-built (wrought) metal. This goal was achieved by addressing the two objectives mentioned in Section 1.6. The first objective was to determine how to mitigate residual stress and porosity defects by using different AM build orientations and post-processing heat-treatment schedules to make AM nickel superalloys safer for nuclear energy applications. This was achieved by varying in-process (build orientation) and post-processing (heat-treatment schedule) parameters. The high, detrimental tensile residual stress is formed on the surface of as-built L-PBF samples due to the high thermal gradient generated during the AM process. This was mitigated by performing post-processing heat treatment at, or above, annealing temperatures. Heat treatment recrystallized the microstructure and relaxed the plastic strains present in the as-built AM samples. The plastic strains were caused by the presence of dislocations and performing heat treatment eliminated them. The porosity defect can be alleviated by using either different build orientations during the AM process or post-processing heat-treatment schedules. Changing the build orientation affects the inter-layer adhesion and influences the porosity level formed in the part. After mitigating the residual stress and porosity defects in the AM IN625 part, it was made more desirable for the neutron irradiation experiments. In addition, key process-structure-property relationships were learned.

The second objective was to discover how AM metals can be tailored to make them more tolerant towards full-spectrum and fast neutron irradiation induced hardening compared to their wrought counterparts. This was accomplished by performing post full-spectrum and fast neutron irradiation experiments on AM and wrought nickel-superalloys. AM IN625 samples showed lower percent hardening damage compared to wrought samples due to the potential factors such as high pre-irradiation hardness in AM IN625 samples which makes it difficult to produce neutron irradiation induced hardening effects. The diagonally-built samples had higher porosity compared to vertically-built samples which resulted in a higher percent increase in microhardness post-irradiation. The high porosity creates additional obstacles for the dislocation motion under the external pressure applied by the hardness indenter. After fast neutron irradiation, the heat-treatment schedule of 900 ºC - 1h, proved to be the most optimal one for AM IN625 to resist radiation hardening/softening damage after fast neutron irradiation. On the other hand, heat-treatment of 1050 ºC - 1h, proved to be the most optimal one for AM IN718 to resist radiation hardening/softening damage. Overall, it can be concluded that tailoring the microstructure and mechanical properties of pre-irradiated AM built IN625 and IN718 samples can make them as resistant or more to irradiation induced hardening damage compared to the conventionally machined metals. The experimental research data from this dissertation can enhance the confidence among engineers in considering AM technology as an alternative manufacturing method for the advance nuclear reactor components.

5.8 Future work

Future research work may include performing a detailed microstructure analysis of pre-irradiation and post-irradiation samples. This can be done using scanning electron microscopy (SEM) on bulk Inconel samples to observe any presence of neutron irradiation induced line defects

such as dislocations and volume defects such as voids and helium embrittlement. Additionally, creating small volume lamella from Inconel samples and irradiating them at higher neutron fluence can be done. Investigating the small volume lamella using the transmission electron microscopy (TEM) technique can be performed for high resolution microstructure analysis post-irradiation.

Bibliography

[1]   V. O'Donnell *et al.*, "Diagnostic Technique Characterizing Neutron Irradiation Effects on Additively Manufactured Inconel 625 Eliminating the Need for Remote Handling," *Nucl. Technol.*, vol. 209, no. 2, pp. 254–260, 2023, doi: 10.1080/00295450.2022.2120321.

[2]   T. Rayna and L. Striukova, "From rapid prototyping to home fabrication: How 3D printing is changing business model innovation," *Technol. Forecast. Soc. Change*, vol. 102, pp. 214–224, 2016, doi: 10.1016/j.techfore.2015.07.023.

[3]   International Organization for Standardization (ISO), "Additive manufacturing-General principles-Fundamentals and vocabulary Fabrication additive-Principes généraux-Fondamentaux et vocabulaire International Standard ISO/ASTM 52900:2021(E) Copyright Protected Document," vol. 2021, 2021.

[4]   S. H. Huang, P. Liu, A. Mokasdar, and L. Hou, "Additive manufacturing and its societal impact: A literature review," *Int. J. Adv. Manuf. Technol.*, vol. 67, no. 5–8, pp. 1191–1203, 2013, doi: 10.1007/s00170-012-4558-5.

[5]   C. Klahn, B. Leutenecker, and M. Meboldt, "Design strategies for the process of additive manufacturing," *Procedia CIRP*, vol. 36, pp. 230–235, 2015, doi: 10.1016/j.procir.2015.01.082.

[6]   A. J. Dunbar *et al.*, "Development of experimental method for in situ distortion and temperature measurements during the laser powder bed fusion additive manufacturing process," *Addit. Manuf.*, vol. 12, pp. 25–30, 2016, doi: 10.1016/j.addma.2016.04.007.

[7]   L. Cherdo, "Metal 3D printers in 2023: a comprehensive guide," *Aniwaa*, 2022. https://www.aniwaa.com/buyers-guide/3d-printers/best-metal-3d-printer/

[8]   D. Thomas, *Costs, benefits, and adoption of additive manufacturing: a supply chain*

perspective, vol. 85, no. 5–8. 2016. doi: 10.1007/s00170-015-7973-6.

[9]   C. W. J. Lim, K. Q. Le, Q. Lu, and C. H. Wong, "An Overview of 3-D Printing in Manufacturing, Aerospace, and Automotive Industries," *IEEE Potentials*, vol. 35, no. 4, pp. 18–22, 2016, doi: 10.1109/MPOT.2016.2540098.

[10]   R. Russell *et al.*, *Qualification and certification of metal additive manufactured hardware for aerospace applications*. 2019. doi: 10.1016/B978-0-12-814062-8.00003-0.

[11]   B. Jackson;, "GE AVIATION CELEBRATES 30000th 3D PRINTED FUEL NOZZLE," *3D Printing Industry*, 2018. https://3dprintingindustry.com/news/ge-aviation-celebrates-30000th-3d-printed-fuel-nozzle-141165/

[12]   M. E. Orme *et al.*, "Additive Manufacturing of Lightweight, Optimized, Metallic Components Suitable for Space Flight," *J. Spacecr. Rockets*, vol. 54, no. 5, pp. 1050–1059, 2017, doi: 10.2514/1.A33749.

[13]   R. Bracci, E. Maccaroni, and S. Cascinu, "Transient Sunitinib Resistance in Gastrointestinal Stromal Tumors," *N. Engl. J. Med.*, vol. 368, no. 21, pp. 2042–2043, 2013, doi: 10.1056/nejmc1301237.

[14]   S. Kondor *et al.*, "Personalized Surgical Instruments," *J. Med. Device.*, vol. 7, no. 3, p. 30934, 2013, doi: 10.1115/1.4024487.

[15]   C. G. Sandström, "The non-disruptive emergence of an ecosystem for 3D Printing - Insights from the hearing aid industry's transition 1989-2008," *Technol. Forecast. Soc. Change*, vol. 102, pp. 160–168, 2016, doi: 10.1016/j.techfore.2015.09.006.

[16]   "Framatome installs first 3D-printed stainless steel fuel component at Forsmark Nuclear Power Plant," *Framatome*, 2022. https://www.framatome.com/medias/framatome-installs-first-3d-printed-stainless-steel-fuel-component-at-forsmarknuclear-power-plant/?lang=en

[17]   "Siemens sets milestone with first 3D-printed part operating in nuclear power plant," *Siemens Press*, 2017. https://press.siemens.com/middleeast/en/pressrelease/siemens-sets-milestone-first-3d-printed-part-operating-nuclear-power-plant

[18]   A. Thompson, I. Maskery, and R. K. Leach, "X-ray computed tomography for additive manufacturing: a review," *Meas. Sci. Technol.*, vol. 27, no. 7, p. 72001, Jun. 2016, doi: 10.1088/0957-0233/27/7/072001.

[19]   A. Yadollahi and N. Shamsaei, "Additive manufacturing of fatigue resistant materials: Challenges and opportunities," *Int. J. Fatigue*, vol. 98, pp. 14–31, 2017, doi: https://doi.org/10.1016/j.ijfatigue.2017.01.001.

[20]   S. A. Khairallah *et al.*, "Controlling interdependent meso-nanosecond dynamics and defect generation in metal 3D printing," *Science (80-.).*, vol. 368, no. 6491, pp. 660–665, 2020, doi: 10.1126/science.aay7830.

[21]   M. Zheng *et al.*, "A novel method for the molten pool and porosity formation modelling in selective laser melting," *Int. J. Heat Mass Transf.*, vol. 140, pp. 1091–1105, 2019, doi: https://doi.org/10.1016/j.ijheatmasstransfer.2019.06.038.

[22]   H.-W. Mindt, O. Desmaison, M. Megahed, A. Peralta, and J. Neumann, "Modeling of Powder Bed Manufacturing Defects," *J. Mater. Eng. Perform.*, vol. 27, no. 1, pp. 32–43, 2018, doi: 10.1007/s11665-017-2874-5.

[23]   Y. Tian, L. Yang, D. Zhao, Y. Huang, and J. Pan, "Numerical analysis of powder bed generation and single track forming for selective laser melting of SS316L stainless steel," *J. Manuf. Process.*, vol. 58, pp. 964–974, 2020, doi: https://doi.org/10.1016/j.jmapro.2020.09.002.

[24]   C. Qiu, C. Panwisawas, M. Ward, H. C. Basoalto, J. W. Brooks, and M. M. Attallah, "On

the role of melt flow into the surface structure and porosity development during selective laser melting," *Acta Mater.*, vol. 96, pp. 72–79, 2015, doi: https://doi.org/10.1016/j.actamat.2015.06.004.

[25] S. M. Thompson and N. B. Crane, "Process Defects in Metal Additive Manufacturing," in *Additive Manufacturing Design and Applications*, ASM International, 2023. doi: 10.31399/asm.hb.v24A.a0006972.

[26] H. L. Wei, Y. Cao, W. H. Liao, and T. T. Liu, "Mechanisms on inter-track void formation and phase transformation during laser Powder Bed Fusion of Ti-6Al-4V," *Addit. Manuf.*, vol. 34, no. March, 2020, doi: 10.1016/j.addma.2020.101221.

[27] E. Brandl, U. Heckenberger, V. Holzinger, and D. Buchbinder, "Additive manufactured AlSi10Mg samples using Selective Laser Melting (SLM): Microstructure, high cycle fatigue, and fracture behavior," *Mater. Des.*, vol. 34, pp. 159–169, 2012, doi: https://doi.org/10.1016/j.matdes.2011.07.067.

[28] B. Gorny, T. Niendorf, J. Lackmann, M. Thoene, T. Troester, and H. J. Maier, "In situ characterization of the deformation and failure behavior of non-stochastic porous structures processed by selective laser melting," *Mater. Sci. Eng. A*, vol. 528, no. 27, pp. 7962–7967, 2011, doi: 10.1016/j.msea.2011.07.026.

[29] T. Vilaro, C. Colin, and J. D. Bartout, "As-fabricated and heat-treated microstructures of the Ti-6Al-4V alloy processed by selective laser melting," *Metall. Mater. Trans. A Phys. Metall. Mater. Sci.*, vol. 42, no. 10, pp. 3190–3199, 2011, doi: 10.1007/s11661-011-0731-y.

[30] S. Pal, G. Lojen, V. Kokol, and I. Drstvensek, "Evolution of metallurgical properties of Ti-6Al-4V alloy fabricated in different energy densities in the Selective Laser Melting

technique," *J. Manuf. Process.*, vol. 35, no. November 2017, pp. 538–546, 2018, doi: 10.1016/j.jmapro.2018.09.012.

[31] G. Kasperovich, J. Haubrich, J. Gussone, and G. Requena, "Correlation between porosity and processing parameters in TiAl6V4 produced by selective laser melting," *Mater. Des.*, vol. 105, pp. 160–170, 2016, doi: https://doi.org/10.1016/j.matdes.2016.05.070.

[32] X. Zhou *et al.*, "3D-imaging of selective laser melting defects in a Co-Cr-Mo alloy by synchrotron radiation micro-CT," *Acta Mater.*, vol. 98, pp. 1–16, 2015, doi: 10.1016/j.actamat.2015.07.014.

[33] A. Du Plessis, "Porosity in laser powder bed fusion," *Fundam. Laser Powder Bed Fusion Met.*, pp. 155–178, 2021, doi: 10.1016/B978-0-12-824090-8.00007-X.

[34] P. Nandwana, M. M. Kirka, V. C. Paquit, S. Yoder, and R. R. Dehoff, "Correlations Between Powder Feedstock Quality, In Situ Porosity Detection, and Fatigue Behavior of Ti-6Al-4V Fabricated by Powder Bed Electron Beam Melting: A Step Towards Qualification," *Jom*, vol. 70, no. 9, pp. 1686–1691, 2018, doi: 10.1007/s11837-018-3034-6.

[35] H. Choo *et al.*, "Effect of laser power on defect, texture, and microstructure of a laser powder bed fusion processed 316L stainless steel," *Mater. Des.*, vol. 164, p. 107534, 2019, doi: https://doi.org/10.1016/j.matdes.2018.12.006.

[36] J. B. Forien, J. D. Philip, G. M. Guss, B. H. Jared, J. D. Madison, and M. J. Matthews, "Effect of laser power on roughness and porosity in laser powder bed fusion of stainless steel 316L alloys measured by X-ray tomography," *Int. J. Mater. Res.*, vol. 111, no. 1, pp. 47–54, 2020, doi: 10.3139/146.111816.

[37] H. Hassanin, F. Modica, M. A. El-Sayed, J. Liu, and K. Essa, "Manufacturing of Ti–6Al–

4V Micro-Implantable Parts Using Hybrid Selective Laser Melting and Micro-Electrical Discharge Machining," *Adv. Eng. Mater.*, vol. 18, no. 9, pp. 1544–1549, 2016, doi: https://doi.org/10.1002/adem.201600172.

[38]   G. Ziółkowski, E. Chlebus, P. Szymczyk, and J. Kurzac, "Application of X-ray CT method for discontinuity and porosity detection in 316L stainless steel parts produced with SLM technology," *Arch. Civ. Mech. Eng.*, vol. 14, no. 4, pp. 608–614, 2014, doi: 10.1016/j.acme.2014.02.003.

[39]   E. C. Santos, K. Osakada, M. Shiomi, Y. Kitamura, and F. Abe, "Microstructure and mechanical properties of pure titanium models fabricated by selective laser melting," *Proc. Inst. Mech. Eng. Part C J. Mech. Eng. Sci.*, vol. 218, no. 7, pp. 711–719, 2004, doi: 10.1243/0954406041319545.

[40]   A. du Plessis and E. Macdonald, "Hot isostatic pressing in metal additive manufacturing: X-ray tomography reveals details of pore closure," *Addit. Manuf.*, vol. 34, p. 101191, 2020, doi: https://doi.org/10.1016/j.addma.2020.101191.

[41]   C. B. Finfrock, A. Exil, J. D. Carroll, and L. Deibler, "Effect of Hot Isostatic Pressing and Powder Feedstock on Porosity , Microstructure , and Mechanical Properties of Selective Laser Melted," *Metallogr. Microstruct. Anal.*, vol. 7, no. 4, pp. 443–456, 2018, doi: 10.1007/s13632-018-0456-z.

[42]   Z. Wang *et al.*, "Uncertainty quantification and reduction in metal additive manufacturing," *npj Comput. Mater.*, vol. 6, no. 1, 2020, doi: 10.1038/s41524-020-00444-x.

[43]   A. A. Martin *et al.*, "Dynamics of pore formation during laser powder bed fusion additive manufacturing," *Nat. Commun.*, vol. 10, no. 1, pp. 1–10, 2019, doi: 10.1038/s41467-019-10009-2.

[44]   W. E. King *et al.*, "Observation of keyhole-mode laser melting in laser powder-bed fusion additive manufacturing," *J. Mater. Process. Technol.*, vol. 214, no. 12, pp. 2915–2925, 2014, doi: https://doi.org/10.1016/j.jmatprotec.2014.06.005.

[45]   M. Bayat *et al.*, "Keyhole-induced porosities in Laser-based Powder Bed Fusion (L-PBF) of Ti6Al4V: High-fidelity modelling and experimental validation," *Addit. Manuf.*, vol. 30, no. August, p. 100835, 2019, doi: 10.1016/j.addma.2019.100835.

[46]   A. Yadollahi and N. Shamsaei, "Additive manufacturing of fatigue resistant materials: Challenges and opportunities," *Int. J. Fatigue*, vol. 98, pp. 14–31, 2017, doi: 10.1016/j.ijfatigue.2017.01.001.

[47]   H. Masuo *et al.*, "Effects of Defects, Surface Roughness and HIP on Fatigue Strength of Ti-6Al-4V manufactured by Additive Manufacturing," *Procedia Struct. Integr.*, vol. 7, pp. 19–26, 2017, doi: https://doi.org/10.1016/j.prostr.2017.11.055.

[48]   Y. Murakami, H. Masuo, Y. Tanaka, and M. Nakatani, "Defect Analysis for Additively Manufactured Materials in Fatigue from the Viewpoint of Quality Control and Statistics of Extremes," *Procedia Struct. Integr.*, vol. 19, pp. 113–122, 2019, doi: https://doi.org/10.1016/j.prostr.2019.12.014.

[49]   U. Zerbst, M. Madia, C. Klinger, D. Bettge, and Y. Murakami, "Defects as a root cause of fatigue failure of metallic components. I: Basic aspects," *Eng. Fail. Anal.*, vol. 97, pp. 777–792, 2019, doi: https://doi.org/10.1016/j.engfailanal.2019.01.055.

[50]   D. Deng, H. Murakawa, and W. Liang, "Numerical and experimental investigations on welding residual stress in multi-pass butt-welded austenitic stainless steel pipe," *Comput. Mater. Sci.*, vol. 42, no. 2, pp. 234–244, 2008, doi: https://doi.org/10.1016/j.commatsci.2007.07.009.

[51]   A. De and T. DebRoy, "A perspective on residual stresses in welding," *Sci. Technol. Weld. Join.*, vol. 16, no. 3, pp. 204–208, 2011, doi: 10.1179/136217111X12978476537783.

[52]   K. Masubuchi, *Analysis of welded structures: residual stresses, distortion, and their consequences*, Vol. 33. Elsevier, 2013.

[53]   T. DebRoy *et al.*, "Additive manufacturing of metallic components – Process, structure and properties," *Prog. Mater. Sci.*, vol. 92, pp. 112–224, 2018, doi: https://doi.org/10.1016/j.pmatsci.2017.10.001.

[54]   G. A. Webster and A. N. Ezeilo, "Residual stress distributions and their influence on fatigue lifetimes," *Int. J. Fatigue*, vol. 23, pp. 375–383, 2001, doi: https://doi.org/10.1016/S0142-1123(01)00133-5.

[55]   M. Shiomi, K. Osakada, K. Nakamura, T. Yamashita, and F. Abe, "Residual stress within metallic model made by selective laser melting process," *CIRP Ann. - Manuf. Technol.*, vol. 53, no. 1, pp. 195–198, 2004, doi: 10.1016/S0007-8506(07)60677-5.

[56]   P. Mercelis and J. P. Kruth, "Residual stresses in selective laser sintering and selective laser melting," *Rapid Prototyp. J.*, vol. 12, no. 5, pp. 254–265, 2006, doi: 10.1108/13552540610707013.

[57]   M. Masoomi, S. M. Thompson, and N. Shamsaei, "Quality part production via multi-laser additive manufacturing," *Manuf. Lett.*, vol. 13, pp. 15–20, 2017, doi: 10.1016/j.mfglet.2017.05.003.

[58]   X. Wang and K. Chou, "The effects of stress relieving heat treatment on the microstructure and residual stress of Inconel 718 fabricated by laser metal powder bed fusion additive manufacturing process," *J. Manuf. Process.*, vol. 48, no. December 2018, pp. 154–163, 2019, doi: 10.1016/j.jmapro.2019.10.027.

[59] P. Dong, "Residual stresses and distortions in welded structures: a perspective for engineering applications," *Sci. Technol. Weld. Join.*, vol. 10, no. 4, pp. 389–398, 2005, doi: 10.1179/174329305X29465.

[60] X. Wang and K. Chou, "Residual stress in metal parts produced by powder-bed additive manufacturing processes," *Proc. - 26th Annu. Int. Solid Free. Fabr. Symp. - An Addit. Manuf. Conf. SFF 2015*, pp. 1463–1474, 2020.

[61] F. Liu, X. Lin, G. Yang, M. Song, J. Chen, and W. Huang, "Microstructure and residual stress of laser rapid formed Inconel 718 nickel-base superalloy," *Opt. Laser Technol.*, vol. 43, no. 1, pp. 208–213, 2011, doi: https://doi.org/10.1016/j.optlastec.2010.06.015.

[62] R. Barros *et al.*, "Stress Analysis Before and After Heat Treatment," *Metals (Basel).*, vol. 9, no. 12, p. 1290, 2019, [Online]. Available: https://www.mdpi.com/2075-4701/9/12/1290

[63] Y. Liu, Y. Yang, and D. Wang, "A study on the residual stress during selective laser melting (SLM) of metallic powder," *Int. J. Adv. Manuf. Technol.*, vol. 87, no. 1–4, pp. 647–656, 2016, doi: 10.1007/s00170-016-8466-y.

[64] L. Parry, I. A. Ashcroft, and R. D. Wildman, "Understanding the effect of laser scan strategy on residual stress in selective laser melting through thermo-mechanical simulation," *Addit. Manuf.*, vol. 12, pp. 1–15, 2016, doi: https://doi.org/10.1016/j.addma.2016.05.014.

[65] Y. Lu *et al.*, "Study on the microstructure, mechanical property and residual stress of SLM Inconel-718 alloy manufactured by differing island scanning strategy," *Opt. Laser Technol.*, vol. 75, pp. 197–206, 2015, doi: https://doi.org/10.1016/j.optlastec.2015.07.009.

[66] J. Robinson, I. Ashton, P. Fox, E. Jones, and C. Sutcliffe, "Determination of the effect of scan strategy on residual stress in laser powder bed fusion additive manufacturing," *Addit. Manuf.*, vol. 23, no. June, pp. 13–24, 2018, doi: 10.1016/j.addma.2018.07.001.

[67] T. Simson, A. Emmel, A. Dwars, and J. Böhm, "Residual stress measurements on AISI 316L samples manufactured by selective laser melting," *Addit. Manuf.*, vol. 17, pp. 183–189, 2017, doi: https://doi.org/10.1016/j.addma.2017.07.007.

[68] P. Pant *et al.*, "Mapping of residual stresses in as-built Inconel 718 fabricated by laser powder bed fusion: A neutron diffraction study of build orientation influence on residual stresses," *Addit. Manuf.*, vol. 36, no. February, p. 101501, 2020, doi: 10.1016/j.addma.2020.101501.

[69] L. Parry, I. A. Ashcroft, and R. D. Wildman, "Understanding the effect of laser scan strategy on residual stress in selective laser melting through thermo-mechanical simulation," *Addit. Manuf.*, vol. 12, pp. 1–15, 2016, doi: 10.1016/j.addma.2016.05.014.

[70] D. Deng, R. L. Peng, H. Brodin, and J. Moverare, "Microstructure and mechanical properties of Inconel 718 produced by selective laser melting: Sample orientation dependence and effects of post heat treatments," *Mater. Sci. Eng. A*, vol. 713, no. July 2017, pp. 294–306, 2018, doi: 10.1016/j.msea.2017.12.043.

[71] D. Buchbinder, W. Meiners, N. Pirch, K. Wissenbach, and J. Schrage, "Investigation on reducing distortion by preheating during manufacture of aluminum components using selective laser melting," *J. Laser Appl.*, vol. 26, no. 1, p. 12004, 2013, doi: 10.2351/1.4828755.

[72] J. Zhang, S. Li, Q. Wei, Y. Shi, L. Wang, and L. Guo, "Cracking behavior and inhibiting process of inconel 625 alloy formed by selective laser melting," vol. 39, pp. 961–966, 2015, doi: 10.13373/j.cnki.cjrm.2015.11.001.

[73] C. Silbernagel, L. Gargalis, I. Ashcroft, R. Hague, M. Galea, and P. Dickens, "Electrical resistivity of pure copper processed by medium-powered laser powder bed fusion additive

manufacturing for use in electromagnetic applications," *Addit. Manuf.*, vol. 29, p. 100831, 2019, doi: https://doi.org/10.1016/j.addma.2019.100831.

[74] J. Guo, H. Fu, B. Pan, and R. Kang, "Recent progress of residual stress measurement methods: A review," *Chinese J. Aeronaut.*, vol. 34, no. 2, pp. 54–78, 2020, doi: 10.1016/j.cja.2019.10.010.

[75] M. Masoomi *et al.*, "Residual stress measurements via neutron diffraction of additive manufactured stainless steel 17-4 PH," *Data Br.*, vol. 13, pp. 408–414, 2017, doi: 10.1016/j.dib.2017.06.027.

[76] N. S. Rossini, M. Dassisti, K. Y. Benyounis, and A. G. Olabi, "Methods of measuring residual stresses in components," *Mater. Des.*, vol. 35, pp. 572–588, 2012, doi: https://doi.org/10.1016/j.matdes.2011.08.022.

[77] K. Tanaka, "The cosα method for X-ray residual stress measurement using two-dimensional detector," *Mech. Eng. Rev.*, vol. 6, no. 1, pp. 18-00378-18–00378, 2019, doi: 10.1299/mer.18-00378.

[78] S. X. Elastic, "Comparison of Two X-Ray Residual Stress Measurement Methods: Sin2 ψ and Cos α, Through the Determination of a Martensitic Steel X-Ray Elastic Constant," *Residual Stress. 2016*, vol. 2, no. January 2017, pp. 55–60, 2017, doi: 10.21741/9781945291173-10.

[79] T. Oguri, T. Tanaka, T. Okano, K. Murata, H. Kawakami, and Y. Sato, "X-ray Stress Measurement of the Cylindrical Surface by the cos α Method," *J. Soc. Mater. Sci. Japan*, vol. 66, pp. 488–494, 2017, doi: 10.2472/jsms.66.488.

[80] D. Delbergue *et al.*, "Comparison of Two X-Ray Residual Stress Measurement Methods : Sin2 ψ and Cos α , Through the Determination of a Martensitic Steel X-Ray Elastic Constant

To cite this version : HAL Id : hal-01823988 Comparison of Two X-Ray Residual Stress Measurement Metho," *Mater. Res.*, vol. 2, pp. 55–60, 2016.

[81]   H. L. Wei, J. W. Elmer, and T. DebRoy, "Origin of grain orientation during solidification of an aluminum alloy," *Acta Mater.*, vol. 115, pp. 123–131, 2016, doi: https://doi.org/10.1016/j.actamat.2016.05.057.

[82]   T. Wang, Y. Y. Zhu, S. Q. Zhang, H. B. Tang, and H. M. Wang, "Grain morphology evolution behavior of titanium alloy components during laser melting deposition additive manufacturing," *J. Alloys Compd.*, vol. 632, pp. 505–513, 2015, doi: https://doi.org/10.1016/j.jallcom.2015.01.256.

[83]   A. Yadollahi, N. Shamsaei, S. M. Thompson, and D. W. Seely, "Effects of process time interval and heat treatment on the mechanical and microstructural properties of direct laser deposited 316L stainless steel," *Mater. Sci. Eng. A*, vol. 644, pp. 171–183, 2015, doi: 10.1016/j.msea.2015.07.056.

[84]   L. L. Parimi, R. G. A., D. Clark, and M. M. Attallah, "Microstructural and texture development in direct laser fabricated IN718," *Mater. Charact.*, vol. 89, pp. 102–111, 2014, doi: https://doi.org/10.1016/j.matchar.2013.12.012.

[85]   N. Raghavan *et al.*, "Numerical modeling of heat-transfer and the influence of process parameters on tailoring the grain morphology of IN718 in electron beam additive manufacturing," *Acta Mater.*, vol. 112, pp. 303–314, 2016, doi: https://doi.org/10.1016/j.actamat.2016.03.063.

[86]   A. K. Parida and K. Maity, "Comparison the machinability of Inconel 718, Inconel 625 and Monel 400 in hot turning operation," *Eng. Sci. Technol. an Int. J.*, vol. 21, no. 3, pp. 364–370, 2018, doi: https://doi.org/10.1016/j.jestch.2018.03.018.

[87]   K. Mahesh, J. T. Philip, S. N. Joshi, and B. Kuriachen, "Machinability of Inconel 718: A critical review on the impact of cutting temperatures," *Mater. Manuf. Process.*, vol. 36, no. 7, pp. 753–791, 2021, doi: 10.1080/10426914.2020.1843671.

[88]   D. M. D'Addona, S. J. Raykar, and M. M. Narke, "High Speed Machining of Inconel 718: Tool Wear and Surface Roughness Analysis," *Procedia CIRP*, vol. 62, pp. 269–274, 2017, doi: 10.1016/j.procir.2017.03.004.

[89]   G. Marchese *et al.*, "Influence of heat treatments on microstructure evolution and mechanical properties of Inconel 625 processed by laser powder bed fusion," *Mater. Sci. Eng. A*, vol. 729, pp. 64–75, 2018, doi: 10.1016/j.msea.2018.05.044.

[90]   F. Zhang *et al.*, "Homogenization kinetics of a nickel-based superalloy produced by powder bed fusion laser sintering," *Scr. Mater.*, vol. 131, pp. 98–102, 2017, doi: 10.1016/j.scriptamat.2016.12.037.

[91]   F. Zhang *et al.*, "Effect of heat treatment on the microstructural evolution of a nickel-based superalloy additive-manufactured by laser powder bed fusion," *Acta Mater.*, vol. 152, pp. 200–214, 2018, doi: 10.1016/j.actamat.2018.03.017.

[92]   C. Li, R. White, X. Y. Fang, M. Weaver, and Y. B. Guo, "Microstructure evolution characteristics of Inconel 625 alloy from selective laser melting to heat treatment," *Mater. Sci. Eng. A*, vol. 705, no. August, pp. 20–31, 2017, doi: 10.1016/j.msea.2017.08.058.

[93]   L. M. Suave *et al.*, "Microstructural evolutions during thermal aging of alloy 625: Impact of temperature and forming process," *Metall. Mater. Trans. A Phys. Metall. Mater. Sci.*, vol. 45, no. 7, pp. 2963–2982, 2014, doi: 10.1007/s11661-014-2256-7.

[94]   M. Sundararaman, L. Kumar, G. Eswara Prasad, P. Mukhopadhyay, and S. Banerjee, "Precipitation of an intermetallic phase with Pt2Mo-type structure in alloy 625," *Metall.*

Mater. Trans. A Phys. Metall. Mater. Sci., vol. 30, no. 1, pp. 41–52, 1999, doi: 10.1007/s11661-999-0194-6.

[95]   P. Petrzak, K. Kowalski, and M. Blicharski, "Analysis of phase transformations in Inconel 625 alloy during annealing," *Acta Phys. Pol. A*, vol. 130, no. 4, pp. 1041–1044, 2016, doi: 10.12693/APhysPolA.130.1041.

[96]   D. Deng, *Additively Manufactured Inconel 718 : Microstructures and Mechanical Properties*, no. 1798. 2018.

[97]   S. Mahadevan, S. Nalawade, J. B. Singh, A. Verma, B. Paul, and K. Ramaswamy, "Evolution of δ phase microstructure in alloy 718," *7th Int. Symp. Superalloy 718 Deriv. 2010*, vol. 2, pp. 737–750, 2010, doi: 10.1002/9781118495223.ch57.

[98]   E. Chlebus, K. Gruber, B. Kuźnicka, J. Kurzac, and T. Kurzynowski, "Effect of heat treatment on the microstructure and mechanical properties of Inconel 718 processed by selective laser melting," *Mater. Sci. Eng. A*, vol. 639, pp. 647–655, 2015, doi: https://doi.org/10.1016/j.msea.2015.05.035.

[99]   Y.-L. Kuo, S. Horikawa, and K. Kakehi, "The effect of interdendritic δ phase on the mechanical properties of Alloy 718 built up by additive manufacturing," *Mater. Des.*, vol. 116, pp. 411–418, 2017, doi: https://doi.org/10.1016/j.matdes.2016.12.026.

[100]   G. H. Cao *et al.*, "Investigations of γ′, γ″ and δ precipitates in heat-treated Inconel 718 alloy fabricated by selective laser melting," *Mater. Charact.*, vol. 136, pp. 398–406, 2018, doi: https://doi.org/10.1016/j.matchar.2018.01.006.

[101]   Y. Desvallees, M. Bouzidi, F. Bois, and N. Beaude, "Delta Phase in INCONEL 718: Mechanical Properties and Forging Process Requirements," pp. 281–291, 2012, doi: 10.7449/1994/superalloys_1994_281_291.

[102] J. F. Radavich, "The Physical Metallurgy of Cast and Wrought Alloy 718," pp. 229–240, 2012, doi: 10.7449/1989/superalloys_1989_229_240.

[103] W. J. S. H. B. A. S. T. L. E. L. R. R. Dehoff M. M. Kirka and S. S. Babu, "Site specific control of crystallographic grain orientation through electron beam additive manufacturing," *Mater. Sci. Technol.*, vol. 31, no. 8, pp. 931–938, 2015, doi: 10.1179/1743284714Y.0000000734.

[104] H. Qin, V. Fallah, Q. Dong, M. Brochu, M. R. Daymond, and M. Gallerneault, "Solidification pattern, microstructure and texture development in Laser Powder Bed Fusion (LPBF) of Al10SiMg alloy," *Mater. Charact.*, vol. 145, pp. 29–38, 2018, doi: https://doi.org/10.1016/j.matchar.2018.08.025.

[105] O. Gokcekaya, T. Ishimoto, S. Hibino, J. Yasutomi, T. Narushima, and T. Nakano, "Unique crystallographic texture formation in Inconel 718 by laser powder bed fusion and its effect on mechanical anisotropy," *Acta Mater.*, vol. 212, p. 116876, 2021, doi: https://doi.org/10.1016/j.actamat.2021.116876.

[106] F. Schmeiser, E. Krohmer, C. Wagner, N. Schell, E. Uhlmann, and W. Reimers, "In situ microstructure analysis of Inconel 625 during laser powder bed fusion," *J. Mater. Sci.*, vol. 57, no. 21, pp. 9663–9677, 2022, doi: 10.1007/s10853-021-06577-8.

[107] G. Marchese *et al.*, "The role of texturing and microstructure evolution on the tensile behavior of heat-treated Inconel 625 produced via laser powder bed fusion," *Mater. Sci. Eng. A*, vol. 769, p. 138500, 2020, doi: https://doi.org/10.1016/j.msea.2019.138500.

[108] G. Marchese *et al.*, "Characterization and Comparison of Inconel 625 Processed by Selective Laser Melting and Laser Metal Deposition," *Adv. Eng. Mater.*, vol. 19, no. 3, p. 1600635, 2017, doi: https://doi.org/10.1002/adem.201600635.

[109] P. Wang *et al.*, "Microstructural characteristics and mechanical properties of carbon nanotube reinforced Inconel 625 parts fabricated by selective laser melting," *Mater. Des.*, vol. 112, pp. 290–299, 2016, doi: https://doi.org/10.1016/j.matdes.2016.09.080.

[110] A. Kreitcberg, V. Brailovski, and S. Turenne, "Effect of heat treatment and hot isostatic pressing on the microstructure and mechanical properties of Inconel 625 alloy processed by laser powder bed fusion," *Mater. Sci. Eng. A*, vol. 689, no. December 2016, pp. 1–10, 2017, doi: 10.1016/j.msea.2017.02.038.

[111] S. Li, Q. Wei, Y. Shi, C. K. Chua, Z. Zhu, and D. Zhang, "Microstructure Characteristics of Inconel 625 Superalloy Manufactured by Selective Laser Melting," *J. Mater. Sci. Technol.*, vol. 31, no. 9, pp. 946–952, 2015, doi: 10.1016/j.jmst.2014.09.020.

[112] K. Inaekyan, A. Kreitcberg, S. Turenne, and V. Brailovski, "Microstructure and mechanical properties of laser powder bed-fused IN625 alloy," *Mater. Sci. Eng. A*, vol. 768, no. September, p. 138481, 2019, doi: 10.1016/j.msea.2019.138481.

[113] X. Y. Fang, H. Q. Li, M. Wang, C. Li, and Y. B. Guo, "Characterization of texture and grain boundary character distributions of selective laser melted Inconel 625 alloy," *Mater. Charact.*, vol. 143, pp. 182–190, 2018, doi: https://doi.org/10.1016/j.matchar.2018.02.008.

[114] E. M. Fayed, M. Saadati, D. Shahriari, V. Brailovski, M. Jahazi, and M. Medraj, "Optimization of the Post-Process Heat Treatment of Inconel 718 Superalloy Fabricated by Laser Powder Bed Fusion Process," *Metals (Basel).*, vol. 11, no. 1, 2021, doi: 10.3390/met11010144.

[115] E. Broitman, "Indentation Hardness Measurements at Macro-, Micro-, and Nanoscale: A Critical Overview," *Tribol. Lett.*, vol. 65, no. 1, pp. 1–18, 2017, doi: 10.1007/s11249-016-0805-5.

[116] N. K. Mukhopadhyay and P. Paufler, "Micro- and Nanoindentation Techniques for Mechanical Characterisation of Materials," *Int. Mater. Rev.*, vol. 51, pp. 209–245, 2006, doi: 10.1179/174328006X102475.

[117] ASTM Standard, "Standard Test Methods for Vickers Hardness and Knoop Hardness of Metallic Materials," vol. 03.01, pp. 1–28, 17AD, doi: 10.1520/E0092-23.

[118] J. Van Bavel, "The world population explosion: causes, backgrounds and -projections for the future.," *Facts, views Vis. ObGyn*, vol. 5, no. 4, pp. 281–91, 2013, [Online]. Available: http://www.ncbi.nlm.nih.gov/pubmed/24753956%0Ahttp://www.pubmedcentral.nih.gov/articlerender.fcgi?artid=PMC3987379

[119] P. A. Owusu and S. Asumadu-Sarkodie, "A review of renewable energy sources, sustainability issues and climate change mitigation," *Cogent Eng.*, vol. 3, no. 1, p. 1167990, Dec. 2016, doi: 10.1080/23311916.2016.1167990.

[120] K. L. Murty and I. Charit, "Structural materials for Gen-IV nuclear reactors: Challenges and opportunities," *J. Nucl. Mater.*, vol. 383, no. 1, pp. 189–195, 2008, doi: https://doi.org/10.1016/j.jnucmat.2008.08.044.

[121] J. Kupitz, F. Depisch, and O. Azpitarte, "The IAEA International Project on Innovative Nuclear Reactors and Fuel Cycles (INPRO): Status, ongoing activities and outlook," *Proc. 2004 Int. Congr. Adv. Nucl. Power Plants, ICAPP'04*, pp. 675–684, 2004.

[122] B. Zohuri, *Generation IV nuclear reactors*. 2020. doi: 10.1016/B978-0-12-818483-7.00006-8.

[123] E. M. A. Hussein, "Emerging small modular nuclear power reactors: A critical review," *Phys. Open*, vol. 5, p. 100038, 2020, doi: https://doi.org/10.1016/j.physo.2020.100038.

[124] S. G. Kim *et al.*, "A concept design of supercritical CO2 cooled SMR operating at isolated

microgrid region," *Int. J. Energy Res.*, vol. 41, no. 4, pp. 512–525, 2017, doi: https://doi.org/10.1002/er.3633.

[125] E. M. A. Hussein, "Emerging small modular nuclear power reactors: A critical review," *Phys. Open*, vol. 5, no. August, p. 100038, 2020, doi: 10.1016/j.physo.2020.100038.

[126] L. Boldon, L; Sabharwall, P; Painter, C; Liu, "AN OVERVIEW OF SMALL MODULAR REACTORS : STATUS OF GLOBAL DEVELOPMENT , POTENTIAL DESIGN ADVANTAGES , AND METHODS FOR ECONOMIC ASSISSMENT," *Int. J. Energy, Environ. Econ.*, vol. 22, no. 5, pp. 437–459.

[127] IAEA, "Advances in Small Modular Reactor Technology Developments," *A Suppl. to IAEA Adv. React. Inf. Syst. 2020 Ed.*, p. 354, 2020, [Online]. Available: http://aris.iaea.org/

[128] International Atomic Energy Agency (IAEA), "What are Small Modular Reactors (SMRs)?" https://www.iaea.org/newscenter/news/what-are-small-modular-reactors-smrs

[129] B. Betzler, *Additive Manufacturing in the Nuclear Reactor Industry*. 2021. doi: 10.1016/B978-0-12-819725-7.00106-9.

[130] J. O. Stiegler and L. K. Mansur, "Radiation Effects in Structural Materials," *Annu. Rev. Mater. Sci.*, vol. 9, no. 1, pp. 405–454, 1979, doi: 10.1146/annurev.ms.09.080179.002201.

[131] G. Sharma *et al.*, "Effect of irradiation on the microstructure and mechanical behavior of nanocrystalline nickel," *Scr. Mater.*, vol. 65, no. 8, pp. 727–730, 2011, doi: https://doi.org/10.1016/j.scriptamat.2011.07.021.

[132] W. B. Liu, Y. Z. Ji, P. K. Tan, C. Zhang, C. H. He, and Z. G. Yang, "Microstructure evolution during helium irradiation and post-irradiation annealing in a nanostructured reduced activation steel," *J. Nucl. Mater.*, vol. 479, pp. 323–330, 2016, doi: https://doi.org/10.1016/j.jnucmat.2016.07.030.

[133] C.-L. Chen, A. Richter, and R. Kögler, "The effect of dual Fe+/He+ ion beam irradiation on microstructural changes in FeCrAl ODS alloys," *J. Alloys Compd.*, vol. 586, pp. S173–S179, 2014, doi: https://doi.org/10.1016/j.jallcom.2012.11.113.

[134] R. W. Harrison, "On the use of ion beams to emulate the neutron irradiation behaviour of tungsten," *Vacuum*, vol. 160, no. March 2018, pp. 355–370, 2019, doi: 10.1016/j.vacuum.2018.11.050.

[135] Q. Dong, Z. Yao, P. Saidi, and M. R. Daymond, "Effect of pre-existing dislocations on the formation of dislocation loops: Pure magnesium under electron irradiation," *J. Nucl. Mater.*, vol. 511, pp. 43–55, 2018, doi: https://doi.org/10.1016/j.jnucmat.2018.08.040.

[136] X.-M. Bai and B. P. Uberuaga, "The Influence of Grain Boundaries on Radiation-Induced Point Defect Production in Materials: A Review of Atomistic Studies," *JOM*, vol. 65, no. 3, pp. 360–373, 2013, doi: 10.1007/s11837-012-0544-5.

[137] G. Monnet, "Multiscale modeling of irradiation hardening: Application to important nuclear materials," *J. Nucl. Mater.*, vol. 508, pp. 609–627, 2018, doi: https://doi.org/10.1016/j.jnucmat.2018.06.020.

[138] M. L. Grossbeck, "Effect of Radiation on Strength and Ductility of Metals and Alloys," *Compr. Nucl. Mater. Second Ed.*, pp. 130–152, 2020, doi: 10.1016/B978-0-08-102865-0.00004-2.

[139] S. J. Zinkle and J. T. Busby, "Structural materials for fission & fusion energy," *Mater. Today*, vol. 12, no. 11, pp. 12–19, 2009, doi: https://doi.org/10.1016/S1369-7021(09)70294-9.

[140] Z. Cheng *et al.*, "Irradiation effects in high-entropy alloys and their applications," *J. Alloys Compd.*, vol. 930, p. 166768, 2023, doi: https://doi.org/10.1016/j.jallcom.2022.166768.

[141] M. R. Stoudt *et al.*, "The Influence of Annealing Temperature and Time on the Formation of δ-Phase in Additively-Manufactured Inconel 625," *Metall. Mater. Trans. A Phys. Metall. Mater. Sci.*, vol. 49, no. 7, pp. 3028–3037, 2018, doi: 10.1007/s11661-018-4643-y.

[142] T. Sasaki, Y. Hirose, K. Sasaki, and S. Yasukawa, "Influence of image processing conditions of Debye Scherrer ring images in X-ray stress measurement using an imaging plate ," *JCPDS-International Cent. Diffr. Data*, no. C, 1997.

[143] K. Siang, "Effect of Residual Stress and Cold Work on Fatigue of Inconel 718 - Final.pdf," 2019.

[144] L. Shuai, Q. Wei, Y. Shi, J. Zhang, and L. Wei, "Micro-crack formation and controlling of Inconel625 parts fabricated by selective laser melting," *Solid Free. Fabr. 2016 Proc. 27th Annu. Int. Solid Free. Fabr. Symp. - An Addit. Manuf. Conf. SFF 2016*, pp. 520–529, 2016.

[145] L. H. Wu and C. H. Jiang, "Effect of shot peening on residual stress and microstructure in the deformed layer of Inconel 625," *Mater. Trans.*, vol. 58, no. 2, pp. 164–166, 2017, doi: 10.2320/matertrans.M2016298.

[146] T. Ungár, "Microstructural parameters from X-ray diffraction peak broadening," *Scr. Mater.*, vol. 51, no. 8 SPEC. ISS., pp. 777–781, 2004, doi: 10.1016/j.scriptamat.2004.05.007.

[147] T. De Terris, O. Castelnau, Z. Hadjem-hamouche, H. Haddadi, V. Michel, and P. Peyre, "Analysis of As-Built Microstructures and Recrystallization Phenomena on Inconel 625 Alloy Obtained via Laser Powder Bed Fusion (L-PBF)," *Metals (Basel).*, vol. 11, no. 4, p. 619, 2021, [Online]. Available: https://doi.org/10.3390/met11040619

[148] A. S. Gill, A. Telang, C. Ye, S. R. Mannava, D. Qian, and V. K. Vasudevan, "Localized plastic deformation and hardening in laser shock peened Inconel alloy 718SPF," *Mater.*

Charact., vol. 142, no. May, pp. 15–26, 2018, doi: 10.1016/j.matchar.2018.05.010.

[149] D. Tabor, "A Simple Theory of Static and Dynamic Hardness," *Proc. R. Soc. London Ser. A*, vol. 192, no. 1029, pp. 247–274, Feb. 1948, doi: 10.1098/rspa.1948.0008.

[150] R. Hill, E. H. Lee, S. J. Tupper, and N. F. Mott, "The theory of wedge indentation of ductile materials," *Proc. R. Soc. London. Ser. A. Math. Phys. Sci.*, vol. 188, no. 1013, pp. 273–289, 1947, doi: 10.1098/rspa.1947.0009.

[151] S. Tammas-Williams, P. J. Withers, I. Todd, and P. B. Prangnell, "Porosity regrowth during heat treatment of hot isostatically pressed additively manufactured titanium components," *Scr. Mater.*, vol. 122, pp. 72–76, 2016, doi: https://doi.org/10.1016/j.scriptamat.2016.05.002.

[152] S. J. Hirsch, L. Winter, T. Grund, and T. Lampke, "Heat Treatment Influencing Porosity and Tensile Properties of Field Assisted Sintered AlSi7Mg0.6," *Materials (Basel).*, vol. 15, no. 7, 2022, doi: 10.3390/ma15072503.

[153] H. Bu, L. Chen, and Y. Duan, "Effect of Solution Heat Treatment on the Porosity Growth of Nickel-Based P/M Superalloys," *Metals (Basel).*, vol. 12, no. 11, 2022, doi: 10.3390/met12111973.

[154] A. Kumar Maurya and A. Kumar, "Effect of building orientation & heat-treatment on microhardness & surface roughness of additive manufactured IN718 alloy," *Mater. Today Proc.*, vol. 59, pp. 628–635, 2022, doi: https://doi.org/10.1016/j.matpr.2021.12.180.

[155] Z. Wang, K. Guan, M. Gao, X. Li, X. Chen, and X. Zeng, "The microstructure and mechanical properties of deposited-IN718 by selective laser melting," *J. Alloys Compd.*, vol. 513, pp. 518–523, 2012, doi: 10.1016/j.jallcom.2011.10.107.

[156] X. Xiao, "Fundamental mechanisms for irradiation-hardening and embrittlement: A

review," *Metals (Basel).*, vol. 9, no. 10, 2019, doi: 10.3390/met9101132.

[157] B. P. Eftink *et al.*, "Proton irradiation and characterization of additively manufactured 304L stainless steels," *J. Nucl. Mater.*, vol. 531, p. 152007, 2020, doi: 10.1016/j.jnucmat.2020.152007.

[158] T. S. Byun *et al.*, "Mechanical behavior of additively manufactured and wrought 316L stainless steels before and after neutron irradiation," *J. Nucl. Mater.*, vol. 548, p. 152849, 2021, doi: 10.1016/j.jnucmat.2021.152849.

[159] M. A. Stopher, "The effects of neutron radiation on nickel-based alloys," *Mater. Sci. Technol. (United Kingdom)*, vol. 33, no. 5, pp. 518–536, 2017, doi: 10.1080/02670836.2016.1187334.

[160] T. M. Angeliu, J. T. Ward, and J. K. Witter, "Assessing the effects of radiation damage on Ni-base alloys for the prometheus space reactor system," *J. Nucl. Mater.*, vol. 366, no. 1–2, pp. 223–237, 2007, doi: 10.1016/j.jnucmat.2007.01.217.

[161] A. Aitkaliyeva, L. He, H. Wen, B. Miller, X. M. Bai, and T. Allen, *Irradiation effects in Generation IV nuclear reactor materials*, no. January. 2017. doi: 10.1016/B978-0-08-100906-2.00007-0.

[162] S. Pratheesh Kumar, S. Elangovan, R. Mohanraj, and J. R. Ramakrishna, "A review on properties of Inconel 625 and Inconel 718 fabricated using direct energy deposition," *Mater. Today Proc.*, vol. 46, pp. 7892–7906, 2021, doi: 10.1016/j.matpr.2021.02.566.

[163] T. S. Byun and K. Farrell, "Tensile properties of Inconel 718 after low temperature neutron irradiation," *J. Nucl. Mater.*, vol. 318, no. SUPPL, pp. 292–299, 2003, doi: 10.1016/S0022-3115(03)00006-0.

[164] Z. H. Ismail, "Effect of low dose neutron irradiation on the mechanical properties of an

AIMgSi alloy," *Radiat. Eff. Defects Solids*, vol. 112, no. 4, pp. 105–110, 1990, doi: 10.1080/10420159008213036.

[165] M. Sun, L. Yu, and X. Xiao, "Model for irradiation softening of nickel-based single crystal superalloys under ion irradiation," *J. Mater. Res. Technol.*, vol. 22, pp. 3101–3107, 2023, doi: https://doi.org/10.1016/j.jmrt.2022.12.122.

[166] S. G. Giniyatova *et al.*, "Study of the Mechanisms of Radiation Softening and Swelling upon Irradiation of TiTaNbV Alloys with He2+ Ions with an Energy of 40 keV," *Materials (Basel).*, vol. 16, no. 11, 2023, doi: 10.3390/ma16114031.

[167] M. Tanaka, K. Fukaya, and K. Shiraishi, "Radiation Softening and Hardening in Neutron Irradiated Molybdenum.," *Trans. Japan Inst. Met.*, vol. 20, no. 12, pp. 697–705, 1979, doi: 10.2320/matertrans1960.20.697.

[168] A. Tsepelev, "Radiation-induced softening of Fe-Mo alloy under high- temperature electron irradiation," *IOP Conf. Ser. Mater. Sci. Eng.*, vol. 130, no. 1, 2016, doi: 10.1088/1757-899X/130/1/012016.